Multielectron effects in strong field processes in molecules

by

Yuqing Xia

B.A., University of Science and Technology of China, 2010

M.S., University of Colorado at Boulder, 2013

A thesis submitted to the

Faculty of the Graduate School of the

University of Colorado in partial fulfillment

of the requirements for the degree of

Doctor of Philosophy

Department of Physics

2016

This thesis entitled:
Multielectron effects in strong field processes in molecules
written by Yuqing Xia
has been approved for the Department of Physics

Prof. Agnieszka Jaroń-Becker

Prof. Andreas Becker

Date

The final copy of this thesis has been examined by the signatories, and we find that both the content and the form meet acceptable presentation standards of scholarly work in the above mentioned discipline.

Xia, Yuqing (University of Colorado at Boulder)

Multielectron effects in strong field processes in molecules

Thesis directed by Prof. Agnieszka Jaroń-Becker

Laser technology has experienced a rapid evolution in available intensities, frequencies, and pulse durations over the last three decades. Many new laser induced phenomena in atoms have been discovered, such as multiphoton ionization, above-threshold ionization, high-order harmonic generation etc. For the interaction with atoms, usually only one electron in the outermost shell is assumed to be active (called single-active-electron approximation) while all other electrons are considered to remain frozen in their initial states. Due to the extra degrees of freedom (vibration and rotation) and the more complex structures, the interaction of molecules with intense laser pulses reveals many new features. Recent experiments have indicated that electrons from inner valence orbitals of molecules can have significant contributions to ionization and high harmonic generation. Theoretical analysis of these processes in molecules faces the challenge to extend previous theories developed for the atomic case by including the multielectron character of the molecular target.

In this thesis we systematically investigate multielectron effects in the interaction of molecules with intense laser light. To this end, we apply time-dependent density-functional theory to solve the multielectron Schrödinger equation and analyze highly nonlinear processes such as high harmonic generation, laser-induced ionization and nonadiabatic electron localization. Based on the results of our numerical simulations we predict a new feature in the harmonic spectra of molecules, namely the occurrence of fractional harmonics in the form of Mollow sidebands. Such additional peaks in the spectra appear due to a field-induced resonant coupling of an inner valence orbital with the outermost orbital in a molecule. Furthermore, we show that the theoretical explanation of recent experimental data for the ellipticity of high harmonics in N_2 and CO_2 require the systematic consideration of all inner valence shells as well as the proper alignment distribution in the experiment. We also show that the coupling of molecular orbitals in the field can lead to an enhancement of

(inner-shell) ionization, potentially leading to a population inversion in the ion, as well as nonadiabatic electron dynamics, where the electron can be trapped at one side of the molecule over several field cycles. Finally, we present the development of a new intense-field theory based on the Floquet theorem with complex Gaussian basis sets and show results of first applications for ionization of simple systems.

Dedication

To my love and family

Acknowledgements

Firstly, I would like to express my sincere gratitude to my advisor Prof. Agnieszka Jaroń-Becker for her excellent guidance, caring, patience, and providing me with an excellent atmosphere during my Ph.D study and research. She taught me a lot how to question thoughts and express ideas. Her patience and broad knowledge in Chemistry and Physics helped me to overcome many crisis situation in our project and finish this dissertation. She is also very warmhearted and always be ready to help us no matter what problem we met in both research and daily life.

Next, I would like to thank Prof. Andreas Becker, who is like a co-advisor for me in the group. He is a very nice and easygoing person but with rigorous attitude towards science. I am deeply grateful to him for the discussion and always get new ideas because of his keen intuition in Physics.

I would also like to thank my previous and current group members: Dr. Carlos Hernandez-Garcia, Daniel Weflen, Hongcheng Ni, Jing Su, Andrew Spott, Michelle Miller, Cory Goldsmith, Benjamin Miller, Ran Reiff, Erez Shani, Quynh Nguyen, as well as Felipe Cajiao. We not only share our ideas on projects but also any interesting things in life. They helped create a pleasant working environment and make the research full of fun.

The Janus supercomputer and the clusters at JILA have given me continuous computational support during these years. Without these computation resources, I would not be able to finish my research. So I am grateful to all the people working for the Janus supercomputer and the staff members of JILA computing group.

Finally, and most importantly, I would also like to thank my family and my friends for the support they provided me. In particular, I must acknowledge my wife. Thanks for her encouragement when I was frustrated and thanks to her to let me have a such lovely son. All in all, without their love, encouragement I would not have accomplished this thesis.

Contents

Chapter

Tables

Table

Figures

Figure

Chapter 1

Introduction

Since the invention of the laser in 1960s, it has been used extensively to study the response of quantum systems such as atoms, molecules, and solids to the light field, which has extended our knowledge about the mechanism of electron response to coherent radiation. At low light intensity the light-matter interaction is dominated by the process of one- or two-photon absorption or emission, which can be sufficiently analyzed with the lowest-order perturbation theory [1]. The capability of producing high intense light fields over a wide frequency range in the form of short laser pulses opened a new domain in the study of light-matter interaction. At intensities of 10^{13} W/cm^2, the strength of the interaction between electron and light electric field can compete with that of the interaction between electron and Coulomb field. Therefore, the interaction between quantum systems and light field can no longer be treated as a perturbation to the system [2]. Due to the intense laser field, higher order processes, corresponding to the net absorption and emission of more than one photon, called multiphoton processes [3], start to play a significant role. Novel phenomena such as above-threshold ionization (ATI) [4], high-order harmonic generation (HHG) [5, 6], laser-induced correlated electron emission [7, 8] have been observed as a consequence of nonlinear nonperturbative effects.

For the atomic system, the interaction with laser field has been studied extensively and is considered to be well understood. Several ab-initial theoretical techniques as well as systematic approximation methods have been developed and the results agree well with experimental observations. The strong-field ionization from atoms can be modeled successfully by the strong-field

approximation (SFA, also known as Keldysh-Faisal-Reiss (KFR) theory [9, 10, 11]) or by quasi-static tunneling models [9, 12, 13]. In these models, it is assumed that only one of the bound electrons responds to the external field and all others are frozen in their initial states, which is called single-active-electron (SAE) approximation. Such assumption is justified by the fact of large spacing between electronic energy levels in atoms. Another assumption behind these models is that the active electron follows the oscillation of the electric field adiabatically and thus most of strong-field phenomena are interpreted with quasi-static pictures.

Two important fundamental processes in the interaction between atomic systems and strong field, namely ionization and high harmonic generation are studied very well. For ionization at relatively low intensity of a light field, an electron can only be ionized if the energy of the absorbed photon is larger than the ionization potential. When the intensity of the light field increases, multi-photon ionization becomes probable, in which the electron can absorb more than one photon to accumulate enough energy to reach the continuum. At sufficiently high intensities ($I > 10^{11}$ W/cm^2), it was found that the ejected electron can absorb photons in excess of the minimum number required for ionization, which is called above-threshold ionization (ATI), as discovered by Agostini et al. [4] in 1979. If the laser field is sufficiently strong and the frequency is low enough, ionization can be interpreted by using a quasi-static model. In this case, the bound electron experiences an effective potential barrier formed by adding to the atomic potential the potential of the instantaneous laser electric field. The ionization rate can be approximated by the static-limit tunneling rate as given in [14]. The separation between multiphoton ionization and tunneling ionization can be associated with the Keldysh parameter γ_K [9] given by

$$\gamma_K = \sqrt{\frac{I_p}{2U_p}}, \tag{1.1}$$

where I_p is the ionization potential and U_p is the average energy of a free electron in a laser field. The multiphoton ionization is usually more likely to happen for $\gamma_K > 1$ while tunneling ionization dominates for $\gamma_K < 1$.

Another important process in strong field is high-order harmonic generation (HHG). The

interaction between atoms and sufficiently intense laser field can lead to the emission of radiation at high-multiples, or harmonics, of the angular frequency ω of the laser field. Since the discovery of harmonic generation in 1961 by Franken et al. [15], the study of high-order harmonic generation has attracted considerable interest because it extends the range of laser light sources to shorter wavelengths and thus can provide a source of very bright, short-pulse, high-frequency coherent radiation, an attractive low-cost alternative to large scale facilities like synchrotrons and free-electron lasers. Nowadays, the spectra of HHG can be extended to keV regime [16, 17]. The ultrabroad bandwidth of the spectra makes it possible to produce attosecond pulses, which can in principle be used to detect electron dynamics directly at its natural time scale. This opened a new research area: attosecond science [18, 19, 20]. Much of earlier work in experiment as well as in theory in the nonperturbative regime of interaction in atomic systems with radiation have been summarized in [21, 22, 23, 3, 24].

When moving from atoms to study molecules, because of the extra degrees of freedom (rotation and vibration), the multi-center nuclear frame, and a more complex electronic energy level structure, new phenomena such as Coulomb explosion, bond softening, vibration trapping, optically triggered explosion, above-threshold dissociation, and quantum interference were discovered [25, 26, 27, 28, 29, 30, 31]. Most of the previous theories developed for studying atoms need modification to analyze the interaction of molecules with intense laser light. For example, electron wavepackets emitted from different centers in molecules can interfere destructively leading to a suppression of molecular ionization [30, 31] and a minimum in the spectra of high harmonics [28, 29]. On the other hand, the single-active-electron (SAE) model can break down in the interaction between molecules and intense laser fields because the valence orbitals of molecules usually have ionization energies close to each other and thus nonperturbative processes may involve electrons from more than one orbitals [32, 33, 34, 35, 36, 37]. Recently, the alignment [38] of molecules made it possible to control the intersection angle between molecular axis and the polarization of laser field and thus made it possible to study angle-dependent properties. The studies of ionization and HHG dependence on the alignment angle reveal that such processes strongly depend on the sym-

metry of orbitals. As a result, molecular imaging techniques based on HHG were developed, which has became an important topic, since Itatani et al. [39] have shown that HHG may be exploited to tomographically image the highest occupied molecular orbital (HOMO) for diatomic molecules. Besides this, quasi-static picture can also break down in the interaction between molecules and intense laser field, leading to nonadiabatic effects. Compared to atomic systems, the electronic states in molecules are usually much closer to each other and thus a nonadiabatic behavior is easier to induce and observe in molecules because of the coupling of states. The nonadiabatic behavior is also easier to observe in large molecules because the time for an electron inside a large molecule to traverse is longer which is in favor of nonadiabatic response to external laser field [40, 41, 42].

Because of these complex phenomena in molecules, it is important to study the response of molecules in intense laser field to help us understand the mechanisms behind these phenomena better. In this thesis, we analyze multielectron effects in high-order harmonic generation, ionization and nonadiabatic electron localization. Since the solution of multielectron Schrödinger equation for the interaction between a molecule and a laser field at nonperturbative intensities is numerically not achievable, we use the time-dependent density-functional theory. In particular, we study the nonlinear processes for scenarios where the laser field couples states inside the molecule. The thesis is organized as follows:

In Chapter 2 we introduce the time-dependent density-functional theory (TDDFT). TDDFT transforms the problem of solving multielectron Schrödinger equation to the problem of solving single-particle Kohn-Sham equations, which can significantly reduce the computation time. Related concepts like Hohenberg-Kohn theorem, Kohn-Sham equation, exchange-correlation functional, etc. are discussed in this Chapter.

Chapter 3 is devoted to analyze multielectron effects in high-order harmonic spectra from molecules. The basic three-step model and analytical strong-field-approximation (SFA) method are introduced. Specifically, we first investigate the harmonic spectra from open-shell molecules interacting with a laser field, which resonantly couples two states in the molecule. Two new effects are identified and analyzed. Rabi flopping induced by the laser field leads to fractional

harmonics in the form of Mollow sidebands over the whole spectrum of harmonics and modification of the traditional three-step model for the HHG process. Furthermore, we analyze the ellipticity of harmonics from N_2 and CO_2. Ellipticity patterns obtained from our simulations are in good agreement with experimental results. By examining contributions from each valence orbital we surprisingly find significant contributions of inner valence orbitals, which have not been reported previously.

In view of the strong modification of the high-order harmonic generation process due to the resonant coupling, we analyze its influence on the ionization process in Chapter 4. Specifically, we study the coupling of two occupied valence orbitals for molecules like N_2, CO_2, etc. and observe significant enhanced ionization from inner valence orbitals. Consequently, the approximation that inner valence electrons are treated as frozen cannot be applied in such cases. We further show that our results can explain recent observations of population inversion in molecules in recent filamentation experiments.

The coupling between states in strong field can further lead to nonadiabatic electron dynamics in laser driven molecules. In Chapter 5, we study the mechanism behind the nonadiabatic dynamics resulting from coupled states by analyzing the time-dependent changes in the electron density in the laser field. Two competing processes which together lead to the nonadiabatic effects are analyzed with respect to the different type of coupled orbitals as well as the laser intensity on the nonadiabatic processes.

In Chapter 6, we introduce an intense-field method based on basis sets. To this end, we apply the Floquet theorem to time-dependent Schrödinger equation (TDSE) to transform the time-dependent problem into a time-independent problem. To make the Floquet method capable for applications to large molecular systems, we analyze the time-independent problem using Gaussian basis sets. Complex Gaussian basis sets are used to represent the continuum states. An optimization procedure for the exponents of the basis sets is developed. First results for one- and two-photon cross sections are in excellent agreement with those of other calculations.

Finally, we present a summary of the thesis in Chapter 7.

Chapter 2

Time-dependent density-functional theory

The interaction with high intensity laser field has lead to the discovery of many new phenomena in atoms and molecules, which puts a demand for more advanced theoretical approaches to help us understand the mechanism behind it. A real challenge in theoretical description is that the interaction of electrons with the time-dependent electric field cannot be described within perturbation theory because of the high field strength that is comparable to Coulomb field. On the other hand, direct numerical integration of Schrödinger equation is impossible for a system with more than two electrons with current available high power computers. By now, most numerical simulations have been performed within single-active-electron (SAE) approximation, where electrons are assumed to be independent and only one electron is considered to be 'active' while all the remaining electrons are frozen in their initial states. On the other hand, considerable progress towards numerical solution of the six-dimensional Schrödinger problem for double ionization has been achieved with state-of-the-art computations [43, 44, 45] in which two electrons can be 'active'.

Another theoretical approach for strong field problems is Intense-field Many-body S-matrix Theory (IMST). The earliest forms of S-matrix theory that accounted for the non-perturbative intense-field matter interaction, are analogs of the well-known Keldysh-Faisal-Reiss (KFR) model, also called Strong-Field Approximation (SFA), in which the interaction with laser field is emphasized [10, 9, 11]. The IMST which has been developed to extend this model has been used to study multiphoton ionization from outer and inner valence shells of diatomic and polyatomic molecules [46, 47, 30, 48, 49, 50]. However, e.g. the ionization saturation intensity for polyatomic molecules

calculated based on IMST only qualitatively agrees with experimental results. This suggests that ionization from these molecules might show a breakdown of single-active-electron approximation. To investigate such multielectron systems, quantum dynamical version of the configuration interaction (CI) and multiconfiguration self-consistent field (MCSCF) methods of electronic structure calculations have been developed. These interesting approaches, time-dependent CI with single excitations (TD-CIS) [51, 52, 53] and time-dependent Hartree-Fock (TDHF) [54] as well as multiconfiguration time-dependent Hatree-Fock (MCTDHF) [55, 56, 57, 58], are able to treat the correlated motion of many electrons in nonequilibrium situations. However, they were only applied to small or artificial model molecules. Another promising method is time-dependent density-functional theory (TDDFT) [59, 60, 61, 62, 63, 64], which in principle has the ability to describe strong field processes for polyatomic molecules. Otobe and Yabana [59] have studied ionization of benzene and acetylene with TDDFT for the first time. The method has also been applied by Castro et al. [60, 65, 66, 67, 68] and Chu et al. [69, 70, 71, 72] for smaller molecules such as hydrogen molecule, nitrogen molecule, sodium dimer, and helium trimer.

The TDDFT method does not only provide a way to study multielectron system such as large molecules but also gives access to inner valence orbitals in order to investigate their roles in a specific mechanism. In the following sections, the basic concepts within TDDFT are going to be reviewed. More detailed information is available at [73, 74, 75, 76, 77, 78].

2.1 Multielectron system

In quantum mechanics, a multielectron system with N electrons can be described fully by its wavefunction $\Psi(t, \mathbf{r}_1, \mathbf{r}_2, \cdots, \mathbf{r}_N)$ which satisfies the multielectron Schrödinger equation in time dependent form

$$i\hbar\frac{\partial}{\partial t}\Psi(t, \mathbf{r}_1, \mathbf{r}_2, \cdots, \mathbf{r}_N) = \left[\sum_{i=1}^{N}\left(-\frac{\hbar^2\nabla_i^2}{2m} + v(\mathbf{r}_i) + v^{laser}(t, \mathbf{r}_i)\right) + \sum_{i<j=1}^{N} U(\mathbf{r}_i, \mathbf{r}_j)\right]\Psi(t, \mathbf{r}_1, \mathbf{r}_2, \cdots, \mathbf{r}_N), \tag{2.1}$$

or time-independent form

$$\left[\sum_{i=1}^{N}\left(-\frac{\hbar^2\nabla_i^2}{2m}+v(\mathbf{r}_i)\right)+\sum_{i<j=1}^{N}U(\mathbf{r}_i,\mathbf{r}_j)\right]\Psi(\mathbf{r}_1,\mathbf{r}_2,\cdots,\mathbf{r}_N)=E\Psi(\mathbf{r}_1,\mathbf{r}_2,\cdots,\mathbf{r}_N), \tag{2.2}$$

where $U(\mathbf{r}_i,\mathbf{r}_j)$ is the electron-electron interaction which has the form

$$\hat{U}=\sum_{i<j=1}^{N}U(\mathbf{r}_i,\mathbf{r}_j)=\sum_{i<j=1}^{N}\frac{e^2}{|\mathbf{r}_i-\mathbf{r}_j|} \tag{2.3}$$

for a Coulomb system, where we defined an operator $\hat{U}$ for the electron-electron interaction. Similarly, we can define a kinetic energy operator for the electrons

$$\hat{T}=\sum_{i=1}^{N}-\frac{\hbar^2\nabla_i^2}{2m} \tag{2.4}$$

and nuclear-electron interaction energy

$$\hat{V}=\sum_{i=1}^{N}v(\mathbf{r}_i)=\sum_{i,k}\frac{-Q_k e}{|\mathbf{r}_i-\mathbf{R}_k|} \tag{2.5}$$

where Q_k and $\mathbf{R}_k$ are the nuclear charge and nuclear position of k^{th} nuclei, respectively. The interaction between electron and external laser field is included in the term $v^{laser}(t,\mathbf{r}_i)$. In the time-dependent multielectron Schrödinger equation (2.1), we ignored the motion of the nuclei and its interaction with the laser field, since the time-scale of the motion for nuclei is very large compared to the motion of electrons. Thus, the whole wavefunction that describes both nuclei and electrons can be decomposed into two parts: one for nuclei and one for electron, which leads to Eq. (2.1) satisfied by the electron wavefunction. Such approximation is called Born-Oppenheimer approximation [79]. Although the computation power has been improved dramatically over the last decades, it is still impossible to solve the multielectron Schrödinger equation (2.1) directly for more than two-electron systems in realistic time. An alternative approximation method is TDDFT, an extension of density-functional theory (DFT), which provides rather precise results within realizable computing time. Before going to TDDFT, we first look at the Hohenberg-Kohn theorem which establishes the foundation of DFT.

2.2 The Hohenberg-Kohn theorem

DFT is based on the Hohenberg-Kohn (HK) theorem [80] which states that the ground state of a system is uniquely determined by its ground state one-electron density

$$n_o(\mathbf{r}) = N \int d\mathbf{r}_2 \int d\mathbf{r}_3 \cdots \int d\mathbf{r}_N \Psi_o^*(\mathbf{r}, \mathbf{r}_2, \mathbf{r}_3 \cdots \mathbf{r}_N)\Psi_o(\mathbf{r}, \mathbf{r}_2, \mathbf{r}_3 \cdots \mathbf{r}_N), \tag{2.6}$$

where the subscript o refers to ground state. This means $\Psi_o(\mathbf{r}, \mathbf{r}_2, \mathbf{r}_3 \cdots \mathbf{r}_N)$ is a functional of the density and thus all ground-state observables are functionals of the one-electron density $n_o(\mathbf{r})$. Hohenberg and Kohn showed in their paper [80] that if Ψ_o was not determined by the ground state density n_o, then there is a contradiction to the variational principle. The HK theorem has been scrutinized carefully over the years, for example, M. Levy [81] and E. Lieb [82] proposed independently constrained-search proof of the theorem. A strong form of the Hohenberg-Kohn theorem was discovered and given by [83, 84, 85]

$$\int d\mathbf{r} \Delta n(\mathbf{r}) \Delta v(\mathbf{r}) < 0, \tag{2.7}$$

which means we cannot keep either the change of external potential $\Delta v(\mathbf{r})$ or the change of ground state density $\Delta n(\mathbf{r})$ to be zero when the other is changed. So, the HK theorem gives the following conceptual relationship

$$n_o(\mathbf{r}) \rightarrow v(\mathbf{r}) \rightarrow \Psi_o(\mathbf{r}_1, \mathbf{r}_2, \cdots, \mathbf{r_N}), \tag{2.8}$$

which says that the ground density uniquely determines the potential which uniquely determines the ground state of the system. Based on the above information, the ground state wavefunction is a functional of the ground state density

$$\Psi_o(\mathbf{r}_1, \mathbf{r}_2, \cdots, \mathbf{r}_N) = \Psi[n_o(\mathbf{r})] \tag{2.9}$$

and thus any observable of the ground state is also a functional of $n_o(\mathbf{r})$

$$O[n_o(\mathbf{r})] = \langle \Psi[n_o(\mathbf{r})] | \hat{O} | \Psi[n_o(\mathbf{r})] \rangle. \tag{2.10}$$

One of the important observables is total energy

$$E[n_o] = T[n_o] + U[n_o] + V[n_o]. \tag{2.11}$$

2.3 Kohn-Sham equation

Since the system is uniquely determined by the electron density, it is sufficient to determine the correct electron density to calculate any interesting physical quantities. The electron density can be obtained by solving the multielectron Schrödinger equation. However, if it would be possible to obtain it from an auxiliary single-particle Schrödinger equation, then the computation cost would dramatically decrease. Fortunately, such auxiliary equation exists and it is called Kohn-Sham equation. Before the derivation of the Kohn-Sham equation, let us first consider a system of noninteracting electrons in external potential $v_s(\mathbf{r})$.

$$\begin{aligned} \hat{H} &= \hat{T} + \hat{V}_s \\ \hat{V}_s &= \int d\mathbf{r} n(\mathbf{r}) v_s(\mathbf{r}) \end{aligned} \tag{2.12}$$

The ground state wavefunction Ψ_o of the N-particle system can be approximated by a Slater determinant

$$\Psi_o = \frac{1}{\sqrt{N!}} \det \begin{pmatrix} \phi_1(\mathbf{r}_1) & \cdots & \phi_N(\mathbf{r}_1) \\ \vdots & & \vdots \\ \phi_1(\mathbf{r}_N) & \cdots & \phi_N(\mathbf{r}_N) \end{pmatrix} \tag{2.13}$$

where orbital $\phi_i(\mathbf{r}_i)$ is the solution of single-particle Schrödinger equation for the i^{th} particle

$$-\frac{\hbar^2}{2m}\nabla^2\phi_i(\mathbf{r}_i) + v_s(\mathbf{r}_i)\phi_i(\mathbf{r}_i) = \varepsilon_i\phi_i(\mathbf{r}_i). \tag{2.14}$$

For simplicity, the subscript i presents both spatial and spin quantum numbers. The ground state density of the N-noninteracting-particle system is given by

$$n_{os}(\mathbf{r}) = \sum_{i=1}^{N} |\phi_i(\mathbf{r})|^2, \tag{2.15}$$

in which, subscript s is added to differentiate it from the true interacting system. The total energy of the system is

$$E_{os} = \sum_{i=1}^{N} \int d\mathbf{r} \phi_i^*(\mathbf{r}) \frac{(-\hbar^2\nabla^2)}{2m} \phi_i(\mathbf{r}) + \int d\mathbf{r} v_s(\mathbf{r}) n_{os}(\mathbf{r}). \tag{2.16}$$

According to HK theorem, we already know E_{os} and the second term on the right of Eq. (2.16) is a functional of density, then the term for kinetic energy should also be an functional of density. This implies that the orbital is a functional of the ground state energy

$$\phi_i = \phi_i[n_{os}]. \tag{2.17}$$

Now, assume that for a real interacting system with external potential $v_{ext}(\mathbf{r})$, its ground state density $n_o(\mathbf{r})$ can be obtained from the ground state density of some noninteracting system with a single-particle external potential $v_s(\mathbf{r})$ (related but different from $v_{ext}(\mathbf{r})$). In this way, it transforms the problem from solving a multielectron Schrödinger equation to several non-interacting single-particle Schrödinger equations, and thus it significantly reduces the computation time. The question whether such a corresponding single-particle potential $v_s(\mathbf{r})$ exists for any arbitrary density is called v-representability problem and has been early recognized [86]. This is a very important question because HK theorem only guarantees that there cannot be more than two potentials for each density but it does not guarantee that such a potential exists for a given density. Fortunately, it is known that for discretized system the density is ensemble v-representable. A density is said to be ensemble v-representable, if there is a mix of degenerated ground states for some potential which has that density [87, 88, 89].

For an interacting system, we rewrite the exact energy of the system

$$\begin{aligned} E[n_o] &= T[n_o] + U[n_o] + V[n_o] \\ &= T_s[n_o] + U_H[n_o] + E_{xc}[n_o] + V[n_o], \end{aligned} \tag{2.18}$$

where T_s is the total kinetic energy for non-interacting system defined as

$$T_s[n_o] = \sum_i^N \int d\mathbf{r} \phi_i^*(\mathbf{r}) \frac{(-\hbar^2\nabla^2)}{2m} \phi_i(\mathbf{r}), \tag{2.19}$$

and the Hartree energy U_H is defined as

$$U_H[n_o] = \frac{e^2}{2} \int d\mathbf{r} \int d\mathbf{r}' \frac{n_o(\mathbf{r}) n_o(\mathbf{r}')}{|\mathbf{r} - \mathbf{r}'|}. \tag{2.20}$$

The exchange-correlation energy E_{xc} contains the difference $T_c = T - T_s$, which is called correlation energy, and the difference $U - U_H$. The exchange-correlation energy is usually decomposed into two parts $E_{xc} = E_x + E_c$, where E_x, the exchange energy, is due to the Pauli principle and E_c, the correlation energy, is due to correlation (T_c is only a part of E_c). The exchange energy can be expressed in terms of the single-particle orbitals

$$E_x = -\frac{q^2}{2}\sum_{jk}\int d\mathbf{r}\int d\mathbf{r}'\frac{\phi_j^*(\mathbf{r})\phi_k^*(\mathbf{r}')\phi_j(\mathbf{r}')\phi_k(\mathbf{r})}{|\mathbf{r}-\mathbf{r}'|} \tag{2.21}$$

which has no general exact expression in terms of density. The derivative of exchange-correlation energy with respect to density is called exchange-correlation potential

$$v_{xc}[n_o] = \frac{\delta E_{xc}}{\delta n_o} \tag{2.22}$$

and the exact form of this potential is unknown. By now, there exist hundreds of exchange-correlation functionals for different systems [90].

Based on the variational principle with respect to electron density, we have

$$\begin{aligned} 0 = \frac{\delta E[n_o]}{\delta n_o(\mathbf{r})} = & \frac{\delta T_s[n_o]}{\delta n_o(\mathbf{r})} + \frac{\delta V[n_o]}{\delta n_o(\mathbf{r})} + \frac{\delta U_H[n_o]}{\delta n_o(\mathbf{r})} + \frac{\delta E_{xc}[n_o]}{\delta n_o(\mathbf{r})} \\ = & \frac{\delta T_s[n_o]}{\delta n_o(\mathbf{r})} + v_{ext}(\mathbf{r}) + v_H(\mathbf{r}) + v_{xc}(\mathbf{r}), \end{aligned} \tag{2.23}$$

where $v_{ext}(\mathbf{r}) = \frac{\delta V}{\delta n_o}$ is the external potential in which the electrons move and the term $v_H = \frac{\delta U_H}{\delta n}$ is the Hartree potential. Similarly, for a system of non-interacting particles moving in a potential $v_s(\mathbf{r})$,

$$\begin{aligned} 0 = & \frac{\delta E_s[n_o]}{\delta n(\mathbf{r})} = \frac{\delta T_s[n_o]}{\delta n_o(\mathbf{r})} + \frac{\delta V_s[n_o]}{\delta n_o(\mathbf{r})} \\ = & \frac{\delta T_s[n_o]}{\delta n_o(\mathbf{r})} + v_s(\mathbf{r}). \end{aligned} \tag{2.24}$$

Comparing Eq. (2.23) and Eq. (2.24), if we set

$$v_s(\mathbf{r}) = v_{ext}(\mathbf{r}) + v_H(\mathbf{r}) + v_{xc}(\mathbf{r}), \tag{2.25}$$

then, both minimizations should yield the same density $n(\mathbf{r}) = n_s(\mathbf{r})$. Therefore, the density of the interacting many-particle system in a potential $v_{ext}(\mathbf{r})$ can be obtained by solving the equations

of a non-interacting system in potential $v_s(\mathbf{r})$, if we know the exchange-correlation potential. The orbitals of the auxiliary non-interacting system satisfy the Kohn-Sham (KS) equation

$$\left[-\frac{\hbar^2\nabla^2}{2m} + v_s(\mathbf{r})\right]\phi_i(\mathbf{r}) = \varepsilon_i\phi_i(\mathbf{r}) \tag{2.26}$$

and the density of the original system is obtained via

$$n(\mathbf{r}) = n_s(\mathbf{r}) = \sum_{i=1}^{N} f_i|\phi_i(\mathbf{r})|^2, \tag{2.27}$$

where f_i is the electron population in i^{th} orbital.

Since the Hartree potential v_H and the exchange-correlation potential v_{xc} depend on the density n and, thus, depend on the solution ϕ_i; while the solution ϕ_i is determined by the potential v_s, the KS equation (2.26) must be solved self-consistently. It usually starts with an initial guess for $n(\mathbf{r})$, followed by calculating the potential v_s, and then obtaining the solution ϕ_i, which will yield a new density $n(\mathbf{r})$. With the new density, we can start the process again until the result converges.

Once the converged ground state n_o is obtained, we can calculate any interesting quantity like the total energy

$$E_o = \sum_{i}^{N}\varepsilon_i - \frac{e^2}{2}\int d\mathbf{r}\int d\mathbf{r}'\frac{n_o(\mathbf{r})n_o(\mathbf{r}')}{|\mathbf{r}-\mathbf{r}'|} \tag{2.28}$$

or the total dipole of the system

$$\mathbf{d} = \int d\mathbf{r} n_o(\mathbf{r})\mathbf{r} \tag{2.29}$$

2.4 Time-dependent density-functional theory

So far, we have considered a static external potential only. For a system subject to a time-dependent external potential, e.g. that of a laser field, the system is described by the time-dependent Schrödinger equation

$$i\hbar\frac{\partial}{\partial t}\Psi(\mathbf{r},t) = (\hat{T}+\hat{U}+\hat{V})\Psi(\mathbf{r},t) \tag{2.30}$$

The kinetic energy $\hat{T}$ is the same as in Eq. (2.4) and the electron-electron interaction $\hat{U}$ is defined in Eq. (2.3). The external potential $\hat{V}$ not only includes the nuclear potential $\hat{V}_{ne}$ as defined in Eq.

(2.5) but also includes the external electric field which is typically of the form

$$v_{Laser} = f(t)E\sin(\omega t)\sum_{i=1}^{N}\mathbf{r}_i \cdot \alpha, \tag{2.31}$$

where α, ω, and E are polarization, frequency, and electric field amplitude of the laser. The function $f(t)$ is called pulse envelope and describes the shape of the laser pulse in time. For Eq. (2.31), there are two assumptions applied:

- The laser field is treated classically, which is valid as long as the density of photons is large and the individual quantum nature of photons can be ignored. For all simulations presented in this thesis, this is the case.

- The dipole approximation is applied, in which we assume that the wavelength of the laser field is much larger than both the size of the system and the path that is traveled by electron in one period of the laser field. Also this assumption is valid for all simulations presented in this thesis.

Similar to the static case, although the time-dependent Schrödinger equation provides an accurate description of physics, it is, however, impossible to solve it directly for multielectron system. It is, therefore, natural to ask whether the Hohenberg-Kohn theorem holds for the time-dependent case as well. Fortunately, Runge and Gross [61] have proven that if two potentials $v(\mathbf{r},t)$ and $v'(\mathbf{r},t)$ differ by more than a purely time-dependent function $c(t)$, then the time-dependent density produced with these two potentials cannot be the same:

$$v(\mathbf{r},t) \neq v'(\mathbf{r},t) + c(t) \Rightarrow n(\mathbf{r},t) \neq n'(\mathbf{r},t), \tag{2.32}$$

which implies that there exists a one-to-one mapping between the density and the external time-dependent potential. Again, such density is not obtained directly but with the auxiliary time-dependent Kohn-Sham equation

$$i\hbar\frac{\partial}{\partial t}\phi_i(\mathbf{r},t) = \left[-\frac{\hbar^2\nabla^2}{2m} + v_{ks}(\mathbf{r},t)\right]\phi_i(\mathbf{r},t), \tag{2.33}$$

where the Kohn-Sham potential is defined as in Eq. (2.25) except that the external potential includes both the nuclear potential in Eq. (2.5) and the laser field v_{laser},

$$v_{ext} = v_{nu} + v_{laser}. \tag{2.34}$$

The time-dependent density is then obtained from the time-dependent Kohn-Sham orbitals

$$n(\mathbf{r}, t) = \sum_{i=1}^{N} f_i |\phi_i(\mathbf{r}, t)|^2 \tag{2.35}$$

2.5 Exchange correlation functionals

As shown above, the Kohn-Sham equation is simple and similar to a single-particle Schrödinger equation. However, it contains a term $\nu_{xc}(\mathbf{r})$ which takes account of the multielectron effects, although its explicit formula does not exist. To make DFT and TDDFT a practical theory, different approaches are proposed to design density functionals [91]:

- Local density approximation (LDA). This group of functionals has the form

$$E_{xc}^{LDA}[n] = \int e_{xc}[n(\mathbf{r})] d\mathbf{r}, \tag{2.36}$$

  where $e_{xc}(n)$ is function of electron density only. The analytic formula is derived through analysis of the exchange-correlation energy in a system of uniform electron gas and is applied to the case of non-uniform densities directly or with empirical modifications [92, 93, 94, 78, 95].

- Density-gradient expansion (DGE). LDA is exact for a uniform electron gas and quite accurate for solids but it is less satisfactory for atoms and molecules. The natural step beyond LDA is a formal expansion of E_{xc} in gradients of the density, which was initially proposed by Hohenberg and Kohn [15]. The general form of such group of functionals is given by

$$E_{xc}^{DGE}[n] = \int \left[e_{xc}^{(0)}(n) + e_{xc}^{(1)}(n) \nabla n + e_{xc}^{(2)}(n) |\nabla n|^2 + \cdots \right] d\mathbf{r}. \tag{2.37}$$

The derivation of the coefficients $e_{xc}^{k}(n)$ is very mathematically involved [96, 97, 98, 99]. Since it is based on Taylor expansion, these functionals can only be applied for systems with very slowly-varying densities.

- Constraint satisfaction. This approach is to apply some constraints to the property of the exchange-correlation potential. DGE gives only modest improvements over LDA and the DGE functionals have the wrong analytic behavior of the exchange-correlation potential. The failure of the second-order DGE (divergence of the exchange-correlation potential, overcorrection of the correlation energy, etc) were analyzed in detail in [100, 101, 102]. Accordingly, functionals with desired analytic properties; such as the asymptotic behavior of e_{xc} and ν_{xc}, upper and lower energy bounds, density scaling transformation, etc. [103, 104, 102] were designed, which have the general form,

$$E_{xc}[n] = \int e_{xc}(n, \nabla n, \nabla^2 n, \tau, \cdots) d\mathbf{r}. \tag{2.38}$$

  To eliminate the asymptotic divergence of $v_{xc}(\mathbf{r})$, various modifications of the second-order DGE have been proposed. Most of them fall into the category of generalized gradient approximations (GGA) [103, 105, 106].

- Modeling the exchange-correlation hole. This type of functionals are designed based on the exchange-correlation hole model, forming one of the largest and most diverse groups. The general analytic form is the same as in Eq. (2.38). The exchange-correlation may be approximated by a truncated Taylor series expansion in ρ, $\nabla\rho$, $\nabla^2\rho$ or modeled from a problem that can be analytically solved [102, 107, 104].

- Empirical fits. Such group of functionals are devised by fits to experimental results for atoms and molecules with analytic forms of $E_{xc}[\rho]$ which might be borrowed from other functionals or simply postulated without derivation [108, 109]. The general form of this type of functionals is

$$E_{ex}[\rho] = \sum_k C_k \int e_{xc}^{(k)}(\rho, \nabla\rho, \nabla^2\rho, \tau, \cdots; a_k, b_k, \cdots) d\mathbf{r}, \tag{2.39}$$

where C_k,a_k,b_k,$\cdots$ are fitting parameters.

- Mixing exact and approximation exchange. These functionals are also called hybrid functionals and have the form

$$E_{xc}^{hybrid}[\rho] = \int \left[a e_x^{exact}(\mathbf{r}) + b(e_x^{DFT}(\mathbf{r}) + e_c^{DFT}(\mathbf{r})) \right] d\mathbf{r}, \tag{2.40}$$

where the mixing coefficients a and b either depend on $\mathbf{r}$ or are kept constant [110, 111].

There exist hundreds of density functionals so far designed for the calculations of different systems, from atoms to molecules, from liquids to solids. There is no universal functional, so appropriate functional must be selected for a specific problem. For our simulations, we have done systematic studies to compare results for different functionals and found that LDA yields good results and is also very fast compared to application of other functionals. For more accurate results, for example in the case of ionization from atoms and molecules, it is necessary to chose functionals with correct asymptotic tail, 1/r, such as LB94 [112, 113] functionals. The following subsection is a brief introduction to LDA and LB94 functionals.

2.5.1 LDA and LB94 functionals

As mentioned above, the local density approximation (LDA) has the form

$$E_{xc}^{LDA}[\rho] = \int \rho(\mathbf{r}) \nu_{xc}[\rho] d\mathbf{r}, \tag{2.41}$$

where the exchange-correlation potential $\nu_{xc}(\rho)$ is often separated into two parts: exchange potential $\nu_x(\rho)$ and correlation potential $\nu_c(\rho)$. They can be obtained from the theory of a uniform electron gas.

The details about the derivation of the exchange energy for a uniform electron gas are analyzed by Bloch [92] and Dirac [93]. The exact LDA exchange formula for a uniform electron gas is

$$E_x^{LDA}[\rho] = -C_x \int \rho^{4/3}(\mathbf{r}) d\mathbf{r}, \tag{2.42}$$

where $C_x = \frac{3}{4}\left(\frac{3}{\pi}\right)^{1/3}$. The correlation energy is more complicated than the exchange energy because the exact analytic form of the correlation energy can only be derived for two limiting cases. The first one is the high-density (weak correlation) limit of a spin-compensated uniform electron gas

$$\nu_c = A_{GB} \ln r_s + B + r_s(C \ln r_s + D), \tag{2.43}$$

where r_s is defined as

$$r_s = \left(\frac{3}{4}\rho\right)^{1/3} \ll 1, \tag{2.44}$$

which is interpreted as the radius of a sphere that contains the charge of one electron. Gell-Mann and Brueckner [114] evaluated the coefficients A_{GB} and B, while Carr and Maradubin [115] evaluated C and D. For the low-density (strong correlation) case, Nozières and Pines [116] and Carr [117] obtained the correlation energy in the form of

$$\nu_c(r_s) = \frac{1}{2}\left(\frac{U_o}{r_s} + \frac{U_1}{r_s^{3/2}} + \frac{U_2}{r_s^2} + \cdots\right), r_s \gg 1, \tag{2.45}$$

where U_k are known constants. The exact form for intermediate densities is unknown and the value was obtained through Monte Carlo simulations for uniform electron gas by Ceperley and Alder [118]. In order to connect the low density and high density form as well as to reproduce the value for the intermediate density range, Perdew and Zunger [119] proposed the following fitting formula,

$$\nu_c(r_s) = \begin{cases} \dfrac{\gamma}{1 + \beta_1 r_s^{1/2} + \beta_2 r_s} & \text{if } r_s \geq 1 \\ A \ln r_s + B + C r_s \ln r_s + D r_s & \text{if } r_s < 1 \end{cases}, \tag{2.46}$$

where γ, β_1, β_2, A, B, C, and D are parameters. There also exist some other fitting formulas proposed by Vosko et al. [120] and Perdew et al. [106]. In our simulations, Eq. (2.46) is used and we obtain high accuracy results in comparison with experiments.

One shortage of LDA is the fast decay of atomic potential which does not have correct asymptotic behavior, namely $1/r$. This is however important to obtain accurate results for ionization. To improve it, Leeuwen and Baerends [112] proposed a model of exchange potential that has the correct $1/r$ potential tail:

$$\nu_{xc}^{LB}(\alpha, \beta; \mathbf{r}) = \alpha \nu_x^{LDA}(\mathbf{r}) + \nu_c^{LDA}(\mathbf{r}) - \frac{\beta x_\sigma^2(\mathbf{r}) \rho^{1/3}(\mathbf{r})}{1 + 3\beta x(\mathbf{r}) \ln\{x(\mathbf{r}) + [x^2(\mathbf{r}) + 1]^{1/2}\}}, \tag{2.47}$$

where the last term in Eq. (2.47) is the gradient correction with $x(\mathbf{r}) = |\nabla\rho(\mathbf{r})|/[\rho(\mathbf{r})]^{4/3}$, which ensures the proper asymptotic behavior. The parameters $\alpha = 1$ and $\beta = 0.05$ were obtained by a fit to the exact exchange-correlation potential for the beryllium atom.

2.6 The pseudopotential approximation

For large systems, like large molecules and solids, the concept of pseudopotential (PP) is usually applied so that only the wavefunction for valence electrons is explicitly calculated. The idea is that only valence electrons participate in chemical bonding in molecules and solids, while the inner electrons remain as an atomic-like configuration and their orbitals do not change too much, if the environment of the atom is changed. Such technique leaves only the valence electron density to be determined in the self-consistent cycle for the system which greatly reduces the computation time.

The effective potential in the original KS equation is $v_s[n] = v_{ext}[n] + v_H[n] + v_{xc}[n]$, where the density is the full electron density $n(\mathbf{r})$ of the system. Using the pseudopotential, the electron density is replaced with the density of valence electrons $n_v(\mathbf{r})$. The effect of core electrons is taken into account by replacing the external potential v_{ext} with a pseudopotential v_{ext}^{PP}. Therefore,

$$v_s^{PP}[n_v] = v_{ext}^{PP} + v_H[n_v] + v_{xc}[n_v]. \tag{2.48}$$

The pseudopotential v_{ext}^{PP} can be obtained by applying the following steps:

(1) Determine an effective pseudopotential v_s^{PP} so that the single-particle wavefunction from v_s^{PP} agrees with the valence wavefunction obtained from the all-electron KS equations outside a cut-off radius r_c for the same atom. In other words, the valence orbital densities obtained through these two approaches are the same.

(2) Then the pseudopotential for the atom is equal to

$$v_{ext}^{PP} = v_s^{PP} - v_H[n_v] - v_{xc}[n_v]. \tag{2.49}$$

There are many methods to generate the effective pseudopotential v_s^{PP}. The most popular methods were proposed by Troullier and Martines [121], Bachelet, Hammann and Schlüter [74], Kleinman and Bylander [122], and Vanderbilt [123]. Nowadays one can generate the pseudopotential with these methods through the open source program atomic pseudopotential engine (APE) [73].

2.7 Implementation of TDDFT

To solve the Kohn-Sham equation (2.33), the wavefunction is discretized in both space and time with uniform spacing step Δx and time step Δt, which converts the Kohn-Sham equation into a matrix equation. The initial wavefunction can be obtained by solving the eigenvalue problem self-consistently. An initial guess is needed to start the self-consistent process. For molecules, the initial Kohn-Sham orbital is usually obtained as a linear combination of atomic orbitals. Such atomic orbitals usually implemented are pseudo-orbitals that are used to generate the pseudopotential [124].

Once the initial ground state orbitals are obtained, the wavefunction of each orbital is propagated forward with the method called enforced time-reversal symmetry (ETRS),

$$\phi_{n+1}(\mathbf{r}) = exp(-i\Delta t H_{n+1}/2) exp(-i\Delta t H_n/2)\phi_n(\mathbf{r}). \tag{2.50}$$

It depends on the term H_{n+1} which can only be known exactly via the solution ϕ_{n+1}. The way to avoid such problem is to estimate the exact solution by performing $\phi^*_{n+1} = \exp(-i\Delta t H_n)\phi_n$ and then set $H_{n+1} = H_{n+1}[\phi^*_{n+1}]$

In general, in our simulations, the propagation time step and spatial grid spacing are set to 0.03 a.u. and 0.3 a.u., respectively. There is a relationship for the propagation time step Δt and spatial spacing Δx which must be satisfied in order to get stable results

$$2\frac{(\Delta x)^2}{\Delta t} > \pi. \tag{2.51}$$

The condition is based on the following argument. The maximum energy determined by the grid spacing is $\frac{k^2_{max}}{2} = \frac{1}{2}\left(\frac{\pi}{\Delta x}\right)^2$, while the maximum energy determined by the time step is $E_{max} = \frac{\pi}{\Delta t}$,

and it requires $E_{max} > \frac{k_{max}^2}{2}$ to keep the propagation to be stable which yields the relationship of Eq. (2.51).

When a laser field is applied, an atom or molecule can be ionized and some part of the wavefunction then propagate toward the boundary which will lead to reflection and unphysical effects. Therefore, such ionized wavepacket from the system should be absorbed once it reaches the boundary of the simulation box. There are two types of absorbing boundaries. One procedure is to multiply the wavefunction at each time step with a so-called mask function. The mask function is a function with value 1 for the region outside the absorbing region, decaying from 1 to 0 inside the absorbing boundary. The other method is to add an imaginary potential in the absorbing boundary region. The wavefunction inside the region of imaginary potential is then damped and thus absorbed. To compare the effect of these two boundaries, we have performed simulations for 1-D H atom in a 800 nm laser field with intensity of 1×10^{14} W/cm^2 using these two boundaries. In both cases, the simulation box size and absorbing boundary width are set to 92 a.u and 13 a.u., respectively. Results are presented in Fig. 2.1. For mask absorbing boundary (left), the wavefunction shows a strong interference pattern due to the interference between out-going wavepacket and reflected wavepacket from boundary while for imaginary absorbing potential (right), there is no interference pattern because the out-going wavepacket is well absorbed without reflection.

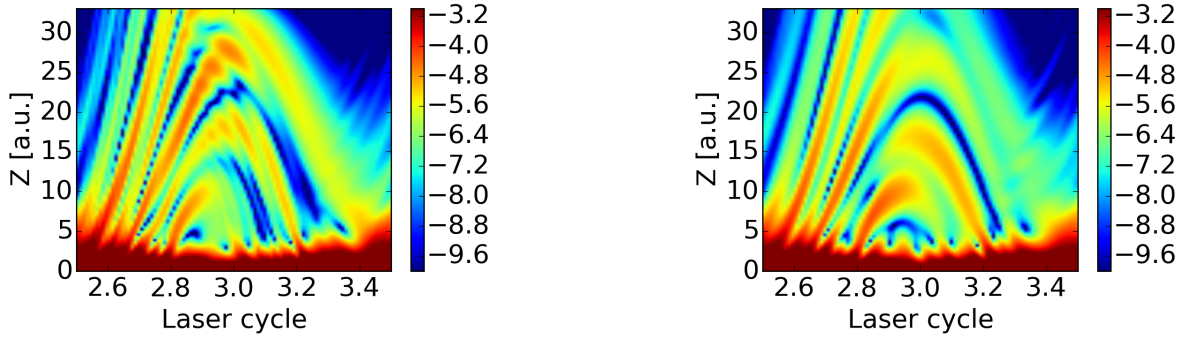

Figure 2.1: Density plots for H atom in a 800 nm laser field at intensity of 1×10^{14} W/cm^2 with mask function (left) and imaginary absorbing potential (right).

The pseudopotential we used is the Martine-Troullier pseudopotential [121]. The simulation with TDDFT is carried out in two stages: first, we perform a DFT calculation to obtain the ground state, and then we start TDDFT calculation by propagating each Kohn-Sham orbital in the laser field. Although self-consistent calculations should be carried out for each time step, these are actually not performed at each time step due to the computational costs. The results are however checked by comparing with those for smaller time step. In each time step, information like eigenvalue, laser induced dipole, population, projection of each orbital are calculated and stored for analysis.

2.7.1 Comparison of exchange-correlation functionals

In this thesis, the physical quantities we are interested in include spectra of high harmonic generation and ionization yield. So, we mainly compared results for this two properties obtained with LDA and LB94 exchange-correlation functionals. As an example, we first compare the ionization yield from N_2 at 400 nm for these two functionals in Fig. 2.2. The LB94 functional has a correct tail, 1/r, and thus the ionization is not as strong as that for the LDA functional. However, the relative ionization yields from valence orbitals are nearly the same for both functionals. So unless we are interested in comparing ionization yield with experimental results, LDA is already good enough to give us insights in a physical mechanism. The high harmonic generation spectra

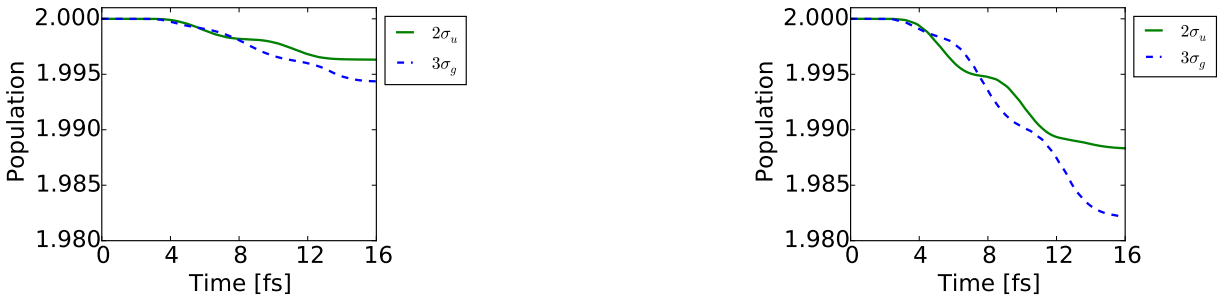

Figure 2.2: Comparison of population from valence orbitals of N_2 between LB94 (left) and LDA (right) functionals. Laser field is at wavelength of 400 nm and intensity of 5×10^{13} W/cm^2. Only the relevant KS orbitals which possess an important response to the laser field are shown with their labels.

obtained with LDA and LB94 functional are also compared for the same laser parameters, as shown in Fig. 2.3. Although the ionization yields from the two functionals have different values, the am-

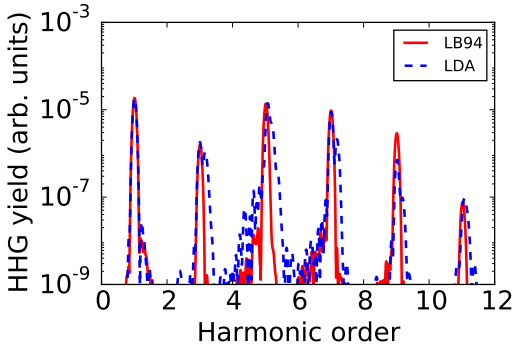

Figure 2.3: Comparison of high harmonic spectra of N_2 for LDA and LB94 functionals. Laser field is at wavelength of 400 nm and intensity of 1×10^{14} W/cm^2 with polarization parallel to the molecular axis.

plitudes of each high harmonic order are nearly the same. As we will discuss later, at wavelength of 400 nm, the laser field will induce a coupling between HOMO-2 ($2\sigma_u$) and HOMO ($3\sigma_g$) for parallel orientation. We therefore also looked at the projection between the two coupled orbitals to see if the two different functionals give us the same Rabi flopping behavior. The comparison is presented in Fig. 2.4. For both functionals, we see an oscillation of projections with nearly

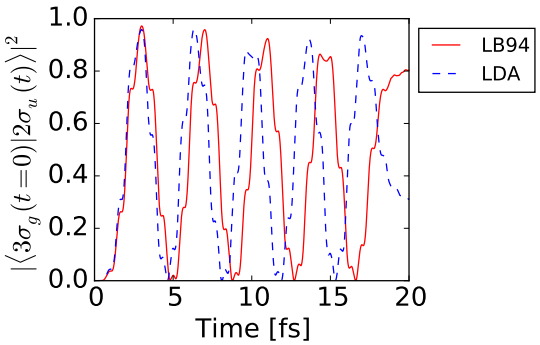

Figure 2.4: Projection between coupled orbitals of N_2 in a 400 nm laser field at intensity of 1×10^{14} W/cm^2 for LDA and LB94 functionals.

the same period. The small difference in the period comes from a slightly different eigenvalue of orbitals calculated with the two functionals. Based on these comparisons, we conclude that LDA

in general , is sufficient for the calculation presented in this thesis, since we are mainly interested in identifying multielectron effects in laser induced process. If it turns out to be necessary to compute using LB94 functional, we will show the comparison in detail between these two functionals in the corresponding Chapter.

Chapter 3

Multielectron effects in high-order harmonic generation from molecules

High-order harmonic generation (HHG) is one of the highly nonlinear nonperturbative processes in intense laser field science. It was first observed for neon gas by McPherson et al. [5] in 1987. Typically, HHG is generated by focusing an ultrashort, high-intense, near-IR laser pulse into a noble gas at intensities of about 10^{14} W/cm^2. The intensity spectra of high harmonics emitted by an atom reveal some characteristic features. Perturbation theory predicts that the intensities of the first few harmonics rapidly decreases with the increasing order of harmonics [125]. However, the experimental observations and calculations with non-perturbation theories show that the typical spectrum of the harmonic intensities has a fast initial decay followed by a region with fairly constant harmonic intensities, which is called 'plateau'. At the end of the plateau is the so-called cutoff, beyond which the harmonic intensity drops dramatically.

Over the last three decades, HHG has progressed dramatically, becoming a very active research topic [126, 35, 127]. One application of HHG is to serve as table-top XUV light source. By now, the plateau of HHG can be extended to keV regime [16, 17]. The ultrabroad bandwidth of the spectra makes it possible to produce attosecond pulses, which can in principle be used to detect electron dynamics directly at its natural time scale. This opened a new research area: attosecond science [128, 18, 19, 20]. HHG itself contains information about the electronic structure of the target and therefore it is extensively used to study the dynamics in atoms and molecules[129, 130, 131, 132]. As a spectroscopic tool, HHG is successfully applied to image static and dynamic properties of molecules and solid state materials [133, 134, 135, 136, 137, 32]. Molec-

ular imaging with HHG became an important topic, since Itatani et al. [39] have shown that HHG may be exploited to tomographically image the highest occupied molecular orbital (HOMO) for diatomic molecules. Concerning bigger molecules, there have also been performed experiments on HHG for butane, propane and and on allene and acetylene [138]. Going to larger molecules was motivated by the possibilities of imaging of molecules within HHG. One of the problems, that can be met in pursuing this goal is related to the fact that in larger molecules one can have interferences between electron wavepackets that can be traced to different orbitals. Several experiments [33, 32, 34, 139] indeed suggest that electrons from more than one orbital contribute during such process.

In the non-perturbative intensity regime it is a great challenge to do theoretical analysis for interaction with multielectron systems. Without the machinery of perturbation theory one is forced to compromise. One of the most popular approaches assumes the Single-Active-Electron (SAE) approximation. Methods used within this approximation range from tunneling theories, the so called strong field approximation (also called Lewenstein approximation) to numerical solutions of Schrödinger equation with effective single-electron potential modeling the rest of the molecule. The approaches like tunnel theory and strong field approximation were very successful for atoms. Clearly, these approaches do not include multielectron effects or electron correlation.

In this Chapter, we are going to analyze multielectron effects in the HHG spectra from molecules using TDDFT framework. In particular, we consider the spectra at driving laser frequency matching the energy difference of orbitals in molecules.

3.1 Classical and semi-classical description of HHG

3.1.1 Three-step model

HHG can be understood using the semiclassical three-step model [140, 141] as shown in Fig. 3.1 (left). In the first step, an intense laser field tilts the Coulomb potential and an electron can tunnel through the barrier into the continuum, then the free electron is accelerated by the laser field.

When the laser field reverses direction, the electron can return to the parent ion, and recombine emitting excess energy in the form of high-order harmonic photon. Such process occurs every half-cycle and it produces a pulse train of radiation. A simple semiclassical theory based picture captures not only HHG properties but also other interesting phenomena, such as non-sequential ionization [142] and above threshold-ionization (ATI) [143].

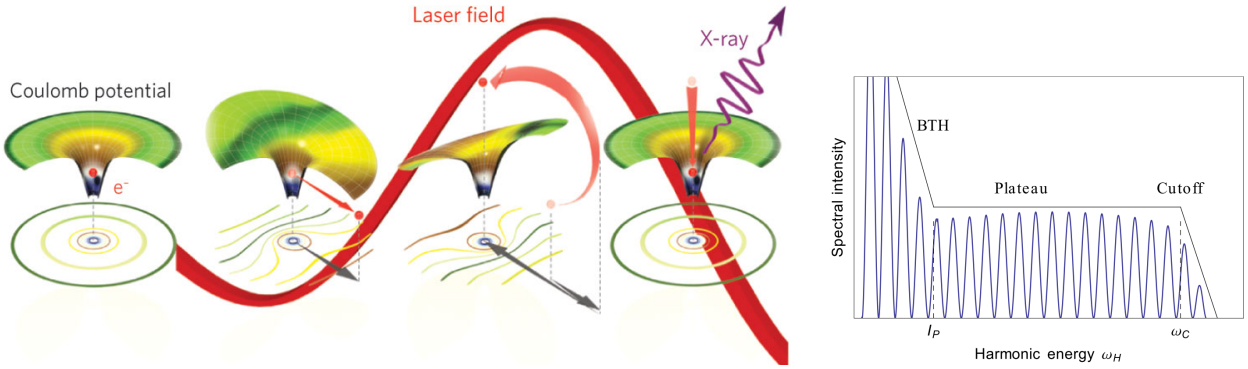

Figure 3.1: Three step model for high-order harmonic generation (left) and typical harmonic spectra from noble gas atom (right), adapted from [144].

The generated harmonic spectra have particular characteristic features as shown in Fig. 3.1(right). The harmonic intensity decays quickly as a function of harmonic order followed by a region with fluctuating but fairly constant intensity, which is called a *plateau*. The plateau ends with the so called *cutoff*, where the harmonics intensities drop several orders of magnitude. The cutoff can be estimated based on the classical formula [140, 141]

$$E_{cutoff} = I_p + 3.17U_p \tag{3.1}$$

where I_p is the ionization potential and $U_p = \frac{e^2E^2}{4m\omega_o^2}$ is the ponderomotive potential, which is defined as the average kinetic energy of a free electron in a linearly polarized electric field with amplitude E and frequency ω_o.

Since HHG is a quantum process, its description is contained in the solution of the time-dependent Schrödinger equation (TDSE). In general, the solution of TDSE is however very time consuming. Therefore, models, in particular those using the strong field approximation (SFA), are

popular and discussed in the following section.

3.1.2 Strong field approximation (SFA)

The strong field approximation is based on the following assumptions: (1) only one electron in the outermost shell is involved in HHG (SAE approximation); (2) only the ground state and continuum states are involved in the process; (3) ground-state depletion due to ionization is ignored, and (4) Coulomb interaction between electron and parent ion has no influence on the wavepacket in the continuum. Following these assumptions, we can derive the SFA formula for HHG (similar to that given in Lewenstein et al. [141]).

For an electromagnetic field applied to one electron system, the corresponding time-dependent Schrödinger equation is given by

$$i\partial_t \Psi(\mathbf{r},t) = \left[H_o + V + H_{int}\right]\Psi(\mathbf{r},t), \tag{3.2}$$

where H_o is the free particle Hamiltonian, V is the Coulomb potential, and H_{int} is the interaction between the particle and laser field which has the form, $H_{int} = e\mathbf{E}\cdot\mathbf{r}$ in length gauge and $H_{int} = -\frac{e}{m}\mathbf{p}\cdot\mathbf{A} + \frac{e^2}{2m}A^2$ in velocity gauge. The exact solution has the form,

$$\Psi(t,\mathbf{r}) = \Psi_o(t,\mathbf{r}) + \int_{-\infty}^{\infty} G(t,t')H_{int}(t',\mathbf{r})\Psi_o(t',\mathbf{r})dt', \tag{3.3}$$

where $\Psi_o(t,\mathbf{r})$ is the initial (ground) state. $G(t,t')$ is the Green's function describing the propagation from t' to t. Inserting Eq. (3.3) back into Eq. (3.2) shows that the Green's function satisfies the equation,

$$i\partial_t G(t-t') = (H_o + V + H_{int})G(t-t') + \delta(t-t'). \tag{3.4}$$

The exact solution depends on the potential V. Let us now approximate the solution by ignoring the effect of Coulomb potential, V, in a strong field. The solution corresponding to the propagation of a free particle in the presence of laser field has the form,

$$G(t,t') = -i\Theta(t-t')G_o(t-t'), \tag{3.5}$$

where the step function $\Theta(t-t')$ arises due to the function $\delta(t-t')$ in Eq. (3.4). Then G_o satisfies the equation,

$$i\partial_t G_o = (H_o + H_{int})G_o. \tag{3.6}$$

This equation can be solved in velocity gauge,

$$i\partial_t \Psi(\mathbf{p},t) = \frac{1}{2}(\mathbf{p} - e\mathbf{A})^2 \Psi(\mathbf{p},t), \tag{3.7}$$

with

$$\Psi(\mathbf{p},t) = C\exp(-\frac{i}{2}\int_{-\infty}^{t}(\mathbf{p} - e\mathbf{A}(t''))^2 dt''), \tag{3.8}$$

and can be transferred back to the space domain giving,

$$\Psi_{\mathbf{p}}^{V}(\mathbf{r},t) = C\exp\{i\mathbf{p}\cdot\mathbf{r} - \frac{i}{2}\int_{-\infty}^{t}(\mathbf{p} - e\mathbf{A}(t''))^2 dt''\}, \tag{3.9}$$

which is called Volkov state [145]. The coefficient C can be obtained through normalization condition,

$$\langle\Psi(\mathbf{r},t)|\Psi(\mathbf{r},t)\rangle = \delta(\mathbf{p} - \mathbf{p}'). \tag{3.10}$$

The solution in velocity gauge is then given by,

$$\Psi_{\mathbf{p}}^{V}(\mathbf{r},t) = \frac{1}{(2\pi)^{3/2}}\exp\left\{i\mathbf{p}\cdot\mathbf{r} - \frac{i}{2}\int_{-\infty}^{t}(\mathbf{p} - e\mathbf{A}(t''))^2 dt''\right\}. \tag{3.11}$$

The solution in length gauge can be obtained through the gauge transformation:

$$\mathbf{A} = \mathbf{A} + \nabla\chi \tag{3.12}$$

$$\phi = \phi' - \frac{\partial}{\partial_t}\chi \tag{3.13}$$

$$\Psi(\mathbf{r},t) = \Psi'(\mathbf{r},t)\exp\left[i\chi(\mathbf{r},t)\right]. \tag{3.14}$$

In order to have $\phi = e\mathbf{E}\cdot\mathbf{r}$ and $\mathbf{A} = 0$, we set $\chi = -e\mathbf{A}\cdot\mathbf{r}$. Thus, the solution in length gauge is equal to,

$$\Psi_{\mathbf{p}}^{V}(\mathbf{r},t) = \frac{1}{(2\pi)^{3/2}}\exp\left[i\left(\mathbf{p} - e\mathbf{A}\right)\cdot\mathbf{r} - \frac{i}{2}\int_{-\infty}^{t}\left(\mathbf{p} - e\mathbf{A}(t'')\right)^2 dt''\right] \tag{3.15}$$

$$= \frac{1}{(2\pi)^{3/2}}\exp\left[-\frac{i}{2}\int_{-\infty}^{t}\left(\mathbf{p} - e\mathbf{A}(t'')\right)^2 dt''\right]|\mathbf{p} - e\mathbf{A}\rangle, \tag{3.16}$$

where

$$|\mathbf{p} - e\mathbf{A}\rangle = \exp\left[i(\mathbf{p} - e\mathbf{A}) \cdot \mathbf{r}\right]. \tag{3.17}$$

Thus, the approximated Green's function then is

$$G^V(t,t') = -i\Theta(t-t') \int d^3p |\Psi_{\mathbf{p}}^V(t)\rangle\langle\Psi_{\mathbf{p}}^V(t')|. \tag{3.18}$$

Inserting the Green's function back into Eq. (3.3), we get

$$\Psi(t,\mathbf{r}) = \Psi_o(t,\mathbf{r}) + \int_{-\infty}^{\infty} G^V(t,t') H_{int}(t',\mathbf{r}) \Psi_o(t',\mathbf{r}) dt'. \tag{3.19}$$

The time-dependent laser induced dipole of the system can then be evaluated as

$$\mathbf{d}(t) = \langle\Psi|(e\mathbf{r})|\Psi\rangle = \langle\Psi_o|(e\mathbf{r})|\Psi_o\rangle + \int_{-\infty}^{\infty} dt' \langle\Psi_o(t)|(e\mathbf{r}(-i\Theta(t-t')G(t,t')^{(V)}))H_{int}|\Psi_o(t')\rangle + c.c., \tag{3.20}$$

where the terms containing the second and higher orders of H_{int} are ignored. The first term is constant or zero while the second term is the interesting part and gives information about the induced oscillating dipole. We denote it as

$$\begin{aligned}
\mathbf{I} =& \int_{-\infty}^{\infty} dt' \langle\Psi_o(t)|(e\mathbf{r}(-i\Theta(t-t')G^V(t,t')))H_{int}|\Psi_o(t')\rangle \\
=& e^2 i \int d\mathbf{p} \int_{-\infty}^{t} dt' \langle\Psi_o(t)|\mathbf{r}|\Psi_p^V(t)\rangle \mathbf{E}(t') \cdot \langle\Psi_p^V(t')|\mathbf{r}|\Psi_o(t')\rangle \\
=& e^2 i \int_{-\infty}^{t} dt' \int d\mathbf{p} \mathbf{D}^*(\mathbf{p} - e\mathbf{A}(t),t) \mathbf{E}(t') \cdot \mathbf{D}(\mathbf{p} - e\mathbf{A}(t'),t') \\
& \times \exp\left[-i \int_{t'}^{t} dt'' \left(\frac{1}{2}\left(\mathbf{p} - e\mathbf{A}(t'')\right)^2 + I_p\right)\right] \\
=& e^2 i \int_{-\infty}^{t} dt' \int d\mathbf{p} \mathbf{D}^*(\mathbf{p} - e\mathbf{A}(t),t) \times \exp\left(iS(\mathbf{p},t,t')\right) \times \mathbf{E}(t') \cdot \mathbf{D}(\mathbf{p} - e\mathbf{A}(t'),t'),
\end{aligned} \tag{3.21}$$

where the action S is defined as

$$S(\mathbf{p},t,t') = \int_{t'}^{t} dt'' \left(\frac{1}{2}\left(\mathbf{p} - e\mathbf{A}(t'')\right)^2 + I_p\right), \tag{3.22}$$

and $\mathbf{D}$ is defined as

$$\mathbf{D}(\mathbf{p} - e\mathbf{A}(t'),t') = \langle\mathbf{p} - e\mathbf{A}(t')|\mathbf{r}|\Psi_o(\mathbf{r},t')\rangle. \tag{3.23}$$

In Eq. (3.23), we recognize that $\langle \mathbf{p} - e\mathbf{A}(t')|\mathbf{r}|\Psi_o(\mathbf{r},t')\rangle$ represents the dipole moment for the transition from state Ψ_o to the continuum at time t', which is usually referred to as ionization dipole moment, while $\mathbf{D}^* = \langle \Psi_o(\mathbf{r},t)|\mathbf{r}|\mathbf{p} - e\mathbf{A}(t)\rangle$ is referred to as recombination dipole moment. The action defined in Eq. (3.22) is the phase accumulated by the wavepacket in the continuum. Based on the interpretation here, Eq. (3.21) represents the three-step model: an electron is ionized at time t' into the continuum, then propagates in the laser field and accumulates the phase S during the time period from t' to t, before it finally recombines back to the ground state Ψ_o at time t.

3.1.3 Saddle point approximation

The direct integration over $\mathbf{p}$ in Eq. (3.21) is difficult, not only because it is an integration over three dimensions but also because strong oscillations from the time dependent phase term part at large p require more precise integration method for accurate results. Saddle point approximation is often used for such oscillating integrals. It can be motivated in simple terms by noting that the highly oscillating contributions will cancel each other and only the stationary point has an influence on the result of the integral. The stationary condition for this integral is equal to

$$\nabla_{\mathbf{p}} S = \nabla_{\mathbf{p}} \int_{t'}^{t} dt''(\frac{1}{2}(\mathbf{p} - e\mathbf{A})^2 + I_p) = 0, \tag{3.24}$$

which yields that

$$\mathbf{p}_{st} = e\frac{\int_{t-\tau}^{t} \mathbf{A}(t'')dt''}{\tau}, \tag{3.25}$$

where $\tau = t - t'$. Using this approximation, and

$$\begin{aligned}\mathbf{I} \simeq & e^2 i \int_0^\infty d\tau \left(\frac{2\pi}{i\tau}\right)^{3/2} \mathbf{D}^*(\mathbf{p}_{st} - e\mathbf{A}(t), t) \times \mathbf{E}(t-\tau) \cdot \mathbf{D}(\mathbf{p}_{st} - e\mathbf{A}(t-\tau), t-\tau) \times \\ & \exp\left[-i\left(-\frac{1}{2}\mathbf{p}_{st}^2\tau + \frac{1}{2}\int_{t-\tau}^{t} \mathbf{A}^2(t'')dt'' + I_p\tau\right)\right].\end{aligned} \tag{3.26}$$

The high harmonic spectra then can be obtained as Fourier transform of the second derivative of the time-dependent dipole in Eq. (3.26) and we will compare the results obtained in this way within SFA to our TDDFT simulations later.

3.2 High-order harmonic generation from molecules

High-order harmonics are currently routinely generated from atoms. HHG can, however, also be generated from molecules and the three-step model has also been used to interpret the basic physics of the process in molecules. The study of HHG from molecules can provide a deeper understanding of the process by investigating the contribution from each step of the three-step model. For example, recent experimental [146] and theoretical [30] studies reveal that ionization rates depend on the molecular symmetry. If the other two steps do not counteract the effects in step 1, then the HHG yield will be increased when ionization is enhanced, which is confirmed by the experimental observation of high-order harmonics from aligned N_2 [39]. For step 2 and 3, one can expect quantum interferences, where the recombination amplitudes of the wavepacket at different nuclei can constructively or destructively interfere with each other as pointed out in recent experimental [147] and theoretical studies [30, 46]. Destructive interference in the HHG from diatomic molecules is well studied within the two-center interference model [148, 149, 150]. Our TDDFT simulations also reproduce such destructive interference phenomena, as it can be seen in the Fig. 3.2. The results represent the HHG spectrum from H_2^+ in an intense laser field at wavelength of 800 nm and intensity of 3×10^{14} W/cm^2. The *orientation angle*, which is the angle between molecular axis and laser polarization vector, is equal to 30^o. The two-center interference model predicts a destructive interference minimum at 31^{th} harmonic order, as can be observed in our results as well.

Another difference between atoms and molecules is that molecules are not isotropic systems. HHG spectra from an ensemble of randomly aligned molecules is often similar to those from atoms [151, 152, 153]. However, for aligned molecules, achieved through addition of a relatively weak pulse creating a rotational wave packet, HHG depends strongly on the orientation angle [147]. The alignment techniques make it also possible to use HHG as spectroscopic tool and to image orbitals. The analysis, however, often relies on approximations such as semiclassical treatment of the electron-field interaction, the single-active-electron approximation and the three-step model.

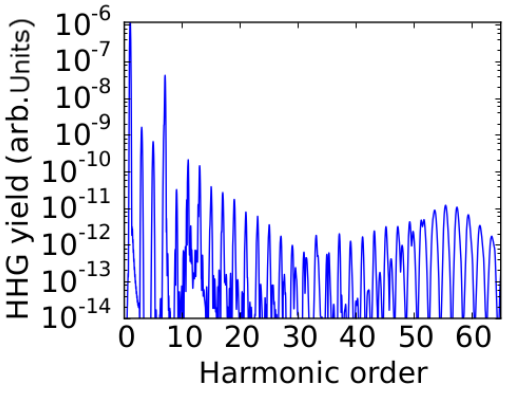

Figure 3.2: High harmonic spectra minimum due to the quantum interference from the wavefunction at the two nuclei in H_2^+. The laser field is at the wavelength of 800 nm and intensity of 3×10^{14} W/cm^2 with pulse length of 20 cycles. Molecular orientation angle is 30 degrees with respect to polarization of the laser field.

One of the example is the proposed method of tomographic imaging of molecular orbitals [39]. It is based on the single-active-electron approximation, simplified strong-field approximation in which only recombination matrix element has been extended to molecules and the neglect of the Coulomb effects. One of the attempts to extend this method by Patchkovskii et al. [32] shows that the consideration of fully anti-symmetrized multielectron wavefunctions and electron relaxation leads to a molecular orbital tomography image, that is a mix of Dyson orbital and exchange-correlation contribution from inner shells. This illustrates how extension beyond the simplest form of SFA can become rather cumbersome. Although possible, the extension still is limited by SFA in a form of separation into three steps and artificial isolation of the electron dynamics in these steps.

In recent years, it has been shown that, in particular in the case of molecules, the generated harmonic spectra often incorporate more features than predicted by the basic three-step SFA model. For example, the relevance of multielectron contributions for the interpretation of experimental data on the ellipticity of high-order harmonics from nitrogen molecules has been demonstrated [154, 155]. This results from the fact that in molecules often there are several orbitals energetically close together in the neutral molecule, as well as the cation. Therefore, the emission of electrons

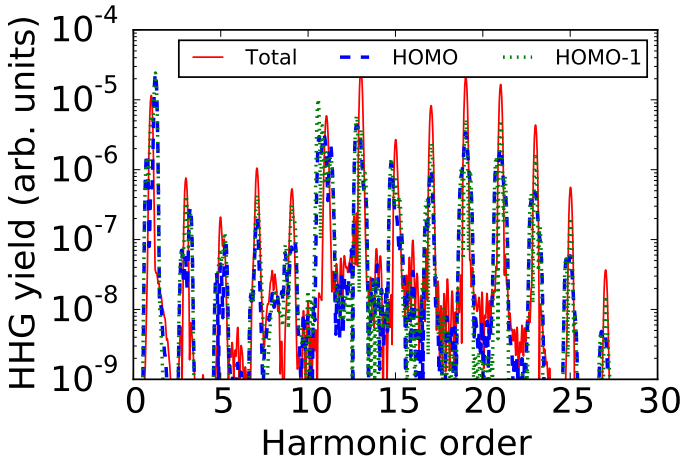

Figure 3.3: The high harmonic spectra of N_2 from its two outermost states HOMO ($3\sigma_g$) (blue dash) and HOMO-1 ($1\pi_u$) (green dots). The total spectra from these two orbitals are also plotted (red solid line). The wavelength of the laser field is 800 nm at intensity of 2×10^{14} W/cm^2 with polarization perpendicular to the molecular axis.

from different orbitals or the coupling between different orbitals during the interaction with the laser field, become more likely than in the case of atoms. For example, TDDFT results for HHG spectra from HOMO and HOMO-1 of N_2 are plotted in Fig. 3.3 and compared with the total harmonic spectra. In this case, contributions from both HOMO and HOMO-1 are comparable in the total spectrum.

In the rest of this Chapter we identify several multielectron effects in HHG from molecules. Specifically, we first predict and analyze the presence of fractional harmonics in the HHG spectra from molecules. The fractional harmonics show up as sidebands to the usual integer odd harmonics. They appear when the driving laser wavelength is tuned to the transition between one of the inner valence orbitals and a hole in the highest occupied molecular orbital (HOMO) and is, hence, most prominent in the interaction of open-shell molecular ions with intense laser radiation. We also analyze the ellipticity of HHG from N_2, CO_2 and compare our results with experimental results, yielding very good agreement after averaging over the alignment angle which accounts for imperfect alignment present and reported in experiments. The contributions from each valence orbital to the harmonic ellipticity are analyzed. Specifically, the results suggest that for N_2 rather strongly bound electrons in the HOMO-2 orbital have significant contribution to the total HHG spectra and for CO_2 nearly all valence orbitals contribute significantly to HHG process and influence the harmonics ellipticity. In our simulations, all valence orbital electrons are considered active, while the effect of all the other electrons is represented by the pseudopotential. Physical quantities like ionization, high harmonic spectrum, ellipticity, and both total and partial contributions from each orbitals are analyzed and compared. From such comparison, we can analyze the behavior of each orbital and identify the significance of their contributions to the processes.

3.3 Fractional harmonics[1]

3.3.1 Open shell molecules

In this section, we study HHG from open shell molecules in their ground states and equilibrium geometry such as N_2^+. Initial wavefunction for N_2^+ is obtained by removing one electron from the HOMO of N_2 and then by performing optimization to find the equilibrium internuclear distance and corresponding wavefunction. Generating HHG from the ion instead of the neutral molecule can be a way to extend the plateau cutoff since the ionization potential is larger. Experiments [156, 157] on HHG from ions using capillary discharged plasma, have shown that the cutoff is indeed greatly extended. Another scenario, where HHG from ions plays a role, is to study filamentation where plasma is naturally generated [158, 159].

Fig. 3.4 shows the orbitals and energy level diagram of N_2^+. The HOMO and HOMO-2 has an energy difference corresponding to wavelength of about 400 nm, while HOMO and HOMO-2 has an energy difference corresponding to 800 nm. Thus, we can study HHG from N_2^+ at typical laser wavelengths, which can couple resonantly two orbitals in the molecular ion.

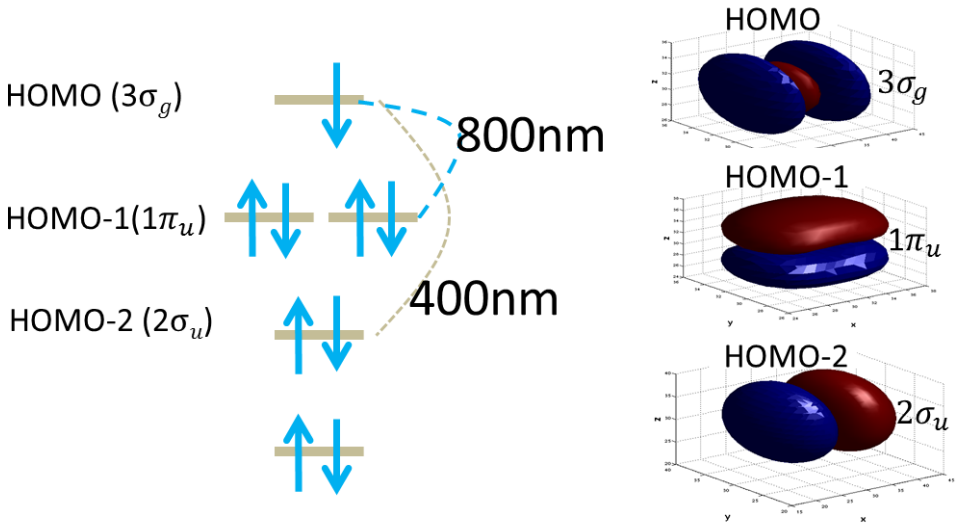

Figure 3.4: Energy level diagram (left) and orbitals (right) of the valence shell of N_2^+.

[1] Part of the results presented in this section are in Y. Xia and A. Jaron-Becker, "Mollow sidebands in high order harmonic spectra of molecules", accepted for publication

3.3.1.1 Nonadiabatic behavior of laser induced dipole

The high harmonic generation from a system can be calculated through the Fourier transform of the laser induced dipole. Within the TDDFT formalism, the calculation of laser induced dipole is equal to

$$\mathbf{d}_{tot} = \sum_i \mathbf{d}_i, \tag{3.27}$$

where $\mathbf{d}_i$ is the dipole from ith orbital,

$$\mathbf{d}_i = \langle \phi_i(t) | \mathbf{r} | \phi_i(t) \rangle = \int \mathbf{r} n_i(\mathbf{r}, t) d\mathbf{r}, \tag{3.28}$$

where $\phi_i(t)$ and $n_i(t)$ are the wavefunction and corresponding partial density for the ith orbital, respectively.

HOMO and HOMO-2 in N_2^+ have an energy gap corresponding to about 400 nm and based on the symmetry of the orbital they can only be coupled via one-photon transition, when the laser electric field is parallel to the molecular axis. In Fig. 3.5, we present the results of simulations

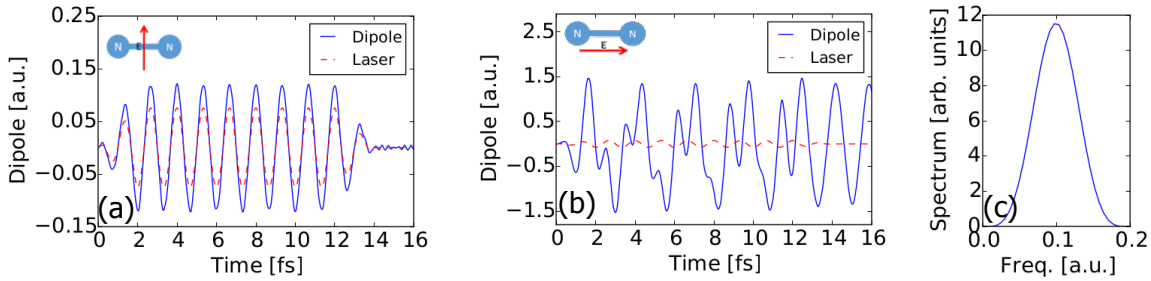

Figure 3.5: Time dependent dipole for HOMO-2 of N_2^+ for the case when the molecular axis is perpendicular (a) and parallel (b) to the laser electric field at wavelength of 400 nm and intensity of 2×10^{14} W/cm^2. The amplitude of the laser field (on arbitrary scale) is shown by dashed line for comparison. The Fourier transform spectrum of the residual dipole after the laser pulse for parallel case (b) is plotted in (c).

with a laser field set to the wavelength of 400 nm and intensity of 2×10^{14} W/cm^2 with trapezoidal envelope and pulse length of 16 fs. The laser induced dipole behaves adiabatically (i.e. following the external laser field) in (a) for perpendicular orientation but does not follow the laser field for the parallel orientation (b). The latter nonadiabatic response is due to the coupling between HOMO

and HOMO-2. This can be seen from the analysis of the dipole after the laser pulse has finished. In our simulations, we have propagated the wavefunction 3 fs after the end of the laser pulse. In Fig. 3.5, the residual dipole after laser pulse is shown: for adiabatic case it is very small (a), while it is prominent for the parallel setup (b). To confirm that such residual dipole is due to the non-zero population transfer between HOMO-2 and HOMO after the laser pulse, Fourier transform is applied to the residual dipole and a dominant peak at 0.11 a.u. (corresponding to the energy difference between HOMO and HOMO-2) in the spectrum is found as shown in Fig. 3.5(c). We will now analyze the signatures of the nonadiabatic response in the HHG spectra.

3.3.1.2 Fractional harmonics from N_2^+

Because of the relationship between HHG spectrum and the oscillating dipole,

$$P(\omega) = \frac{\omega^4}{12\pi\varepsilon_o c^3}\mathbf{d}(\omega)\cdot\mathbf{d}^*(\omega). \tag{3.29}$$

one can expect additional features in the spectrum for the coupling between orbitals. In Fig. 3.6, the spectrum for the perpendicularly oriented molecular ion at 400 nm shows the traditional spectrum consisting of odd harmonics only (panel a), while in the spectrum for the parallel aligned molecule there appear first and second order sidebands for each of the odd harmonics in the spectrum (panel b).

The sidebands do not show up at the integer multiples but at fractionals of the fundamental laser frequency and are, hence, termed "fractional" harmonics. For the present laser parameters they are related to the transition between HOMO-2 ($2\sigma_u$) to HOMO ($3\sigma_g$) in this open shell molecule. The intensity of the fractional harmonics is surprisingly high, which can be attributed to a strong transition and large transition dipole matrix element describing the coupling between these two molecular states.

The mechanism responsible for the sidebands is analogous to that for Mollow sidebands in quantum optics [160], and can be intuitively explained with the so-called dressed states. As shown in Fig. 3.7, if two states are coupled resonantly by an external laser field, they become degenerate

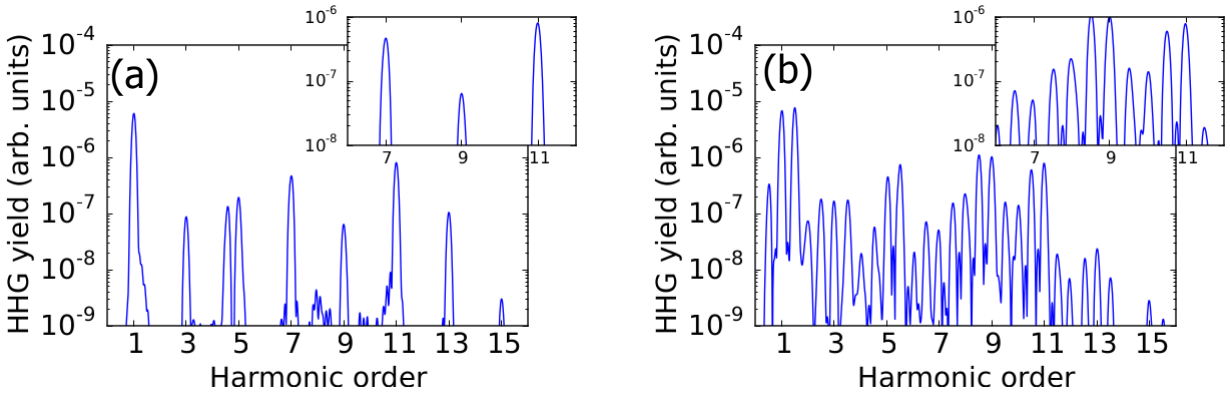

Figure 3.6: High harmonic spectra of N_2^+, aligned parallel (a) and perpendicular (b) to the polarization axis of a laser pulse at 400 nm and 2×10^{14} W/cm^2. The insets show an enlarged view of part of the spectrum, which clearly exhibit the first and second order Mollow sidebands displaced by the Rabi frequency Ω_r and $2\Omega_r$ from the odd harmonics for the aligned molecules.

and create two dressed states $|+,n\rangle$ and $|-,n\rangle$, where n is the photon number, separated by an energy of Rabi frequency. The possible transitions between these dressed states are illustrated in Fig. 3.7. There are three different possible emission energy values ω_o, $\omega_o + \Omega_r$, and $\omega_o - \Omega_r$, where Ω_r is Rabi frequency. Although in the illustration only first order sidebands are presented, higher order sidebands have also been observed in simulations and experiments [161].

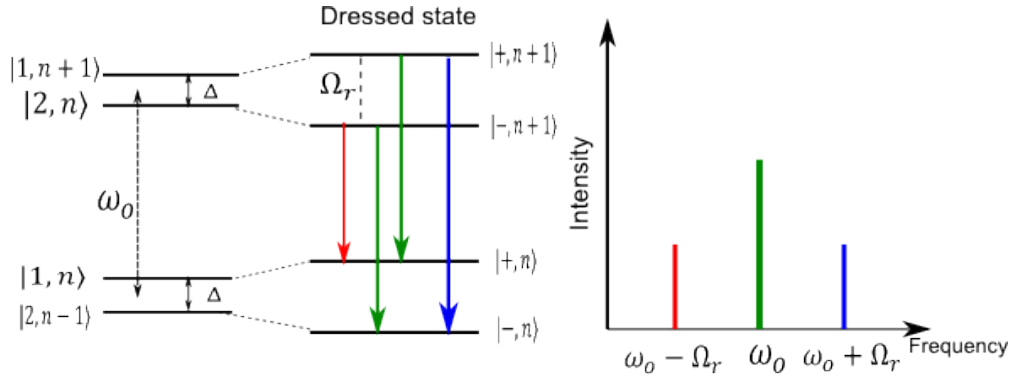

Figure 3.7: Illustration of Mollow triplets.

In the insets on the right of Fig. 3.6, we present enlarged views of parts of the spectra. These clearly show the relation between the separation of the first and second order sideband peaks in the HHG spectrum and the Rabi transition frequency Ω_r.

$$\Omega_r = \frac{\mu E}{\hbar}. \tag{3.30}$$

We studied the splitting of fractional harmonics more systematically by varying the laser field intensity, which influences the Rabi transition frequency directly and the results of simulations are shown in Fig. 3.8. One can see that the first order splitting and the calculated Rabi transition frequency are in almost perfect agreement with each other, while the second order splitting is given by the double of the Rabi transition frequency. This confirms that the fractional harmonics are strongly related to the Rabi transition frequency.

The results in Fig. 3.6 involve the transition between the same type of orbitals as in the previously studied case of H_2^+ [162], where a 1064 nm laser field is applied to couple the so-called

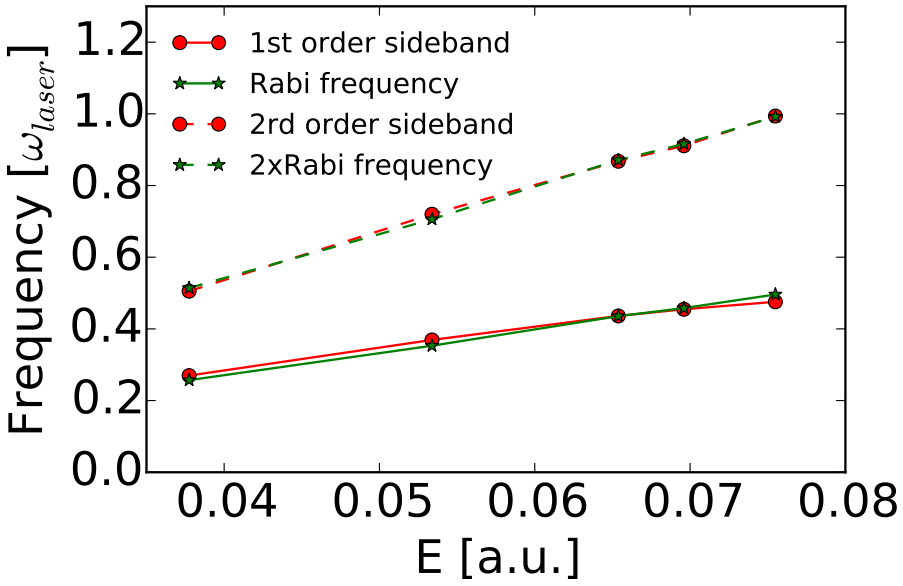

Figure 3.8: Comparison of the distance of the sideband positions, i.e. first and second order fractional harmonics, with respect to the corresponding odd harmonic (averaged over harmonics bellow 11th) and the Rabi transition frequency for different laser field intensities. Laser wavelength of 400 nm and orientation of molecule parallel to the laser field.

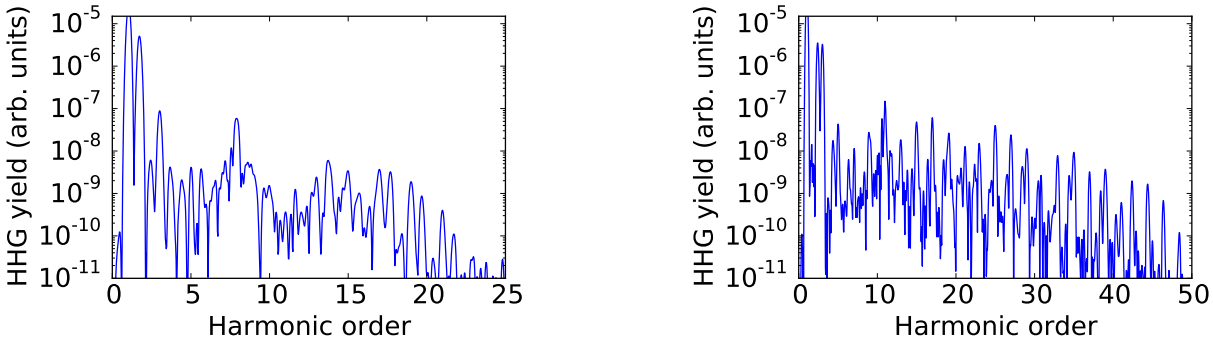

Figure 3.9: HHG spectra from N_2^+ for laser field at wavelength of 600 nm (left) with intensity of 1×10^{14} W/cm^2 and at wavelength of 800 nm (right) with intensity of 2×10^{14} W/cm^2. Molecular axis is oriented parallel to the polarization of laser field. Pulse length is 20 fs.

Charge-Resonance (CR) states HOMO ($1\sigma_g$) and Lowest Unoccupied Molecular Orbital (LUMO) ($1\sigma_u$) at stretched internuclear distances, in the regime of Charge Resonance Enhanced Ionization (CREI). In contrast, in our studies the fractional harmonics effect appears for the interaction of the molecular ion with the field at equilibrium distance and the coupling between valence orbitals, showing that the phenomenon is more general than considered before.

We have also performed simulations for the HHG spectra for laser wavelengths of 600 nm and 800 nm for the molecule aligned parallel to laser polarization vector. Because the wavelength is shifted away from the resonant wavelength 400 nm, we are entering near resonance (600 nm) and off-resonance (800 nm) cases. As can be seen in Fig. 3.9 (left), for 600 nm the fractional harmonics are still present in the spectra but are not as intense as those for 400 nm. But at 800 nm, the spectrum (Fig. 3.9 (right)) consists almost only of odd harmonics. Such simulations confirm that the fractional harmonics result from coupling between the orbitals. Since the fractional harmonics can still be seen in the near-resonant case (600 nm), the fractional harmonics should be observable in experiments, even if the laser frequency does not match exactly the energy difference between the orbitals.

Mollow sidebands in high harmonic generation have so far been predicted for the coupling between orbitals of σ-symmetry only. However, in general, the phenomenon appears for the coupling

between molecular orbitals of different type of symmetry as well. Since the symmetry of the orbitals governs the alignment dependence of the transition matrix element, the strengths of the respective fractional harmonics depends on the alignment between the molecular axis with respect to the polarization vector.

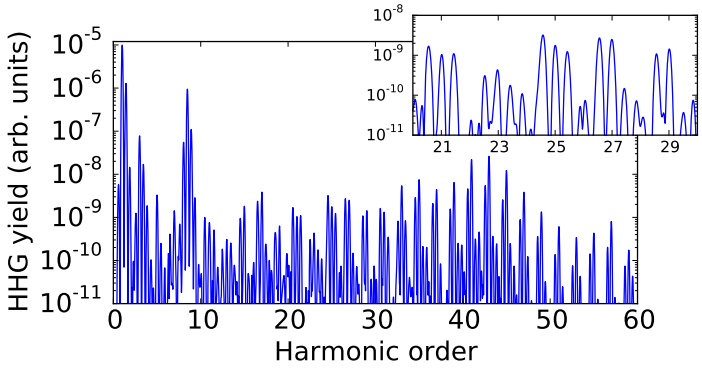

Figure 3.10: High harmonic spectrum of N_2^+ aligned perpendicular to the polarization axis of 60 fs laser pulse at wavelength of 800 nm and intensity of 2×10^{14} W/cm^2. The inset provides an enlarged view of the part of the spectrum.

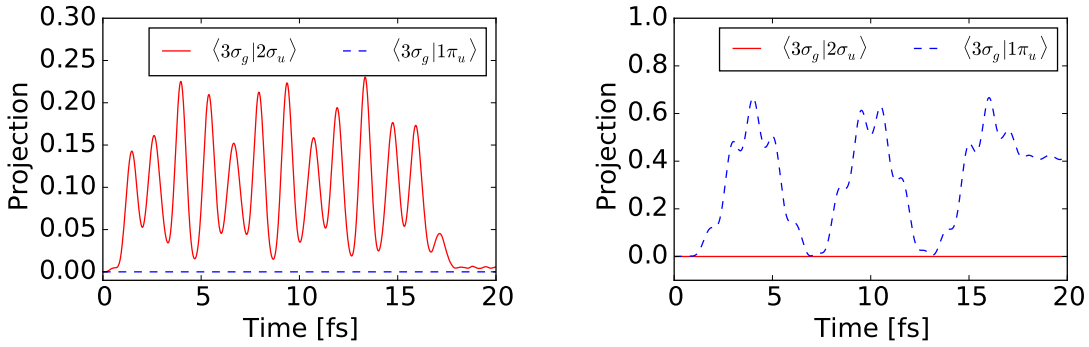

Figure 3.11: Time dependence of the projection between the coupled orbitals of N_2^+ during the interaction with the laser pulse for the case of parallel orientation (left) and perpendicular orientation (right). Laser field parameters: wavelength of 800 nm and intensity of 2×10^{14} W/cm^2.

For example, fractional harmonics due to the coupling between orbitals of π_u- (HOMO-1) and σ_g-symmetry (HOMO) in N_2^+ are induced for the interaction with a 800 nm laser pulse and perpendicular alignment of the molecule. The respective results of our calculations for the HHG spectrum in Fig. 3.10 clearly reveal the occurrence of the Mollow sidebands at these parameters.

For comparison the results for parallel orientation with the same parameters are shown in Fig. 3.9(right). One can still see small splitting which, however, comes from the weak coupling between HOMO and HOMO-2. The coupled orbitals can be identified by projecting one orbital to the other during the simulation and results are shown in Fig. 3.11. For the parallel case, the projection from HOMO-1 ($1\pi_u$) to HOMO ($3\sigma_g$) is zero while there is almost 25% population transfer between HOMO-2 ($2\sigma_u$) and HOMO. For the perpendicular case, the HOMO and HOMO-1 coupling is very strong leading to 80% population transfer between these two orbitals while the projection from HOMO-2 to HOMO in this case is nearly zero. One can conclude that the fractional harmonics for the perpendicular case arise due to the coupling between HOMO and HOMO-1 and the minor fractional harmonics for the parallel case come from weak coupling between HOMO-2 and HOMO.

3.3.1.3 Modified SFA model

Since we now understand that the fractional harmonics arise from the Rabi flopping induced by the laser field, we seek for a model to incorporate such mechanism into the strong-field approximation formalism. Suppose, the electron oscillates between the two states $|\psi_1\rangle$ and $\psi_2\rangle$ with Rabi frequency Ω_r. Then the corresponding state in the SFA model is

$$|\Phi\rangle = C_1(t)|\psi_1\rangle + C_2(t)|\psi_2\rangle, \tag{3.31}$$

where $C_1(t) = \cos(\frac{\Omega_r}{2}t)$ and $C_2(t) = -i\sin(\frac{\Omega_r}{2}t)$, which are obtained by modeling the Rabi flopping in a two-level system. By substituting Eq. (3.31) into Eq. (3.26) we obtain

$$\mathbf{I} = \mathbf{I}_{11} + \mathbf{I}_{22} + \mathbf{I}_{12} + \mathbf{I}_{21}, \tag{3.32}$$

where

$$\mathbf{I}_{ij} = \int_{-\infty}^{\infty} dt' \langle \psi_i(t) C_i(t) (-iq\mathbf{r}\Theta(t-t')) G(t,t') H_{int} C_j(t') |\psi_j(t')\rangle. \tag{3.33}$$

The four terms in Eq. (3.32) correspond to four HHG channels. The first two terms $\mathbf{I}_{11}$ and $\mathbf{I}_{22}$ represent the case, where the initial state and the final state are the same, while the last two terms, $\mathbf{I}_{12}$ and $\mathbf{I}_{21}$, represent the scenario in which the electron is ionized from one state and recombines into

the other. This model captures the resonant nature of the process and it illustrates the necessary modification of the ordinary HHG mechanism. The comparison of results from the modified SFA and the TDDFT simulations is shown in Fig. 3.12. As one can see, the modified SFA does produce the fractional harmonics at exactly the same positions as the results from TDDFT, which further confirms that the fractional harmonics are due to the coupling effect.

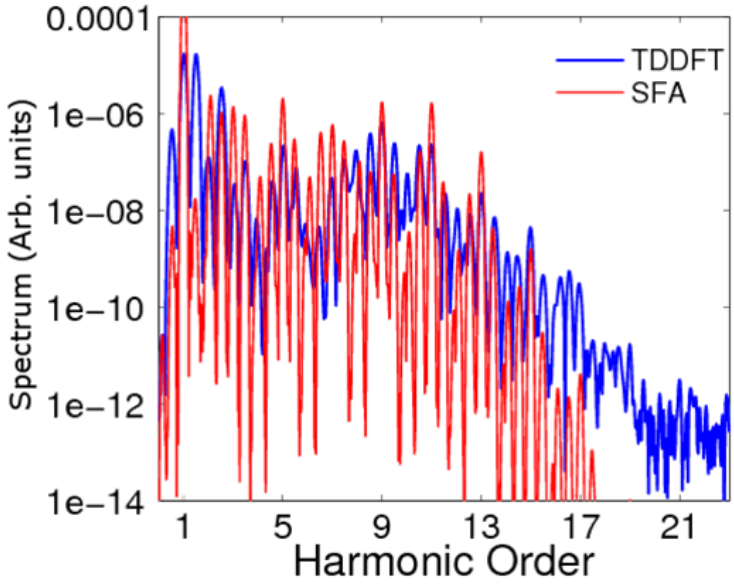

Figure 3.12: Comparison of harmonic spectra for N_2^+ calculated within modified SFA and TDDFT. Laser parameters: λ=400 nm and $I = 1 \times 10^{14}$ W/cm^2. Polarization parallel to the molecular axis.

3.3.1.4 Enhanced harmonic generation

Our TDDFT calculations also allow us to examine the harmonic spectra contributions from each orbital in N_2^+, separately. The results are shown in Fig. 3.13 for the parallel alignment case. Interestingly, the strength of high harmonics from HOMO-2 (spin up component) is much larger than those from spin down components (N_2^+ is created in our calculation by removing one spin-up electron from HOMO). This can be explained by looking at the ionization from each orbital. In Fig. 3.13(d), it can be seen that the ionization yield from spin-up HOMO-2 is much larger than ionization from other orbitals. The resonance between HOMO-2 and HOMO enhances the ionization, which is one part of the explanation. But, the ionization yield from spin-up HOMO-2

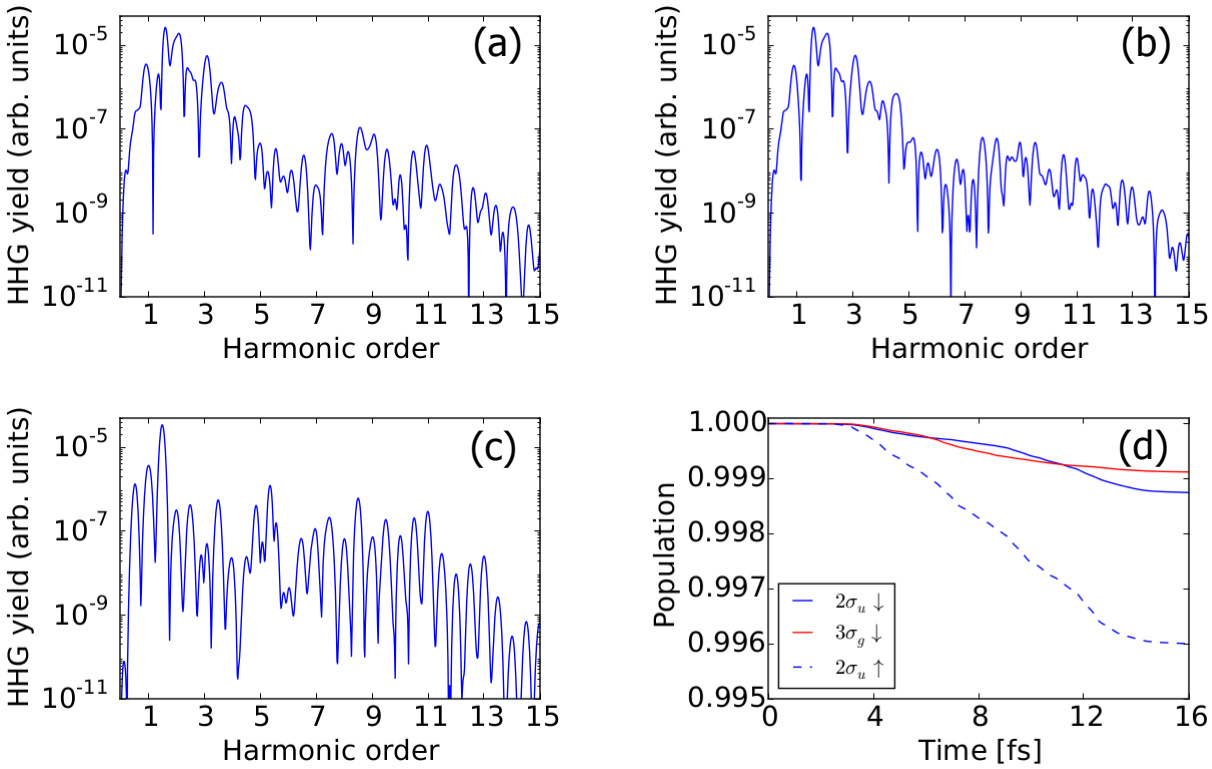

Figure 3.13: Harmonic spectra from HOMO (a) and HOMO-2 (b) of spin down component and HOMO-2 (c) of spin up component and population of coupled orbitals (d) (ionization from other orbitals is negligible). Laser field is at 400 nm and 2×10^{14} W/cm^2 with polarization parallel to the molecular axis.

should not be larger than the ionization yield from spin-down HOMO, if just a resonance process plays a role. The reason why the ionization yield for spin-up HOMO-2 is even larger than for spin-down HOMO can be found from the analysis of the orbital energies as shown in Table 3.1. For the HOMO the orbital eigenvalue is approximately equal to the vertical ionization potential.

Table 3.1: Orbital energies (eigenvalue) of N_2^+

orbital	spin down	spin up
HOMO-3($2\sigma_g$)	-1.488381	-1.465770
HOMO-2($2\sigma_u$)	-0.939705	-0.883796
HOMO-1($1\pi_u$)	-0.849458	-0.831411
HOMO($3\sigma_g$)	-0.848556	-0.779313(unoccupied)

As can be seen from the table, the spin-up HOMO's ionization potential is lower than that of the spin-down HOMO. Therefore, the spin-up HOMO-2 coupled to the spin-up HOMO has a dominant ionization yield in this case, resulting in a dominant HHG yield.

Please note that in our numerical simulations the spin-up and spin-down orbitals are not restricted to be the same. Such method is called *unrestricted open shell TDDFT* [163]. The advantage of unrestricted calculations is that they can be performed very efficiently. However, the wavefunction calculated in this way may no longer be the eigenfunction of the total spin operator $\langle S^2 \rangle$, and if that happens an error called 'spin contamination' is introduced into the calculations. The spin contamination can lead to lowering of the computed total energy because of the extra 'freedom', but more often it leads to a higher total energy since higher energy states are being mixed into the solution. Therefore it is important to check, whether such relative energy shift between spin-up and spin-down components is due to the spin contamination. The spin contamination can be checked, for example, via the calculation of $\langle S^2 \rangle$. According to [163], the total spin of spin-polarized DFT can be calculated as

$$\langle S^2 \rangle = M_s(M_s+1)\hbar^2 + \hbar^2 N_\beta - \hbar^2 \sum_{i=1}^{N_\alpha} \sum_{j=1}^{N_\beta} | \int \phi_i^\alpha(\mathbf{r}) \phi_j^\beta(\mathbf{r}) d^3r |^2. \tag{3.34}$$

For N_2^+, the value $\langle S^2 \rangle$ should be 3/4. We checked the calculations for different functionals and the relative error is less than 1% and thus we conclude that spin contamination does not have influence

on our calculations. So we can trust the energies presented in the Table 3.1.

As we mentioned before, the cutoff of HHG from ions is extended because of high ionization potential. The cutoff for HHG from N_2^+ in our simulations for the 400 nm is around 11^{th} harmonic, corresponding to $I_p = 1.0$ a.u., which means the cutoff is actually corresponding to the ionization potential of spin-up HOMO-2. Without resonance, the dominant HHG is from spin-down HOMO and thus for the cut-off, relevant ionization potential is that of spin-down HOMO. Therefore, the resonance further extends the cutoff of HHG. Because of the enhanced ionization due to resonance, it seems such a resonance is a way to enhance HHG yield and extend the cutoff simultaneously.

3.3.1.5 Nonadiabatic electron density localization

The strong coupling between the orbitals does not only leave its footprints in the high harmonic spectra, but does strongly influence the dynamics of the electron density. More specifically, the emergence of fractional harmonics comes along with profound variation of the electron dynamics inside the molecule as well as during its excursion in the continuum throughout the harmonic generation process. First, the molecular orbital coupling leads to a laser induced nonadiabatic electron dynamics in the molecule, where the electron instead of directly following the changes in the oscillating electric field experiences lags and dwells at one of the nuclei for longer than a half period of the laser field cycle. The time scale of the corresponding localization of the electron is governed, as the location of the fractional harmonics in the spectrum, by the transition frequency, i.e. Rabi frequency, and can therefore in principle be controlled via the laser parameters. This nonadiabatic dynamics can be visualized in our calculations via the difference of the time-dependent total electronic density of the propagated molecular wavepacket and the initial electron density $\rho(z,t) - \rho(z,0)$, where,

$$\rho(z,t) = \sum_{i,\sigma} \rho_{i,\sigma}(z,t) \tag{3.35}$$

with

$$\rho_{i,\sigma}(z,t) = \int dxdy|\phi_{i\sigma}(\mathbf{r},t)|^2. \tag{3.36}$$

The electron density $\rho(z,t)$ is obtained by integrating over the two spatial dimensions transversal to the molecular axis as shown in Eq. (3.36). We present the resulting density for N_2^+ as a function of the electron position along the internuclear axis and as a function of time in Fig. 3.14. The laser

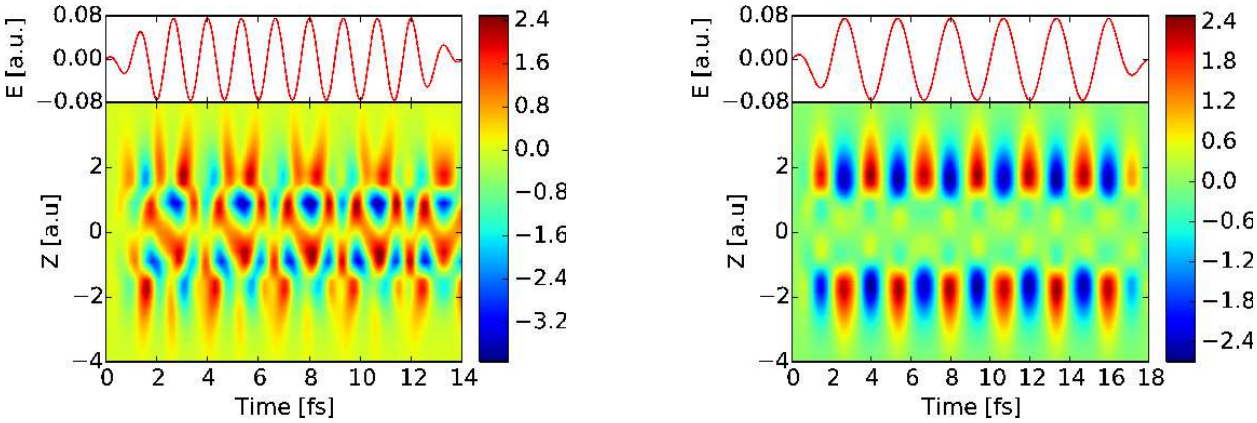

Figure 3.14: Difference between the full time-dependent electron density of N_2^+, aligned along (left) and perpendicular (right) to the polarization of laser, and the initial electron density as a function of time and the position along the molecular axis. The density is integrated over the spatial dimensions transversal to the molecular axis. Laser parameters as in Figure 3.6.

parameters and the orientation of the molecular axis (along the electric field vector) are the same as for the results in Fig. 3.6. For the purpose of comparison the electric field is included at the top. For the sake of comparison, we present changes in the density difference for the case where no coupling is present (right) and one can observe typical adiabatic dynamics.

The result clearly shows that in the Rabi flopping regime the electron density does not swap adiabatically from one side of the molecular ion to the other every half cycle of the electric field (left). Instead dynamical localization islands can be observed along the internuclear axis in particular. However, also the electron density localized around nuclei shows nonadiabatic behavior. For adiabatic case (right) one can typically observe changes in electron density primarily around the nuclei. The frequency of the associated nonadiabatic oscillation is estimated to be approximately equal to the Rabi frequency of the transition between the two states of σ-symmetry. We will further explore the nonadiabatic dynamics in Chapter 5 of this thesis.

3.3.1.6 Modification of the time-frequency analysis of HHG

Since the Rabi flopping induces additional dynamics during the HHG process, we would like to investigate the HHG process in time domain in more details. Time-frequency analysis (also called wavelet analysis) is such a tool which makes it possible to examine how high harmonic generation changes with time. The time-frequency spectra is obtained through formula Eq. (3.37)

$$\mathbf{d}(\omega,\tau) = \int \mathbf{d}(t)\exp(-(\tau-t)^2/2\sigma^2)\exp(-i\omega\tau)dt. \tag{3.37}$$

In time-frequency analysis, instead of performing fast Fourier transform (FFT) directly to the laser induced dipole, a Gaussian type function $\exp(-(\tau-t)^2/2\sigma^2)$ is added, which constraints the FFT only to be applied to the dipole in the time window defined by the Gaussian function. The result of the time-frequency analysis for nonresonant case is presented in Fig. 3.15. From the Figure

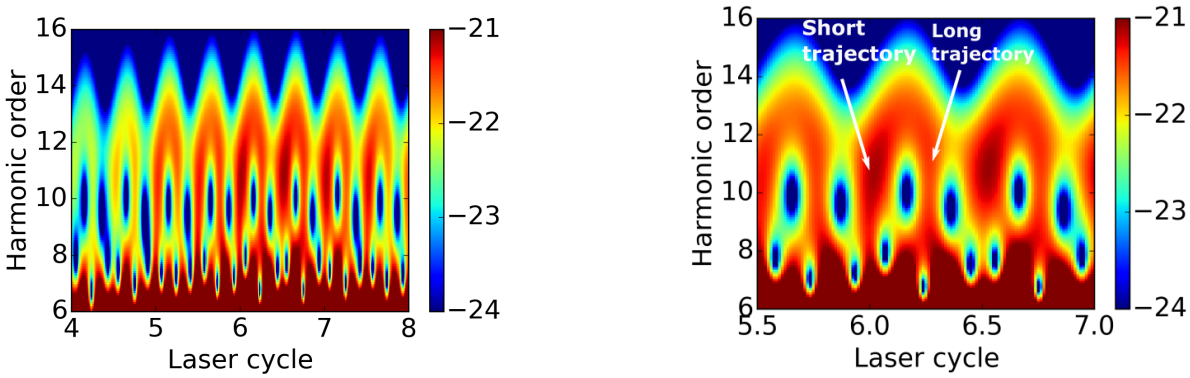

Figure 3.15: Wavelet analysis of high harmonic generation in N_2^+ aligned perpendicular to the polarization direction of laser field. Laser parameters are the same as in Fig. 3.6.

we can see that there is a HHG burst during every half laser cycle. For each harmonic order, there are two recombination times, which are related to two types of trajectories recognized from classical calculations. In typical time frequency analysis the pattern has "lambda" type shape, where the left 'arm' is corresponding to short trajectories, while the right one is corresponding to long trajectories, as indicated in Fig. 3.15(right)

The nonadiabatic electron dynamics in the molecule leads to modifications of this traditional semiclassical picture of HHG, as can be seen from the time frequency analysis in Fig. 3.16. In

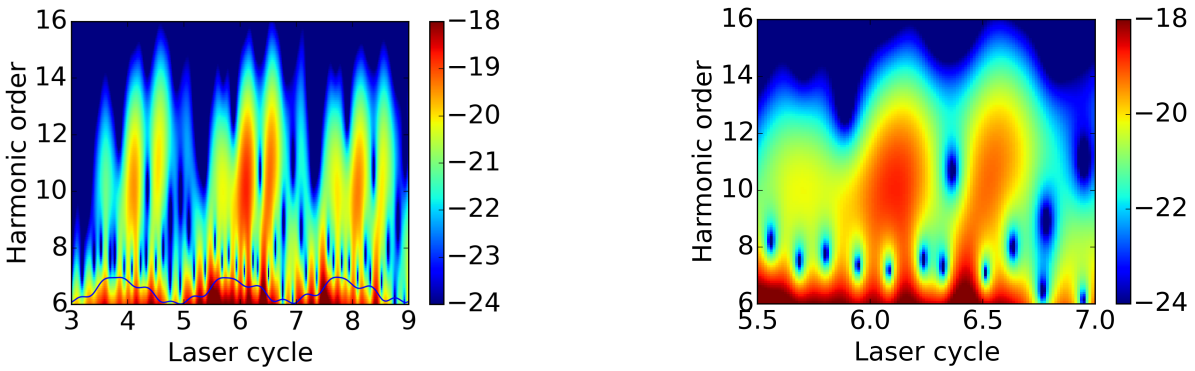

Figure 3.16: Wavelet analysis of high harmonic generation in N_2^+ aligned parallel to the polarization direction of the laser field. Laser parameters are the same as in Fig. 3.6.

contrast to the typical wavelet analysis for high harmonic generation, which exhibits the return of the electron and harmonic emission via short and long trajectories, the generation of the frequencies in the harmonic spectrum as a function of time in this case is more complex. Obviously, any interpretation in terms of classical paths becomes cumbersome. Instead, the time-frequency pattern is modulated by the nonadiabatic dynamics and temporal variation of the electron localization inside the molecule and, not surprisingly, shows an oscillating variation of the pattern with the time scale related to the transition frequency between HOMO and HOMO-2 in the nitrogen molecular ion, which is shown overimposed in the lower part of spectrum in Fig. 3.16(left).

3.3.1.7 Fractional harmonics from other molecules

Present section is devoted to illustration that our findings are not restricted to the nitrogen molecular ion. Indeed, from the results of our calculations we observe the appearance of fractional harmonics in other larger open shell molecules as well, like CO_2^+, $C_2H_4^+$, and NO_2.

CO_2^+

The valence shell electron configuration of CO_2^+ is $(3\sigma_g)^2(2\sigma_u)^2(4\sigma_g)^2(1\pi_u)^4(3\sigma_u)^2(1\pi_g)^3$. To induce coupling, we find that the $1\pi_u$ and $1\pi_g$ can be coupled at parallel orientation with a wavelength around 350 nm, which is available in experiments. The coupled orbitals are shown in Fig. 3.17. The harmonic spectra for both coupling and non-coupling case are shown in Fig. 3.18.

(a) $1\pi_u$ (b) $3\sigma_u$ (c) $1\pi_g$

Figure 3.17: Orbital image of CO_2.

The coupling between orbitals is very strong, leading to appearance of intense fractional harmonics

(left panel) for parallel case, while for the perpendicular case the harmonic spectrum is regular and presents odd harmonics only (right panel).

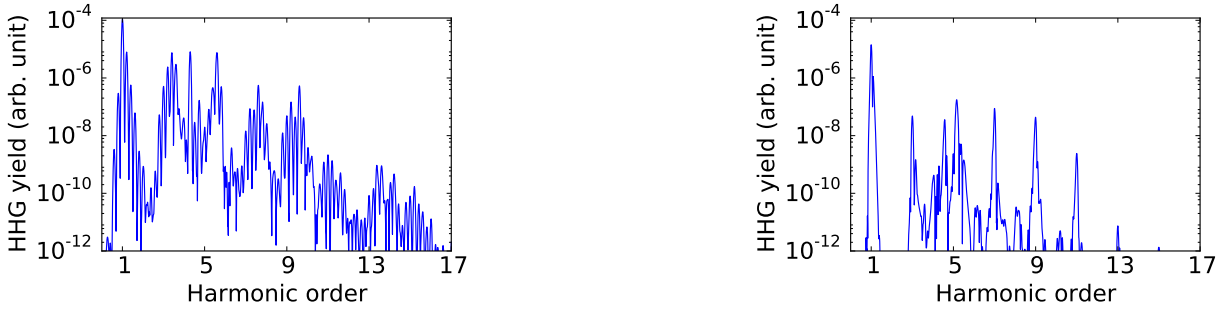

Figure 3.18: Fractional harmonics from CO_2^+ with laser field at wavelength of 350 nm and intensity of 1×10^{14} W/cm^2 at parallel (left) and perpendicular orientation (right).

$\mathbf{C_2H_4^+}$

While the previously studied cases are for the coupling between inner valence shell orbitals and HOMO, in $C_2H_4^+$ two inner valence orbitals can be coupled. One electron is removed from $1b_{3g}$, which leaves the electron configuration as $(2a_g)^2(2b_u)^2(1b_{2u})^2(3a_g)^2(1b_{3g})^1(1b_{3u})^2$. With a 400 nm laser field, a coupling can be induced between $1b_{2u}$ and $1b_{3g}$. The orbital images of $C_2H_4^+$ of the coupled orbitals are shown in Fig. 3.19. We analyze the generated harmonic spectrum with driven

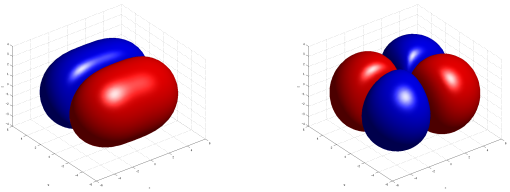

(a) $1b_{2u}$ (b) $1b_{3g}$

Figure 3.19: Orbital images of C_2H_4.

laser field at 400 nm with polarization parallel to the axis along carbon-carbon bond. Fractional harmonics are present again due to the coupling, but since the coupling is not as strong as in CO_2^+ and N_2^+, only first order splitting fractional harmonics are observed in this case, shown in Fig.

3.20(left). For the case where laser polarization is perpendicular to the carbon-carbon bond, only odd harmonics are present.

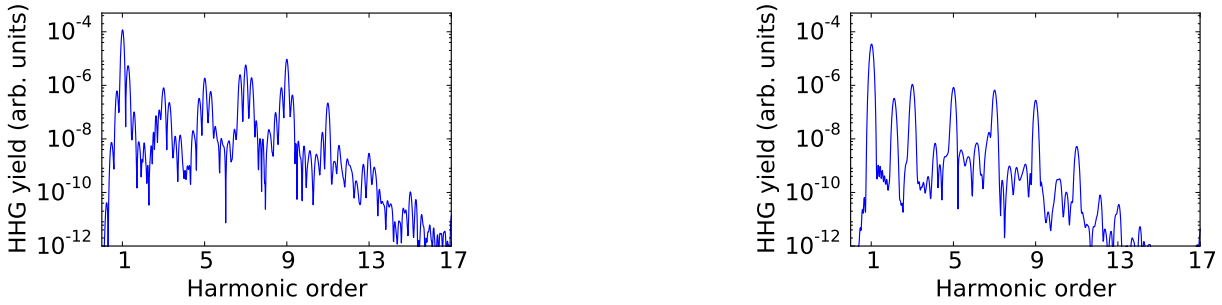

Figure 3.20: Fractional harmonics from $C_2H_4^+$ with laser field at wavelength of 400 nm and intensity of 1×10^{14} W/cm^2 with polarization parallel (left) and perpendicular (right) to the C-C bond.

NO_2

Open shell molecules can be created by removing an electron from neutral molecules, which is, however, difficult for experimentalists to obtain. We, therefore, selected also a neutral open shell molecule NO_2 in our studies, which has the electron configuration as $(5a_1)^2(1b_1)^2(1a_2)^2(4b_2)^2(6a_1)^2$, where the orbital $6a_1$ is partially occupied. The valence orbitals' images are presented in Fig. 3.21. Considering the nonlinear geometry, it is interesting to see if the fractional harmonics are still present. A laser at 400 nm with intensity of 10^{14} W/cm^2 is applied to couple the orbital $4b_2$ and the orbital $6a_1$ with polarization parallel to the oxygen-oxygen bond. The coupling is, however, not very strong. Instead of separated peaks in the spectrum, we therefore get a broadening of each odd harmonics, as shown in Fig. 3.22.

3.4 Ellipticity of high-order harmonics [2]

Since the high-order harmonic generation has recently become an important XUV source [17], the ellipticity of HHG is particularly interesting for experimentalists because the control of ellipticity for soft-X ray is very difficult compared to lasers at wavelengths within the visible light

[2] Parts of the results in this section are published in Y. Xia and A. Jaron-Becker, "Multielectron contributions in elliptically polarized high-order harmonic emission from nitrogen molecules", Opt. Lett. 39, 1461 (2014).

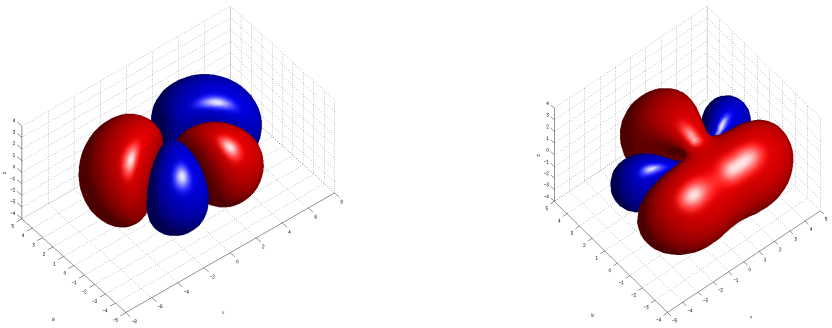

(a) $4b_2$ (b) $6a_1$

Figure 3.21: Orbital images of NO_2.

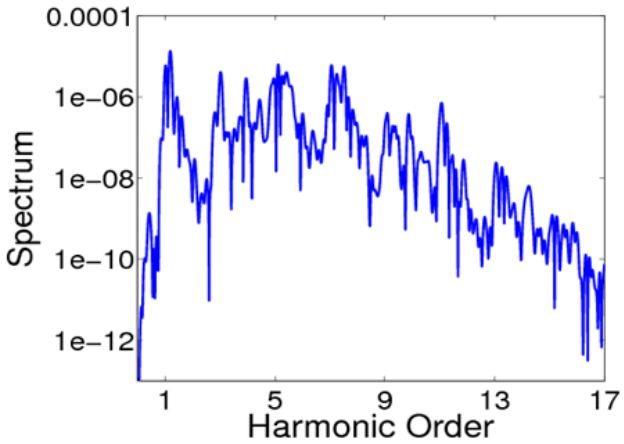

Figure 3.22: Fractional harmonics from NO_2 with laser field at wavelength of 400 nm and intensity of 2×10^{14} W/cm^2 with polarization direction parallel to the oxygen-oxygen axis.

range. It would be appealing, if specific elliptically polarized laser light can be generated from the source directly. Since atoms are spherically symmetric systems, the generated HHG from noble gas atoms by linearly polarized laser field is also linearly polarized. HHG from molecules, however, is naturally elliptically polarized because of the non-spherical symmetric orbital. Recent experiments have shown that elliptically polarized HHG can be obtained from molecules N_2 and CO_2 [164, 165].

In this section we present results of numerical calculations for the polarization and ellipticity of high-order harmonics from molecules like H_2^+, H_2, N_2, and CO_2. We show that for simple one-electron system, the ellipticity has a large value for harmonics at angles where destructively interference occurs. The ellipticity pattern for larger molecules is more complex and multielectron effects start to play a role. For multielectron systems, our calculated ellipticity of high-order harmonics from N_2 and CO_2 are in good agreement with the data of recent experiments [164, 154] and reveal the importance of multielectron contributions for N_2, where at least three different orbitals (HOMO, HOMO-1, and HOMO-2) have influence on the ellipticity and for CO_2, where nearly all valence electron orbitals play a role. In particular, we show that the contributions from inner-valence orbitals are most significant at wavelengths at which there is a resonance between two orbitals. Furthermore, we confirm that it is essential to take proper account of the alignment of the internuclear axis with respect to the polarization direction in the molecular ensemble.

3.4.1 Ellipticity from one-electron system H_2^+

The high harmonic spectrum $d(\omega)$ is obtained through fast Fourier transform of the laser induced dipole $\mathbf{d}(t)$, see Eq. (3.27). For linear molecules, the laser induced dipole usually has two components: the parallel and perpendicular components categorized by the direction with respect to the direction of the laser electric field. The ellipticity of a given harmonic is determined by [166, 150]

$$\epsilon = \sqrt{\frac{1 + r^2 - \sqrt{1 + 2r^2\cos(2\delta) + r^4}}{1 + r^2 + \sqrt{1 + 2r^2\cos(2\delta) + r^4}}}, \tag{3.38}$$

where r is the amplitude ratio of perpendicular component to parallel component

$$r = |d_\perp(\omega,\alpha)| \,/\, \left|d_\parallel(\omega,\alpha)\right|, \tag{3.39}$$

and δ is the relative phase between the two components,

$$\delta = \arg\left[d_\perp(\omega,\alpha)\right] - \arg\left[d_\parallel(\omega,\alpha)\right]. \tag{3.40}$$

From Eq. (3.38), the maximum ellipticity occurs when the amplitude ratio r=1 and the relative phase $\delta = 90^o$, which means the strength of perpendicular component $d_\perp$ has to be comparable to the parallel component $d_\parallel$. This however is usually not satisfied because the electron oscillates strongly along the laser field and thus produces strong parallel and weak perpendicular components.

We first study the ellipticity of HHG from the simplest one-electron system H_2^+. In Figure 3.23 with a laser field at wavelength of 800 nm and intensity of 3×10^{14} W/cm^2, which is also investigated by Chu et al. [150], we compare the amplitude and phase difference of parallel and perpendicular components of 57^{th} harmonic. With the change of alignment angle of molecular axis to the laser polarization axis, the parallel component has a minimum around 50^o while the perpendicular component has a maximum value around the same angle and comparable to the parallel component, which indicates $r \approx 1$ around 50^o. On the other hand, the phase difference changes dramatically from -0.6π to 0.4π. Based on our analysis, we therefore expect maximum ellipticity around 50^o while close to zero elsewhere.

The angle of 50^o for this harmonic actually corresponds to the occurrence of an interference minimum for parallel component at this harmonic according to the two center interference model where minimum occurs when

$$d\cos\theta = (n + \frac{1}{2})\lambda. \tag{3.41}$$

Here d is the internuclear distance and λ is wavelength of ionized electron wavepacket. If the wavefunction has different sign on the two center, then 1/2 should be dropped. According to the analysis, we would expect the maximum ellipticity will occur around the interference minimum of the individual harmonics in HHG of H_2^+, as shown in Figure 3.24. It can be seen that for each

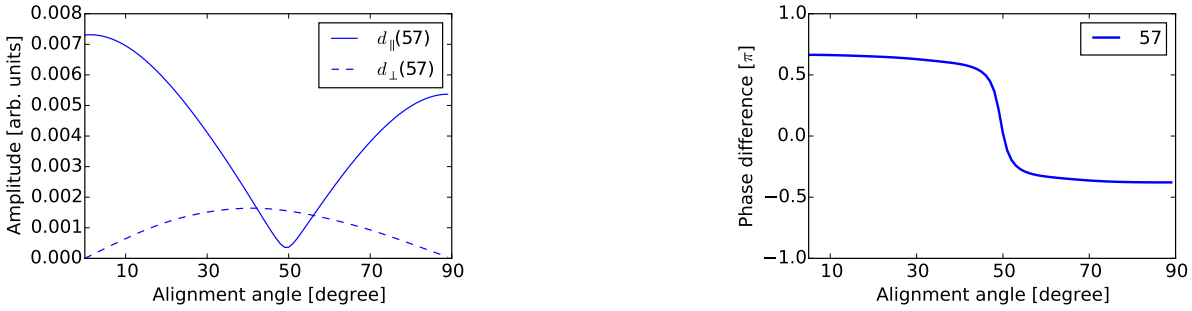

Figure 3.23: The amplitudes of parallel and perpendicular components (left) and phase difference δ (right) of 57^{th} harmonic order of H_2^+ as a function of the alignment angle in a laser field at wavelength of 800 nm and intensity 3×10^{14} W/cm^2.

harmonic the amplitude ratio is close to 1 and the phase difference also changes dramatically near the interference minimum.

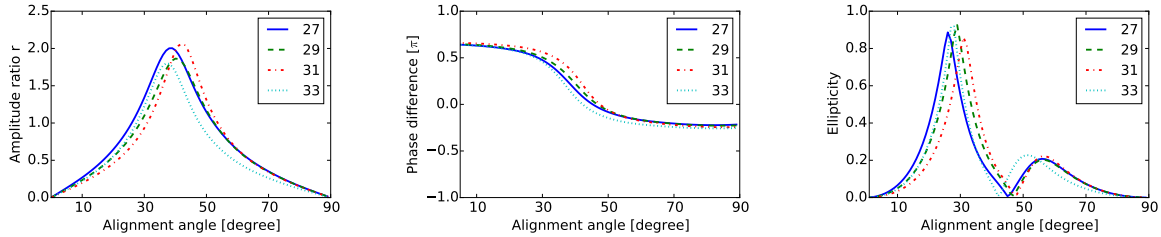

Figure 3.24: The amplitude ratio r (left), phase difference δ (middle), and the ellipticity (right) of high-order harmonics from H_2^+ in a laser field at wavelength of 800 nm and intensity 3×10^{14} W/cm^2.

3.4.2 Complex ellipticity pattern due to two-electron effects

We have shown that the maximum ellipticity of harmonics for a simple one-electron system arises around the interference minimum for H_2^+. We will now consider the influence of two-electron effects in H_2. Considering that the two electrons are in the ground state $1\sigma_g$, we do not expect too much difference for the amplitude and phase difference pattern. We have performed a simulation for H_2 with the same laser parameters as for H_2^+. The results in Fig. 3.25 do share some similar pattern for the amplitude ratio: maximum amplitude ratio and phase change around the interference position which appears at the angle of 40^o. However, the ratio here is not as smooth as that for

H_2^+. Concerning the ellipticity, while the results for H_2^+ show clearly a strong ellipticity around the interference minimum, the ellipticity pattern for H_2 is more complex although the ellipticity maximum is still located near the position of interference minimum.

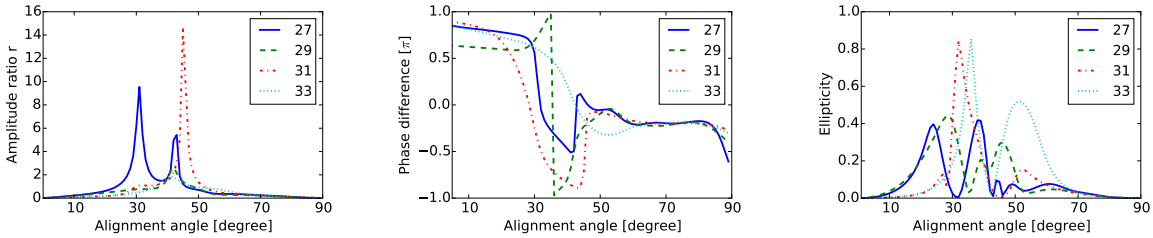

Figure 3.25: The same as Figure 3.24 but for H_2.

Such comparison of the results for these simplest molecules indicates that the ellipticity can be strongly influenced by multielectron effects. In case of the two-electron molecule, the ellipticity pattern is already considerably more complex than that for the one-electron molecule. For molecules with more than two electrons, we therefore expect even more complicated features since effects like interference from orbitals with different symmetry and coupling between the orbitals may occur.

3.4.3 Alignment angle average

In the following sections, we are going to compare our simulation results with experimental data. In experiment, molecules are often aligned using a laser pulse which initiates a rotational wavepacket. The molecules in the ensemble are then aligned at certain time according to the rotational period. The alignment in the experiment is however usually not perfect. The distribution of alignment is measured via $\langle \cos^2 \theta \rangle$. We account for this distribution by carrying out simulations for the angles in the distribution in order to do angle average and compare with observations in experiments.

To obtain the ellipticity at different alignment angle, the time-dependent Kohn-Sham equation

$$i\frac{\partial}{\partial t}\phi_k(\mathbf{r},t) = -\nabla^2\phi_k(\mathbf{r},t) + \left(V_{KS}[\rho(\mathbf{r},t)] + U(\mathbf{r},t)\right)\phi_k(\mathbf{r},t) \tag{3.42}$$

is solved for each alignment angle. The parallel and perpendicular components of dipole moment $d_{\parallel}(\theta,t))$ and $d_{\perp}(\theta,t)$ are obtained via Eq. (3.28). To take account of the distribution of alignment angles in molecular ensemble in the experiment, it is then straightforward to average the dipole moments using the reported alignment distributions [166, 164].

Let the probe laser electric field be along the z-direction (x=0,y=0,z=1) as shown in the diagram in Fig. 3.26 and the pump laser field lies in the y-z plane with a polar angle α and thus the electric field direction for the pump laser field is (0, $\sin\alpha$, $\cos\alpha$). After applying the pump laser field, the linear diatomic molecule is oriented in the direction ($\sin\theta_m\cos\phi_m$, $\sin\theta_m\sin\phi_m$, $\cos\theta_m$). The intersection angle between the pump laser field and the molecular axis is denoted as θ. Then the orientation distribution of molecules with respect to the pump laser field is only a function of θ, denoted as $\rho(\theta)$. The angle θ can be obtained via

$$\cos\theta = \sin\alpha\sin\theta_m\sin\phi_m + \cos\alpha\cos\theta_m. \tag{3.43}$$

Thus the alignment distribution for the molecular axis at orientation angle (θ_m,ϕ_m) with respect to the pump probe angle α is

$$\rho(\alpha,\theta_m,\phi_m) = \rho(\theta(\alpha,\theta_m,\phi_m)), \tag{3.44}$$

and the harmonic spectrum after angle average is given by

$$\bar{d}_{\perp/\parallel}(t,\alpha) \;=\; \int_0^{\pi}\int_0^{2\pi} d_{\perp/\parallel}(t,\theta_m,\phi_m)\rho(\alpha,\theta_m,\phi_m)\sin\theta_m d\theta_m d\phi_m. \tag{3.45}$$

For the calculation of $d_{\perp/\parallel}(t,\theta_m,\phi_m)$, in case of a diatomic molecule, we only perform simulations for several polar angles θ_m at $\phi_m = 0$. For other non-zero ϕ_m, the component $d_{\perp/\parallel}(t,\theta_m,\phi_m)$ can be obtained via a transformation of the calculation results at $\phi_m = 0$.

3.4.4 Comparison with experimental data for N_2

Measurements of the polarization and ellipticity of high-order harmonics generated in nitrogen molecules have been reported recently. Zhou et al. [164] carried out an experiment on molecule N_2 to study the ellipticity of the generated harmonics, in which a 30 fs probe pulse at intensity of

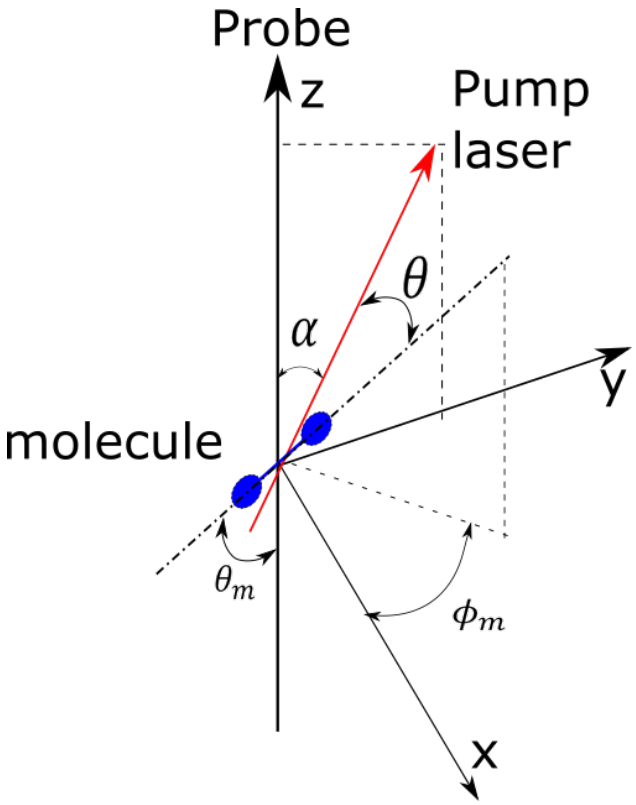

Figure 3.26: Illustration diagram for angle average procedure.

2×10^{14} W/cm^2 was focused on the molecule N_2 which was aligned by a pump pulse. The ellipticity dependence as a function of the pump-probe angle was studied by varying the time delay between pump and probe pulse. In the experiment, the alignment parameter $\langle\cos^2\theta\rangle$ was measured to be 0.65, as compared to 0.3 for random alignment. The measured ellipticity, shown in Fig. 3.27(c), is very large as compared to that observed in a previous experiment [167].

To explain the experimental observations, we have performed simulations with similar laser parameters and the results are angle averaged using the measured distribution. We compared results for different intensities and achieved a good agreement with experiment, which was performed at a relatively low intensity 1×10^{14} W/cm^2. In fact, it is difficult to measure the intensity at the focal spot accurately. Therefore, it is not surprising that results from theory and experiments agree at different laser intensities. We attribute the sensitivity of the ellipticity as a function of intensity to the multielectron character within the present theoretical method. It has been shown by Son et al. [150], and confirmed by us in test calculations, that for one and two-electron molecules the ellipticity varies more smoothly.

Fig. 3.27 compares our simulation results with angle average (middle) and without (left) as well as experimental results (right). The angle averaged results are in good agreement with the experimental observations showing a maximum ellipticity of about 0.4 for alignment angles around 40^o-60^o. As far as we know, this is the first time an agreement between results from ab-initio calculations with experimental data for ellipticity has been found. In the following subsection we will further analyze the contributions from different orbitals.

We note that the ellipticity value is pretty large before angle average. For example, for an alignment at 40^o, the ellipticity of the 19^{th} harmonic is close to 0.8, while after angle average, the maximum ellipticity is only 0.45 for the 21^{th} harmonics. On the other hand, the ellipticity structure is smoother and has similar trend for different harmonics after the average, which means lots of detailed information get lost. Since obtaining and manipulating the ellipticity of HHG is an important goal, our simulations suggest that improving the alignment technique is one way to get highly elliptically polarized harmonics. Furthermore, an improved alignment technique would make

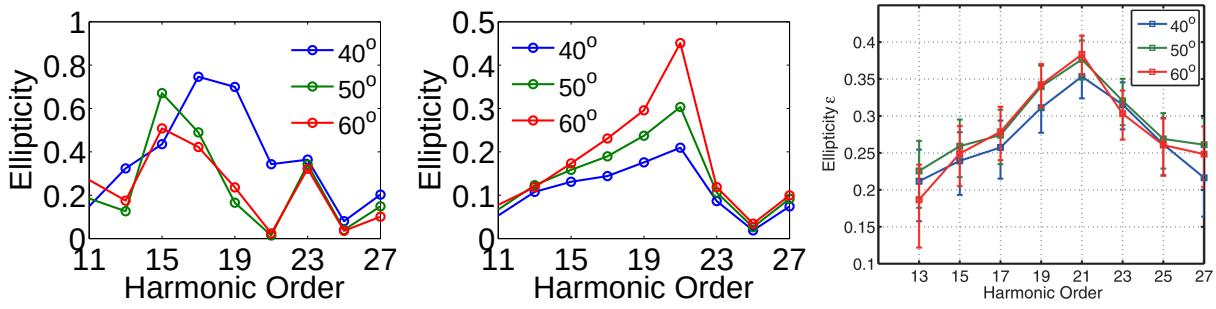

Figure 3.27: Ellipticity of high-order harmonics as a function of the harmonic orders for three molecular alignment angles at $\lambda = 800$ nm and peak intensity of $I_o = 1 \times 10^{14}$ W/cm^2. Comparison of results in which no average (left panel) and a proper average (middle panel) over the distribution of the alignment in the molecular ensemble has been taken into account and experimental results (at 2×10^{14} W/cm^2)(right), adapted from [164].

it possible to access the rich information in the ellipticity, which might provide another approach to study electronic structure in molecules.

Another experiment on ellipticity in HHG from N_2 is reported by Mairesse et al. [154], as shown in Fig. 3.28. Our TDDFT simulation results with and without angle average are presented in Fig. 3.29. Again, we see that TDDFT simulation are in excellent agreement with the experimental data. In this case, intensity 7.5×10^{13} W/cm^2 used in our simulation is just slightly lower than the reported experimental intensity of 8×10^{13} W/cm^2. Mairesse et al. [154] analyzed harmonic

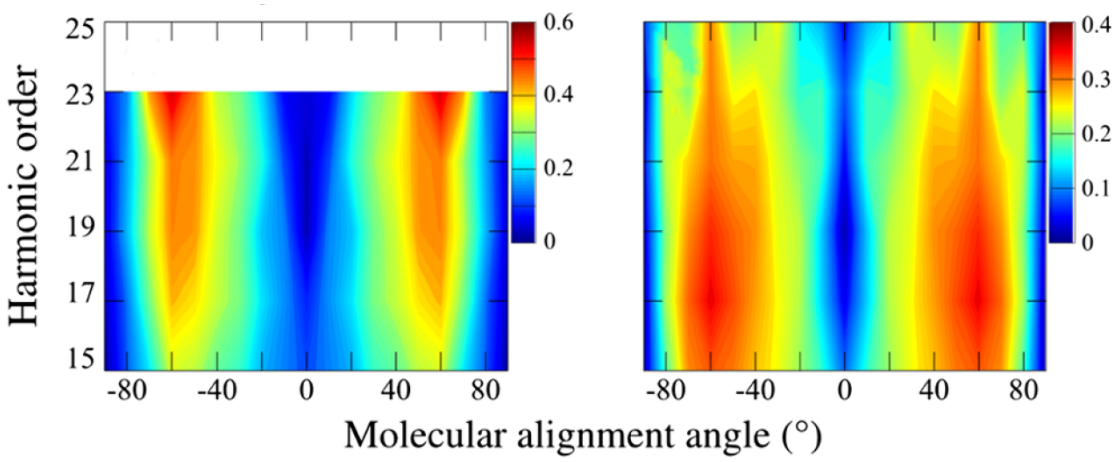

Figure 3.28: Ellipticity from N_2 with 800 nm laser field at intensity of 8×10^{13} W/cm^2 (left) and 1×10^{14} W/cm^2 (right), adapted from [154].

generation from different HHG channels due to the dynamics in the ion. As shown in Fig. 3.30, they considered the situation when an electron, liberated from HOMO, returns to the parent ion, and may find the hole in HOMO-1 orbital, which is created by the resonant coupling of HOMO and HOMO-1 by the 800 nm laser field for large alignment angle between molecular axis and probe laser. In their calculations, ionic ground state X (hole in HOMO), A (hole in HOMO-1), and B (a hole in HOMO-2) are considered. In the paper, the authors studied the relative phase between ionization from HOMO and HOMO-1 and showed that a π phase difference is necessary to reproduce the experimental results. While in the paper the laser-induced subcyle coupling between ionic states is modeled explicitly and decoupled from the HHG process, it is interesting to study such effects with TDDFT which capture the full multielectron dynamics. In the following subsection, we are going

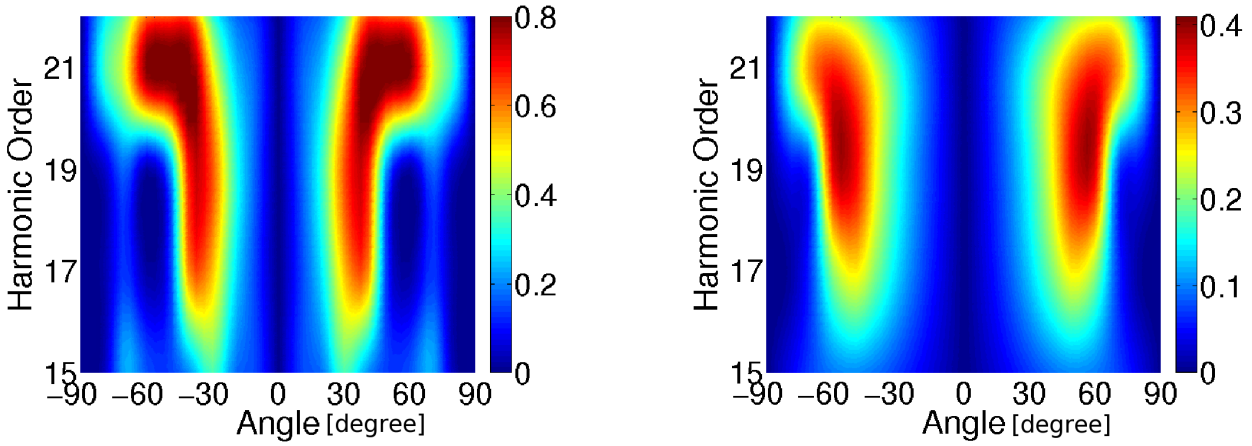

Figure 3.29: Ellipticity of high-order harmonics as a function of the molecular alignment angle and the order of the harmonics at $\lambda = 800$ nm and peak intensity $I_0 = 7.5 \times 10^{13}$ W/cm^2. Comparison of results in which no average (left panel) and a proper average (right panel) over the distribution of the alignment in the molecular ensemble is made.

to present our simulation results which reveal the contribution from each valence shell orbital and their influence on the ellipticity of HHG.

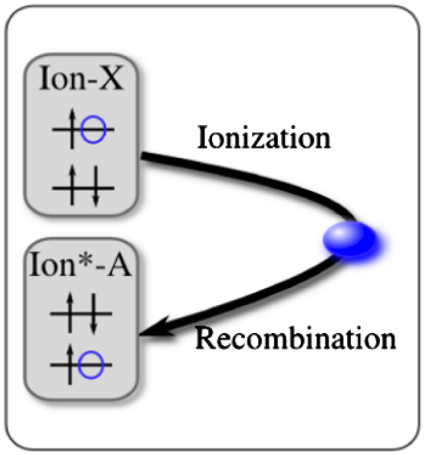

Figure 3.30: Mechanism studied in [154]. Electron is ionized from HOMO and recombines to HOMO-1. The hole at HOMO-1 is created by the 800 nm laser pulse which resonantly couples HOMO-1 and HOMO. Figure is adapted from [154].

3.4.5 Inner shell contributions to ellipticity of harmonics

In our full TDDFT calculations the response of all electrons in the nitrogen molecule is considered. Due to the ab-initio character of TDDFT calculations and in contrast to other theoretical approaches, as e.g. the strong-field approximation used in [154], the recombination and ionization events cannot be separated in the analysis and the laser driven dynamics is not restricted to part of the pulse. In order to analyze the role of transitions to individual orbitals we have further calculated also the responses from a subset of occupied orbitals in the molecule. In Fig. 3.31 we compare the results of such calculations with those of the full calculations for the same laser parameters as in Fig. 3.27. In each panel the ellipticity of the harmonics is plotted as function of the harmonic order and the molecular alignment angle. In order to illustrate the importance of the inner-valence orbitals no ensemble average of the molecular alignment was performed in this set of calculations.

The role of inner-shell contributions becomes obvious from the comparison of the results of the full calculation (upper left panel) and those obtained from the HOMO orbital only (lower left

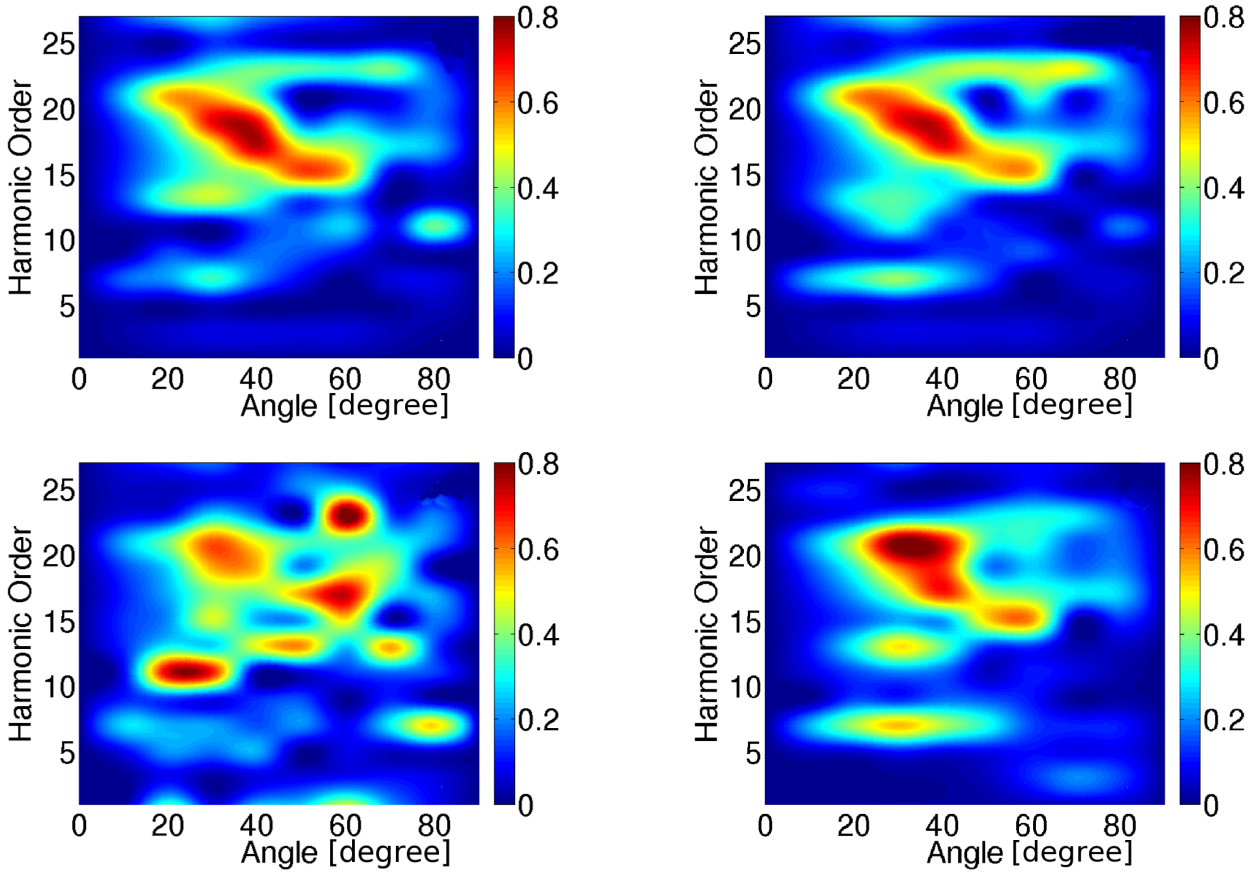

Figure 3.31: Ellipticity of harmonics as function of harmonic order (vertical axis) and angle between molecular axis and laser polarization direction (horizontal axis). Comparison of results from the full calculation (upper left panel) and contributions from HOMO, HOMO-1 and HOMO-2 (upper right panel), HOMO and HOMO-1 (lower right panel) and HOMO only (lower left panel). Laser parameters: wavelength of 800 nm, peak intensity of 1×10^{14} W/cm^2 and pulse duration of 20 fs.

panel). Neither for the low-order nor for the high-order harmonics the HOMO contribution agrees well with the full results. A significant improvement is achieved when both contributions from the HOMO and the HOMO-1 are included in the calculations (lower right panel). However, certain features in the results of this partial calculation, such as the strong maximum for the 21st harmonic at an orientation angle of about 30^o, are not present in the full calculation. Further inclusion of the contributions from the HOMO-2 orbital (upper right panel) finally leads to a more satisfactory agreement with the full results. Therefore, we may point out that we observe a strong influence of multielectron effects and contributions from, at least, three orbitals in the nitrogen molecule over the whole HHG spectrum. This applies, in particular, also for the low-order harmonics which could not be investigated in the previous theoretical studies based on strong- field approximation.

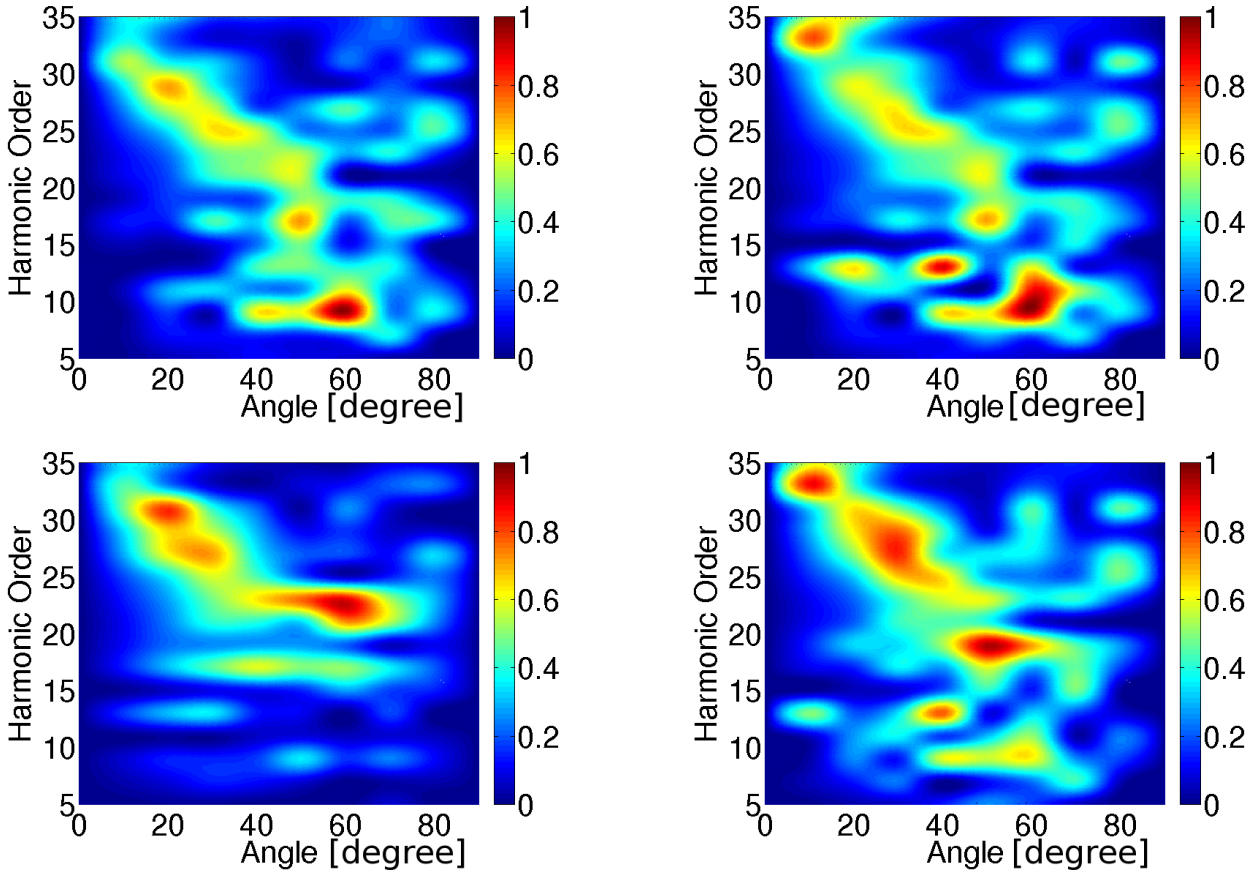

Figure 3.32: Same as Fig. 3.31 but for a laser wavelength of 1000 nm.

In our calculations we have further noticed that a certain inner-shell channel becomes particularly important at driving laser wavelengths, for which there is a resonance between the inner-shell orbital and the HOMO. This can be seen from the results presented in Fig. 3.32 which were obtained for a laser wavelength of 1000 nm. At this wavelength the (unperturbed) HOMO and HOMO-2 levels in the neutral nitrogen molecule are coupled via a two-photon resonance transition. The results show that the effect of the HOMO-2 contributions on the ellipticity of the harmonics is even stronger than at 800 nm (Figure 3.31).

3.4.6 Ellipticity of harmonics from CO_2

3.4.6.1 Comparison with experimental data for CO_2

We have also investigated ellipticity of HHG from CO_2, another extensively studied molecule. Similarly, we have done a simulation for CO_2 with 800 nm laser field at intensity of 1.5×10^{14} W/cm^2 with orientation angle from 0^o to 90^o at a step of 10^o. To compare with experimental results [164], angle average is applied as well. The harmonic intensity ratio of perpendicular to parallel components is calculated and presented in Fig. 3.33(b). The intensity ratio for harmonic order from 17^{th} to 23^{rd} is in the range from 0.02-0.07 which agrees with experimental data in Fig. 3.33(a). The orientation angle ϕ of the elliptically polarized high harmonics, illustrated in Fig. 3.34(a), is

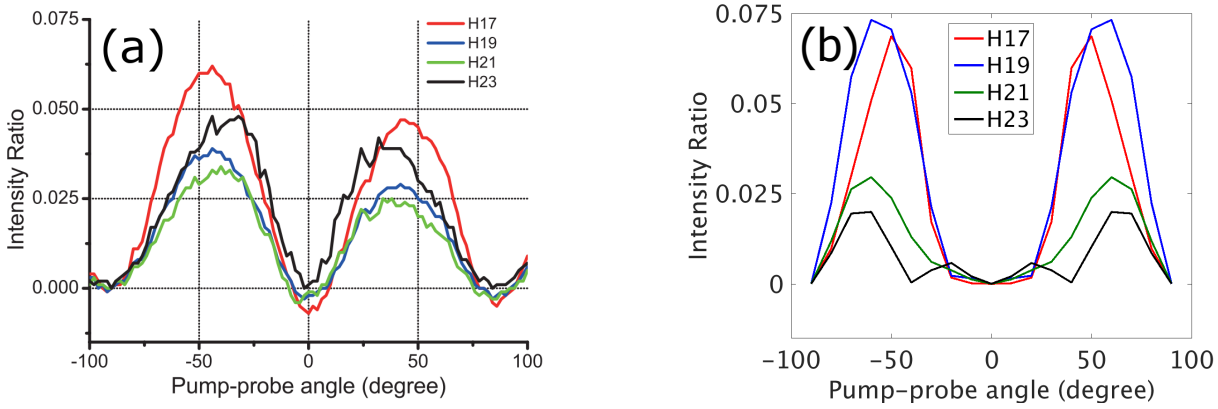

Figure 3.33: Intensity ratio of perpendicular to parallel component. Comparison between experimental result (a) adapted from [164], and our simulation result (b).

also calculated and shown in Fig. 3.34(c). The orientation angle is in opposite direction to the probe-pump angle and has a minimum at 23^{rd} harmonic order. Such features are in agreement with data of experimental measurements shown in Fig. 3.34(b). Experimentally observed ellipticity from

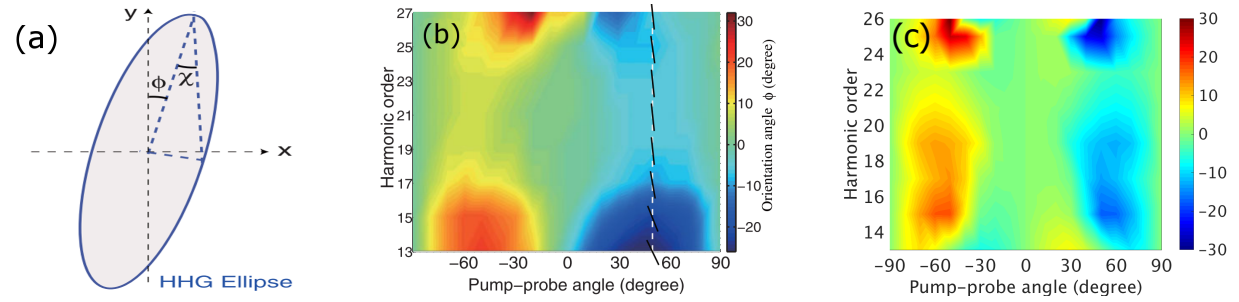

Figure 3.34: Illustration of high harmonic ellipticity orientation angle (a), experimental results of ellipticity orientation angle from CO_2 (b), adapted from [164], and our simulation results (c).

CO_2 is relatively small [164]. We also obtained the ellipticity with ensemble angle averaged results, shown in Fig. 3.35. The ellipticity is weak except for some strong ellipticity around the cutoff. Such weak ellipticity is partly due to the ensemble angle average effect as we have seen for N_2. Another reason is the role of multiorbital contributions, as we will discuss in the next subsection.

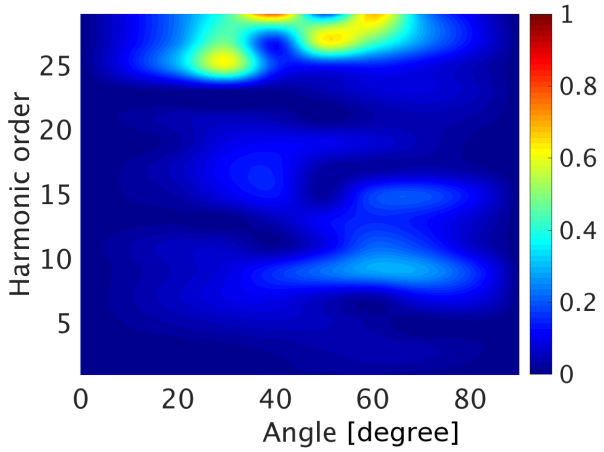

Figure 3.35: Ellipticity of high harmonics as function of alignment angle for CO_2 for a laser field at $\lambda = 800$ nm and $I = 1.5 \times 10^{14}$ W/cm^2.

3.4.6.2 Inner valence shell orbital contributions to ellipticity of harmonics

We study the contribution from each inner valence by looking at the response from HOMO as well as adding those from deeper orbitals. The results are shown in Fig. 3.36. No angle average is performed here. The ellipticity of high harmonics from CO_2 is influenced nearly by all the valence shell orbitals. The ellipticity of HHG from the HOMO ($1\pi_g$) is strong as shown in Fig. 3.36(a) and we also find that based on the two-point interference model, the strong ellipticity happens around the position of destructive interference. However, after adding contribution from HOMO-1 to HOMO, the ellipticity becomes weaker, as presented in Fig. 3.36(b). As we add contributions from inner orbitals one by one, the ellipticity is gradually getting smaller. Therefore, in this case the multiorbital contributions gradually lead to a weak ellipticity while for N_2 we did not observe similar effect.

The reason for the strong contribution from inner valence orbitals is that HHG depends on the ionization which is influenced not only by the ionization potential but also the alignment angle. Although the HOMO has relatively small ionization potential and thus is easier to ionize, its ionization rate is suppressed at 0^o and 90^o because of quantum destructive interference, and has a maximum ionization rate at 45^o. The HOMO-1 and HOMO-2 have very similar ionization potential but the HOMO-1, which is σ_u orbital, is easier to ionize at 0^o while the HOMO-2, which is π_u orbital, is easier to ionize at 90^o (ionization dependence on symmetry will be discussed in next Chapter in detail). So, the HOMO-1 and HOMO-2 have strong contributions to the HHG at angle close to 0^o and 90^o, respectively. As for the HOMO-3 (σ_g), the contributions to HHG comes from the strong coupling between HOMO-3 and HOMO-1 at 800 nm close to 0^o. Looking at the projection between these two orbitals in the laser field, shown in Fig. 3.37(a), there is a significant coupling between these two orbitals (even at off resonant frequency), which means that HOMO-3 plays a role as important as HOMO-1 and thus influences the ellipticity strongly. Finally, HOMO-4 and HOMO-5 contribute to ellipticity slightly. At 800 nm, the two orbitals are however coupled significantly and there is 40% population transfer between these two orbitals, as seen from the right

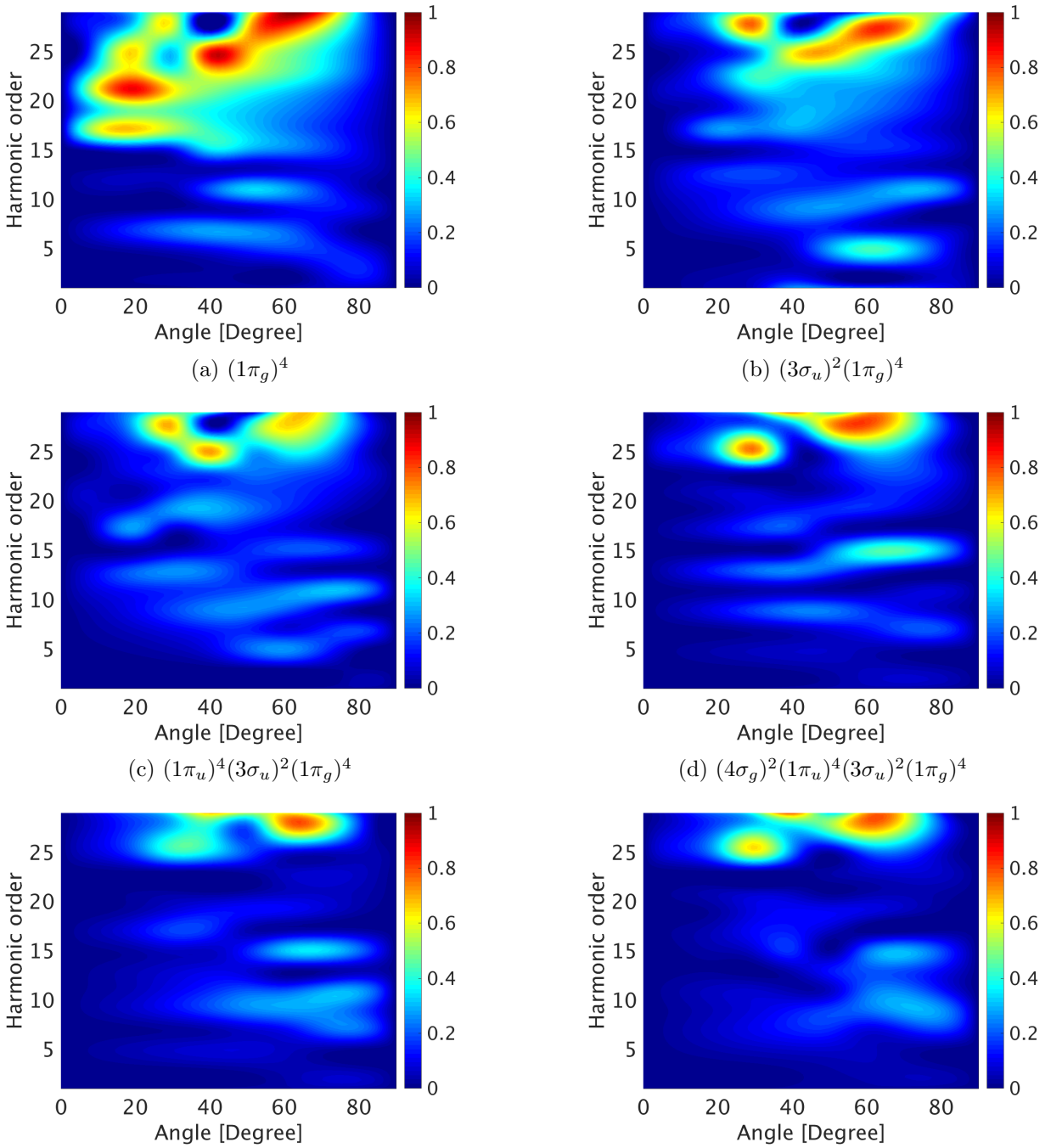

(a) $(1\pi_g)^4$

(b) $(3\sigma_u)^2(1\pi_g)^4$

(c) $(1\pi_u)^4(3\sigma_u)^2(1\pi_g)^4$

(d) $(4\sigma_g)^2(1\pi_u)^4(3\sigma_u)^2(1\pi_g)^4$

(e) $(2\sigma_u)^2(4\sigma_g)^2(1\pi_u)^4(3\sigma_u)^2(1\pi_g)^4$

(f) $(3\sigma_g)^2(2\sigma_u)^2(4\sigma_g)^2(1\pi_u)^4(3\sigma_u)^2(1\pi_g)^4$

Figure 3.36: Ellipticity of harmonics as a function of alignment angle for CO_2. Starting with the results from HOMO only (upper left), contributions from inner valence orbitals are added step by step in the other panels (as indicated). A proper average over the distribution of the alignment in the molecular ensemble is made. Applied laser field is at wavelength of 800 nm and intensity of 1.5×10^{14} W/cm^2 with 30 fs pulse length.

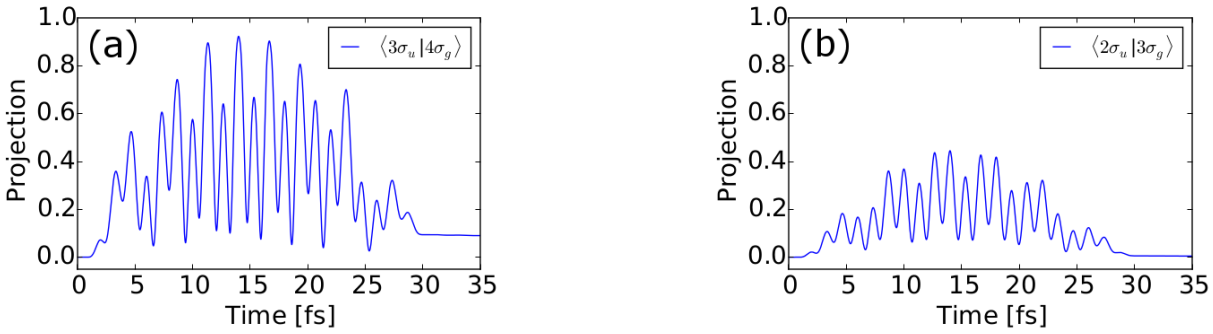

Figure 3.37: Projection of coupled inner valence orbitals HOMO-3 ($4\sigma_g$) to HOMO-1 ($3\sigma_u$) (a) and HOMO-5 ($3\sigma_g$) to HOMO-4 ($2\sigma_u$) (b). Laser wavelength of 800 nm and intensity of 2×10^{14} W/cm^2 with orientation angle of 20^o are considered.

panel in Fig. 3.31. Based on our simulations, we can therefore conclude that the dynamics from and between different orbitals during the HHG in CO_2 is even more complex as compared to N_2.

3.5 Summary

In this Chapter, we first have shown that fractional harmonics in the form of Mollow sidebands occur in high-order harmonic spectra of open shell molecules at equilibrium geometries. The fractional harmonics appear due to a one-photon coupling (Rabi flopping) between one of the inner valence orbitals and the outer open shell induced by the driving laser. The phenomenon is found and illustrated for parallel as well as perpendicular transitions, di-, tri- and polyatomic molecules, coupling of different type of orbitals, and different orientations of the molecule. Thus, it is shown that Mollow sidebands are much more general than the previously studied case of stretched H_2^+ in the regime of charge resonance enhanced ionization. Moreover, the time-dependent electron density and the time-frequency analysis have shown that the appearance of fractional harmonics comes along with a nonadiabatic electron dynamics and localization in the molecule as well as a breakdown of the traditional semiclassical picture of high-order harmonic generation.

We also analyzed the ellipticity of high harmonic spectra starting from simple one-electron molecule H_2^+ to multielectron molecules N_2 and CO_2. The results obtained within the time-dependent density-functional theory reveal the importance of multielectron contributions from

different orbitals for the interpretation of recent experimental data for the ellipticity of higher-order harmonics. It is shown that the full multielectron results are in excellent agreement with the experimental data, if contributions from inner valence orbitals over the whole HHG spectrum are taken into account. We have further confirmed that it is essential to take proper account of the distribution of the molecular axis with respect to the polarization direction to find agreement with the observations.

Chapter 4

Multielectron effects in strong-field ionization from molecules

The ionization of atoms and molecules is another fundamental strong-field process. It provides information about the system from which electron is ionized. For example, streaking and RABBITT are experimental techniques in which measurement of ionized electrons are used to gain dynamical information through pump-probe experiments [168, 169].

Compared to atoms, for molecules the quasistatic picture of tunneling ionization needs to be modified to incorporate the multi-center nature of atomic potentials in molecules. There are indeed several fundamental differences between the ionization of atoms and molecules. Earlier studies [170, 171, 172] revealed experimentally that the ionization signal of molecules and noble gas atoms with comparable ionization potentials behave similarly, for example, the ionization yields of the pair N_2 and Ar as a function of intensity are similar. Later it was found that O_2, which has a similar ionization energy as Xe, violates such rule because of the destructive interference in the electron emission from anti-bonding π_g (HOMO) orbital in O_2 [30]. Therefore, the ionization of molecules is more complex than ionization of atoms, but contains also more information about the electronic structure. Another fundamental difference is charge-resonance-enhanced ionization (CREI) discovered for H_2^+, which occurs at a critical internuclear distance R_c, greater than equilibrium distance R_e [173, 174].

One common approximation in theory of strong-field ionization is to assume that only one active electron responds to the external laser field, which is called, as mentioned before, single-active-electron (SAE) approximation. Recent experimental results on ionization and dissociation

of Br_2 show however that during the dissociation process the valence orbitals rearrange. Ionization from π_u orbital is observed at early dissociation stage, while ionization from σ_g orbital as well as other valence orbitals is observed at large internuclear distances [175]. Such phenomena, orbital rearrangement during dissociation process and changes in the ionization yields from orbitals, are also observed in simulations for stretched C_2H_2 [176]. TDDFT simulations show that inner valence orbitals can contribute considerably to total ionization at high intensity [63, 177]. Furthermore, in experiments on filamentation in N_2 and CO_2 [178, 179], it is found that there is an unusual high ionization yield from the inner valence orbitals compared to the ionization of HOMO, which leads to a population inversion in the ion. Thus, we need to understand the multielectron effects in ionization process. However, the theoretical treatment remains difficult due to the complexity of direct simulation for multielectron systems performed by solving multielectron Schrödinger equation. So by now, there are still not many theoretical studies on multielectron effects in strong-field ionization.

In this Chapter, we are going to investigate the ionization of molecules using TDDFT simulations. This gives us the opportunity to analyze the response from each Kohn-Sham orbital of a multielectron molecule in view of the role of the orbital symmetry and the dependence on the laser field parameters. Specifically, we will study the influence of resonant coupling between valence orbitals on the strong-field ionization.

4.1 Role of ionization potential and orbital symmetry

Within TDDFT approach the Kohn-Sham orbitals are propagated in the laser field. Thus, the population of the i^{th} orbital can be obtained by integrating the corresponding wavefunction in the simulation box

$$n_i^{ks}(t) = \int_{box} |\phi_i(\mathbf{r}, t)|^2 d\mathbf{r}, \tag{4.1}$$

where ϕ_i is the wavefunction of the i^{th} Kohn-Sham (KS) orbital. We also denote the dynamical population $n_i^{ks}(t)$ of i^{th} KS orbital explicitly with superscript ks, which is necessary to separate

it from state population in resonant case as we will show later. The corresponding ionization probability of ith KS orbital is equal to

$$P_i^{ks}(t) \quad = \quad 1 - n_i^{ks}(t). \tag{4.2}$$

The ionization yield from different orbitals can strongly depend on orbital symmetry and ionization potential. Ionization from inner valence orbitals is usually at least an order of magnitude smaller than ionization from HOMO, because of the larger ionization potential as confirmed by our simulation results in Fig. 4.1. In the simulations, a 600 nm laser field at intensity 5×10^{13} W/cm^2 is applied to N_2 with polarization parallel (left) and perpendicular (right) to the molecular axis. In

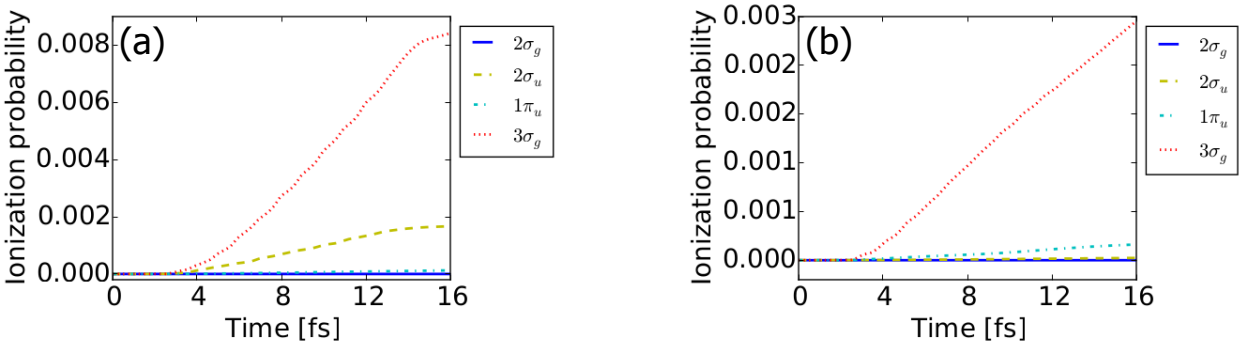

Figure 4.1: Ionization from KS orbitals of N_2 for parallel (a) and perpendicular (b) alignment with respect to external laser field polarization. The laser field parameters: wavelength of 600 nm and intensity of 5×10^{13} W/cm^2.

both cases, the HOMO ($3\sigma_g$) is the strongest ionized orbital as one would expect due to its lowest ionization potential. The ionizations from other orbitals are negligible in this case. However, we can still see that the second strongest ionized orbital is different for the two cases: it is HOMO-2 ($2\sigma_u$) for parallel orientation while for the perpendicular alignment it is HOMO-1 ($1\pi_u$). Although HOMO-1 has slightly lower ionization potential compared to HOMO-2, its ionization is much smaller than HOMO-2 in parallel case. This is because the ionization not only depends on the ionization potential but also strongly on the orbital symmetry and molecular orientation. The symmetry of HOMO-1 influences its ionization in two aspects. HOMO-1 is a π_u orbital (see Fig. 3.4) and it possesses a nodal plane along the molecular axis. If the polarization of laser field is

parallel to the molecular axis, the ionized wavepackets from parts of the orbital above and below the nodal plane interfere destructively with each other due to the opposite phase and thus suppress the ionization, while this is not the case for perpendicular alignment. The ionization of HOMO-2 (σ_u orbital) is also influenced in this way but destructive interference occurs in the perpendicular case. The second effect comes from the density distribution, namely, how much it is extended from the center. The σ orbitals are more extended along molecular axis, while π-orbitals are more extended in perpendicular direction. Because of these factors, HOMO-2 is easier to ionize for parallel molecular orientation, while the HOMO-1 is easier to ionize for perpendicular alignment. We can also see such effects by looking at the ionization from HOMO. In Fig. 4.1, the two figures are generated for the same parameters except the orientation angle. The ionization probability of HOMO in parallel case is obviously larger than that for perpendicular orientation.

4.2 Resonance enhanced ionization of open-shell molecules

We have previously studied the resonance induced fractional harmonics in open-shell molecules. We have shown that for N_2^+ with one spin-up electron removed from HOMO, the resonant laser field at wavelength of 400 nm strongly couples HOMO-2 and HOMO and can enhance the ionization from HOMO-2 strongly, shown in Fig. 3.13(d). For other open-shell molecules, in the same coupling regime where we have seen fractional harmonics, we can also observe the enhanced ionization. The results are shown in Fig. 4.2. For NO_2 in Fig. 4.2(a) where the HOMO ($|6a_1\uparrow\rangle$) is not occupied, the 400 nm laser field induces a coupling between HOMO-1 ($|4b_2\uparrow\rangle$) and HOMO ($|6a_1\uparrow\rangle$) and thus $|4b_2\uparrow\rangle$ has the relative strongest ionization compared to that of other orbitals. For CO_2^+ in Fig. 4.2(b), where an electron in $|1\pi_g\uparrow\rangle$ is removed, a 350 nm laser field induces a coupling between HOMO and HOMO-1 in parallel direction to the molecular axis. The ionization of valence orbitals are more complex. There are three different types of orbitals strongly involved in the ionization process. For the spin-down components, the ionization behavior is like what we expect based on the ionization potentials and symmetries of valence orbitals. The HOMO-1 ($|3\sigma_u\downarrow\rangle$) is strongly ionized at parallel orientation compared to the other two types of orbitals: HOMO ($|1\pi_g\downarrow\rangle$) and

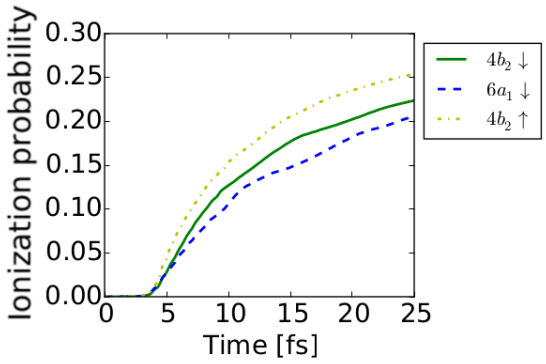

(a) NO_2 with $|6a_1\uparrow\rangle$ unoccupied. λ=400 nm, $I = 2\times10^{14}$ W/cm^2, $|4b_2\uparrow\rangle$ and $|6a_1\uparrow\rangle$ are coupled.

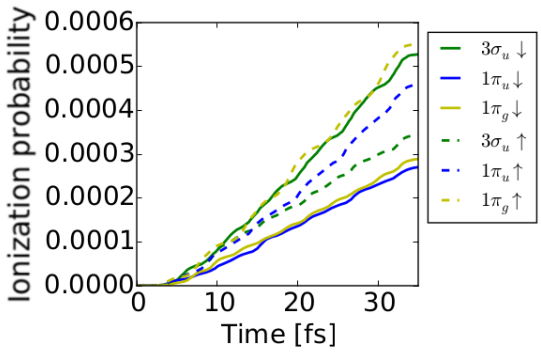

(b) CO_2^+ with $|1\pi_g\uparrow\rangle$ partially occupied. Laser parameters: λ=350 nm, $I = 1\times10^{14}$ W/cm^2. $|1\pi_u\uparrow\rangle$ and $|1\pi_g\uparrow\rangle$ are coupled. For the π_g and π_u orbital, ionization is normalized by initial number of electrons.

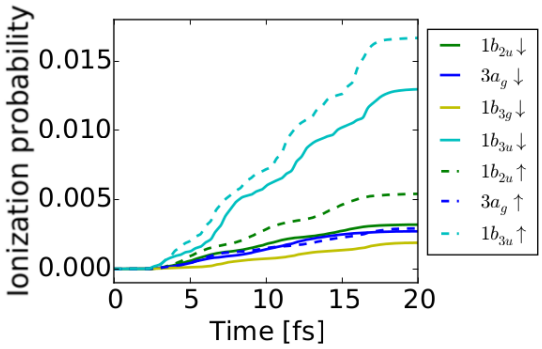

(c) $C_2H_4^+$ with $|1b_{3g}\uparrow\rangle$ unoccupied. Laser parameters: $\lambda = 400$ nm and $I = 1\times10^{14}$ W/cm^2. $|1b_{3g}\uparrow\rangle$ and $|1b_{2u}\uparrow\rangle$ are coupled.

Figure 4.2: Ionization of KS orbitals of openshell molecules: NO_2 (a), CO_2^+ (b), and $C_2H_4^+$ (c). The laser parameters and coupling orbitals are illustrated in the captions below each figure.

HOMO-2 ($|1\pi_u \downarrow\rangle$). For the spin-up component, the HOMO ($|1\pi_g \uparrow\rangle$) is only partially occupied, the coupling between HOMO-2 ($|1\pi_u \uparrow\rangle$) and HOMO ($|1\pi_g \uparrow\rangle$) leads to a strong ionization of HOMO-2 ($|1\pi_u \uparrow\rangle$). For $C_2H_4^+$ in Fig. 4.2(c), where HOMO-1 ($|1b_{3g} \uparrow\rangle$) is unoccupied, the ionization from HOMO ($|1b_{3u}\rangle$) is still the strongest ionized orbital due to its lowest ionization potential. A 400 nm laser field induces a coupling between HOMO-1 ($|1b_{3g} \uparrow\rangle$) and HOMO-3 ($|1b_{2u} \uparrow\rangle$), which enhances the ionization of HOMO-3 ($|1b_{2u} \uparrow\rangle$). But its ionization yield is still relatively smaller than that of HOMO.

Such resonance enhanced multiphoton ionization (REMPI) is a very important process for molecules and it is often used in experiments as a spectroscopy tool for mass spectrometry [180]. Besides REMPI set up for open-shell molecules, we are also interested in studying enhanced ionization from inner-shell orbitals for closed-shell molecules. In the next section we therefore present results for ionization of N_2 at equilibrium internuclear distance.

4.3 Multiorbital contributions and enhanced ionization from inner-shell orbitals of N_2

In section 4.1, we have seen a typical case in which the ionization probability of N_2 is dominantly determined by the orbital with the lowest ionization potential. In such case, it is reasonable to assume that only one active electron or one orbital responds to the external field. However, we have seen before for HHG that the resonant coupling between orbitals can lead to new effects. In particular, we will now analyze if there is any effect on ionization when the laser frequency is tuned to the energy difference for two occupied orbitals in neutral molecules.

The energy differences between HOMO-2 and HOMO, HOMO-1 and HOMO of N_2 correspond to wavelengths of about 400 nm and 800 nm, respectively. These are typical laser wavelengths used in experiments nowadays. We have carried out simulations at these wavelengths and studied the ionization of N_2 with 400 nm laser field with polarization parallel to molecular axis and 800 nm laser field with polarization perpendicular to the molecular axis. The time-dependent ionizations of valence KS orbitals are presented in Fig. 4.3. Compared to the case with 600 nm laser field

shown in Fig. 4.1, we notice a significantly enhanced ionization from inner orbital HOMO-2 ($2\sigma_u$) for parallel orientation and HOMO-1 ($1\pi_u$) for perpendicular alignment.

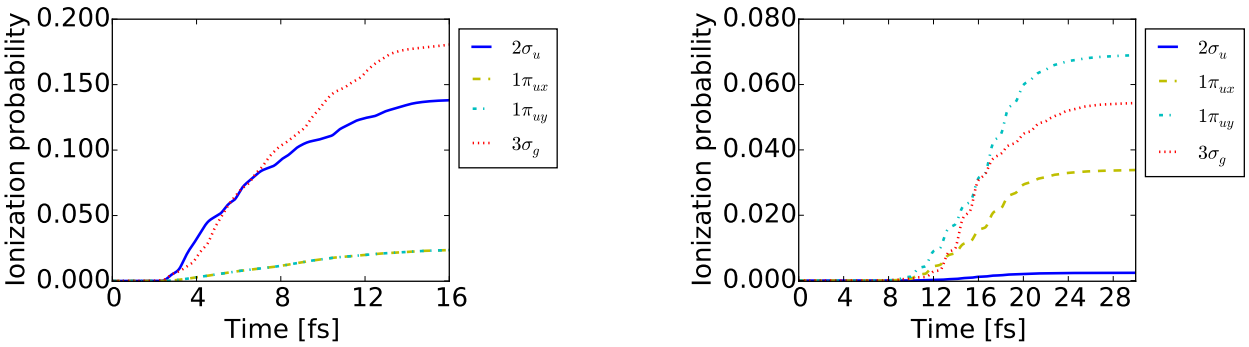

Figure 4.3: The ionization probability of valence KS orbitals of N_2. Only the relevant KS orbitals which possess an important response to the laser field are shown with their labels. Left: Laser polarization is parallel to the molecular axis at 400 nm and intensity of 2×10^{14} W/cm^2, inducing a coupling of HOMO ($3\sigma_g$) and HOMO-2 ($2\sigma_u$). The curves for $1\pi_{ux}$ and $1\pi_{uy}$ overlap because they are degenerate. Right: Laser polarization is perpendicular to the molecular axis at wavelength of 800 nm and intensity of 2×10^{14} W/cm^2, inducing a coupling between HOMO ($3\sigma_g$) and HOMO-1 ($1\pi_u$).

The results shown above are calculated with LDA functional, and field having trapezoidal envelope with fixed nuclei during the propagation of the molecular wavepacket. The LDA functional does, however, not have a correct 1/r tail in the potential. Thus, we would like to clarify that such enhanced ionization from inner shell orbitals is not caused by the incorrect asymptotic potential tail. Since LB94 functional [112] has a correct 1/r tail, we have also performed simulations with this functional for the same laser parameters at wavelength of 400 nm and intensity of 5×10^{13} W/cm^2 and polarization parallel to the molecular axis of N_2. The results are presented in Fig. 4.4. As expected, because of the correct 1/r tail, the ionization calculated with LB94 functional (right) is smaller than the result from LDA calculation (left). But the ionization behavior and the relative orbital contributions in both cases are very similar. The ionization of coupled orbitals ($2\sigma_u$ and $3\sigma_g$) are dominant in both cases and the relative ionization yield is also similar. Therefore, the 1/r tail has no influence on the enhanced ionization from inner orbitals. In our calculations, trapezoidal envelope of the laser pulse is used, because we need a pulse of relatively short duration to reduce

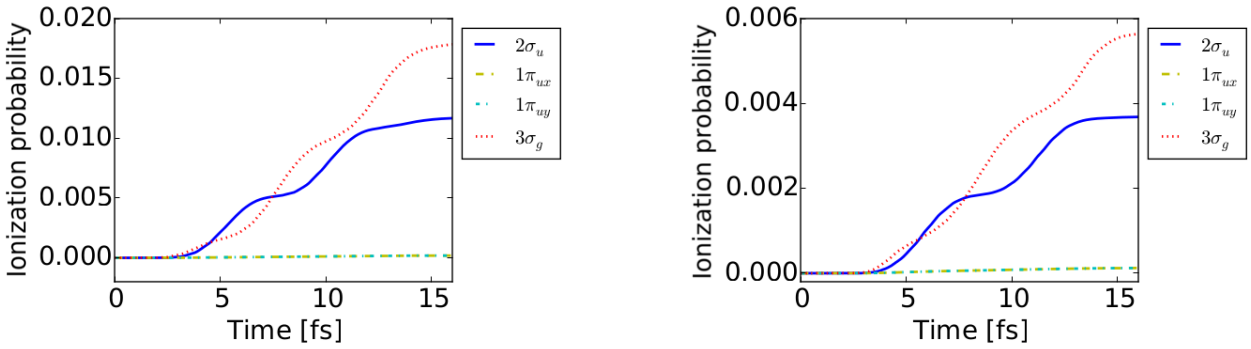

Figure 4.4: Comparison of ionization from N_2 between LDA (left) and LB94 (right) functionals. Laser field has a wavelength of 400 nm and intensity of 5×10^{13} W/cm^2 with polarization parallel to the molecular axis of N_2. Only the relevant KS orbitals which exhibit an significant response to the laser field are shown with their labels.

the simulation time. However, trapezoidal envelope has a point of discontinuity in the derivative, which is not physical and might produce some unphysical results. We have checked this carefully

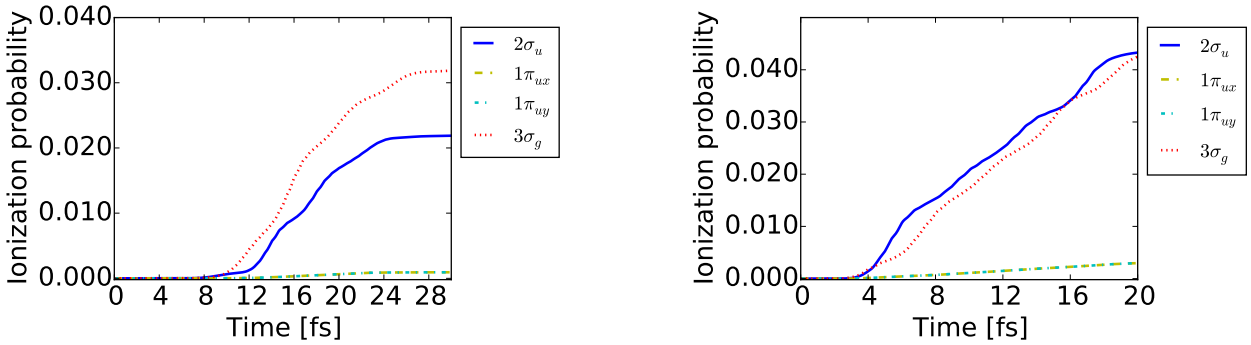

Figure 4.5: Comparison of ionization from N_2 between $\sin^2$ (left) and trapezoidal (right) envelope. Wavelength is 400 nm and intensity is 8×10^{13} W/cm^2 with polarization parallel to the molecular axis of N_2. Only the relevant KS orbitals which possess an important response to the laser field are shown with their labels.

by comparing the result between $\sin^2$ and trapezoidal envelopes in Fig. 4.5. Compared with trapezoidal envelope (right), the relative ionization from HOMO-2 to HOMO is still enhanced, but not as strong as for trapezoidal envelopes, which is understandable because the amplitude of laser field for $\sin^2$ envelope changes with time which influences the coupling.

The results shown above are obtained in simulations with fixed nuclei during the propagation of the molecular wavepacket. Since the molecule vibrates and the corresponding movement of the nuclei plays a role in the electron dynamics, we would also like to see if the results change for simulations without fixed nuclei. If the effect disappears then such enhanced ionization is not measurable in an experiment. To this end, the nuclei are propagated on a mean potential surface corresponding to an electronic superposition state [181]. The results is shown in Fig. 4.6, the enhanced ionization from HOMO-2 is still present for simulations with moving nuclei. The relative ionization of HOMO-2 to HOMO is not as strong as that for fixed nuclei because the energy gap between the two states can change slightly with the internuclear distance.

The way we calculate the ionization from Kohn-Sham orbital based on Eq. (4.2) need to be carefully examined when a coupling is present. Without any coupling, the wavefunction of the

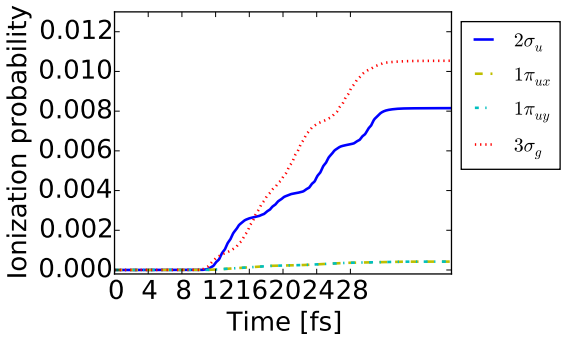

Figure 4.6: Ionization of KS orbitals of N_2 with moving nuclei. LB94 functional and trapezoidal envelope are used in simulation. The laser field is set at wavelength of 400 nm and intensity of 5×10^{13} W/cm^2 with polarization parallel to the molecular axis.

KS orbital remains in the initial state during the propagation. In contrast, when a coupling is present, the wavefunction will periodically evolve to the other coupled state. Therefore, when we calculate the population in a state, integration over the KS orbital will include the population of both coupled states. A better way to calculate the population in one of the coupled states is to project the KS orbital to that state

$$n_i^{st} = |\sum_j^N \langle \phi_i(t=0)|\phi_j(t)\rangle|^2, \tag{4.3}$$

where we add superscript st for the population to separate it from the population of KS orbital. Actually, for coupled states, we only need to sum over the coupled KS orbitals. For non-coupled state, n_i^{st} will give the same value as n_i^{ks}. On the other hand, the KS orbital $\phi_i(t)$ at the time of nonzero electric field can be strongly deformed by the electric field and thus we can project the KS orbitals $\phi_i(t)$ at the time of zero-electric field only. Then the ionization can be obtained via

$$P_i^{st}(t) = 1 - n_i^{st}(t). \tag{4.4}$$

We have calculated the state ionization according to Eq. (4.4). The results for the same situation as in Fig. 4.3 is presented in Fig. 4.7. Compared to Fig. 4.3, we get similar ionization yields

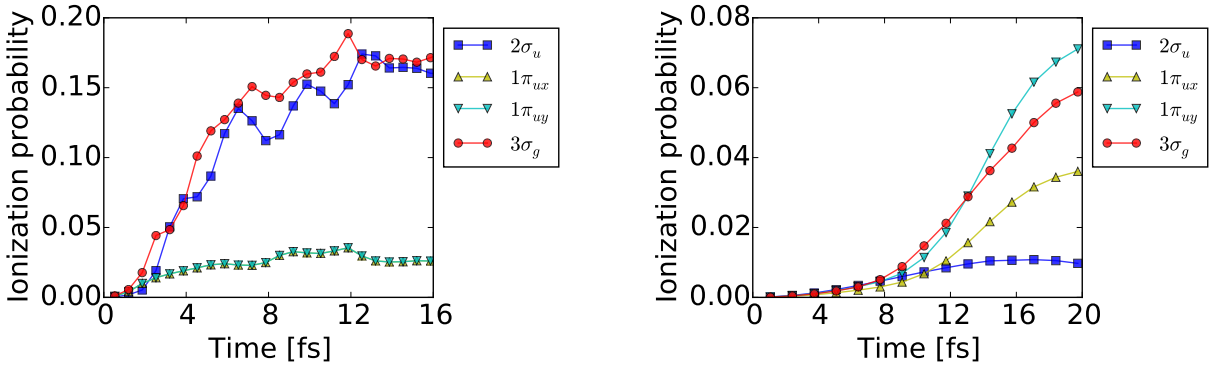

Figure 4.7: Ionization yields of states of N_2 at the time of zero electric field. Only the relevant states which possess an important response to the laser field are shown with their labels. Left: Laser field is parallel to the molecular axis at 400 nm and intensity of 2×10^{14} W/cm^2 inducing a coupling of HOMO ($3\sigma_g$) and HOMO-2 ($2\sigma_u$). Right: Laser field is perpendicular to the molecular axis at 800 nm and intensity of 2×10^{14} W/cm^2 inducing a coupling of HOMO ($3\sigma_g$) and HOMO-1 ($1\pi_u$).

for each state, which means such correction is not significant in our simulations. From Fig. 4.7, we see that the strongest ionized state for N_2 is HOMO ($3\sigma_g$) and HOMO-2 ($2\sigma_u$) for parallel orientation (left), while for perpendicular orientation the strongest ionized state are HOMO ($3\sigma_g$) and HOMO-1 ($1\pi_u$) (right), which confirms the fact that there is an enhanced ionization from inner valence states when a coupling is induced by laser field.

Such an enhanced ionization from inner valence orbitals arises due to the laser induced coupling. To support this conclusion, we have done a systematic analysis by scanning the laser wavelength from 200 nm to 1000 nm and show in Fig. 4.8 the ionization ratio between the ionization yield for the two coupled orbitals in both cases (panels left for parallel alignment and panels right for perpendicular alignment). From the upper two panels in Fig. 4.8, one can see that the ionization from inner valence orbital is enhanced over a relatively wide wavelength range with a peak ratio close to 1 at the optimal wavelength for the coupling. We also studied the ionization ratio at coupling wavelength as function of laser intensity. As we can see from the lower panels in Fig. 4.8, the two coupled orbitals have nearly the same ionization yield and increase simultaneously with the increase of laser intensity, which also indicates the coupling instead of the intensity indeed plays a role here.

In order to gain further understanding, we study the instantaneous eigenvalues of valence orbitals in the laser field. In our simulations, after each time-propagation step, the eigenvalue of each orbital is calculated and the results for the two cases in N_2 are shown in Fig. 4.9. The eigenvalue of orbitals that do not couple with any other states oscillate in phase with the oscillations of the electric field of the laser. On the other hand, the eigenvalues of all orbitals have a decreasing trend, which can be understood by the fact that with increase of ionization in the system, it becomes harder to ionize the system further and thus the eigenvalues become smaller. For the two coupled orbitals, their eigenvalues oscillate with opposite phases and around the same mean average value with the same oscillation amplitude. Since the ionization potential is proportional to the eigenvalue of each orbital, at every transition cycle, the two orbitals are equally ionized. Such oscillating ionization of each orbital can also be seen from Fig. 4.3. Based on this argument, such

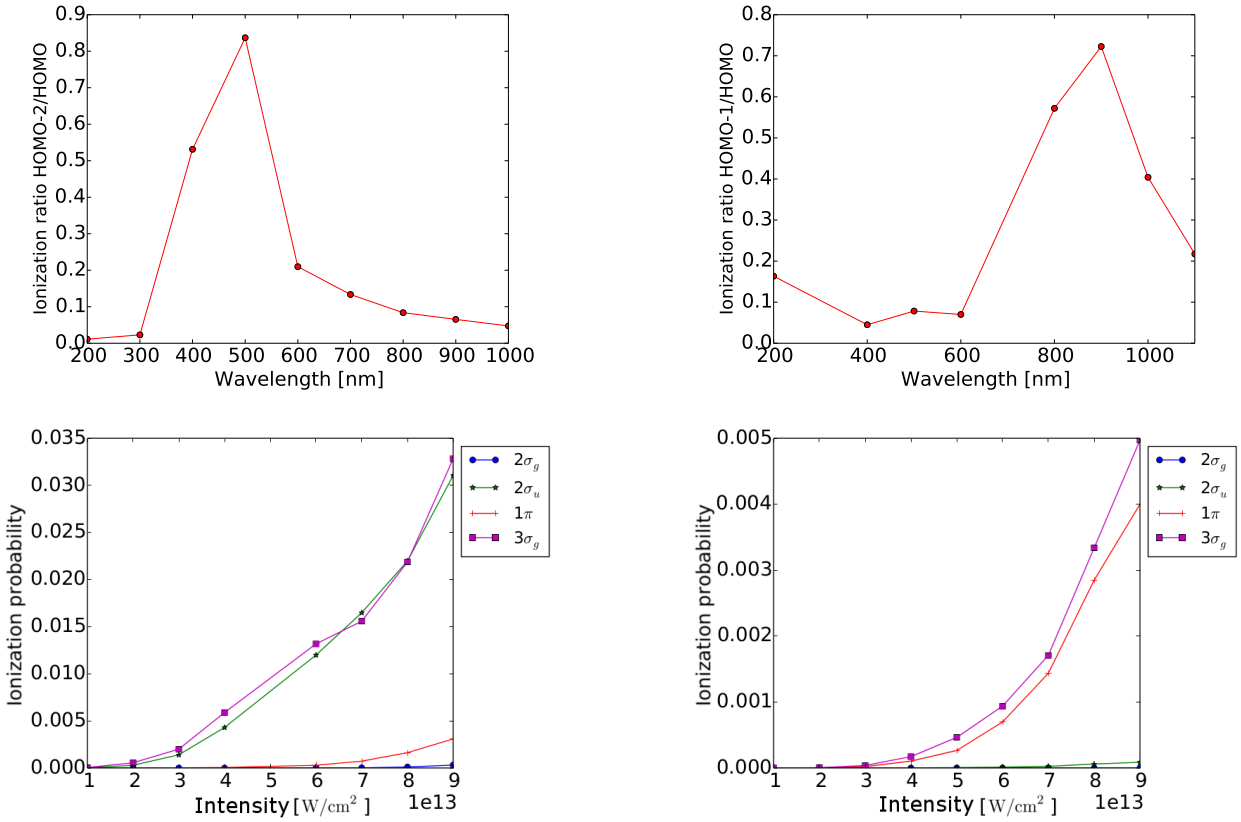

Figure 4.8: Upper pannels: Ratio of ionization yields between HOMO-2 and HOMO (left) and HOMO-1 and HOMO (right) of N_2 as a function of laser wavelength at intensity of 5×10^{13} W/cm^2 and a pulse length of 14 fs. Lower panels: Ionization yields for HOMO and inner valence orbitals as a function of intensity at wavelength of 400 nm (left) and 800 nm (right). Panels on left are for parallel alignment, while panels on right are for perpendicular alignment.

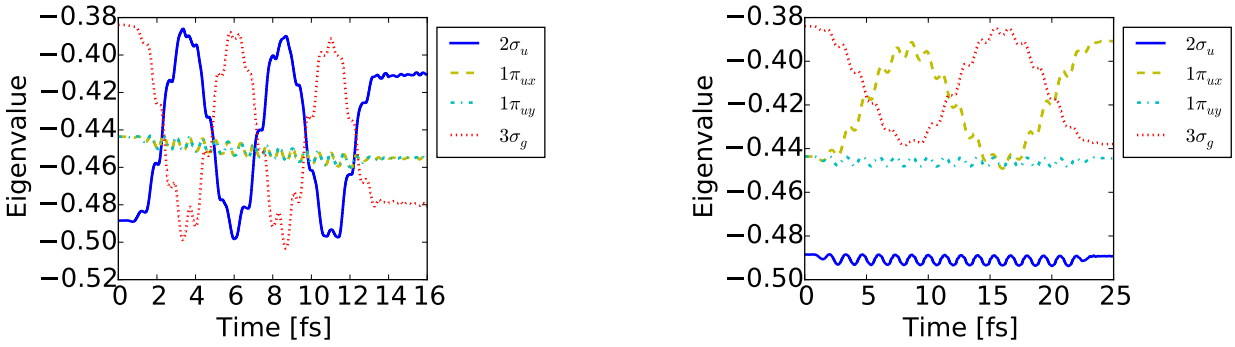

Figure 4.9: Instantaneous eigenvalues of Kohn-Sham Hamiltonian for N_2 valence orbitals for 400 nm laser field at parallel orientation (left) with intensity of 5×10^{13} W/cm^2 and 800 at perpendicular orientation (right) with intensity of 5×10^{13} W/cm^2. Only the relevant KS orbitals, which exhibit significant response to the laser field, are shown with their labels.

mechanism can be detected by measuring the number of excited ions (N_2^+ with a hole in HOMO-2) as a function of time in a pump-probe setup. At times longer than the oscillation period, the two orbitals on average have the same ionization yield.

The reason why the coupled orbitals' eigenvalues oscillate around each other can be analyzed by looking at the projection of the KS orbitals to the other initial states $|\langle\phi_j(t=0)|\phi_i(t)\rangle|^2$. From

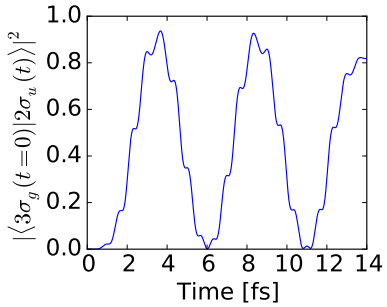

Figure 4.10: The projection of propagated orbital $2\sigma_u(t)$ onto the coupled initial orbital $3\sigma_g(t=0)$. Laser field is at wavelength of 400 nm and intensity of 5×10^{13} W/cm^2 for parallel orientation of molecular axis.

the projection in Fig. 4.10, we can see that the propagated KS orbital $2\sigma_u(t)$ periodically evolves to the other state. Therefore, in the laser field, the coupled KS orbital becomes a mixture of these two coupled states.

For the states in the laser field, it is often convenient to use photon-dressed states within the Floquet picture. Floquet states or laser dressed states have been successfully used to describe the electron response to a strong laser field [3, 182] and are capable to provide an intuitive picture for many physical processes. In the Floquet picture, each state $|\phi\rangle$ has an infinite number of copies that are coupled to n number of photons, denoted as $|\phi, n\rangle$. For the resonance case in our simulation, the two coupled dressed states $|3\sigma_g, n\rangle$ and $|2\sigma_u, n+1\rangle$ become degenerate in the laser field and form two new photon-dressed states which are mixed states of the original states. According to this picture, ionization from the new photon-dressed state indicates that the electron is ionized simultaneously from the two original coupled states. In our simulations, the ionization yields from the two coupled states are indeed close to each other but not exactly. This deviation is due to the

finite pulse duration, since the Floquet picture is strictly applicable for fields of constant amplitude only. An approach to include Floquet picture in the TDDFT formalism will be discussed in Chapter 6.

4.3.1 Total ionization

Since in the case of resonant coupling the ionization is strongly enhanced from an inner valence state, a general question is whether the total ionization is also enhanced and if the consequences of the coupling can be measured in the experiments. This is difficult to check because it is not possible to switch off the coupling effects during the interaction of the laser pulse with the molecule within our simulations. If we force to keep all the inner shell orbitals except the HOMO frozen, then the system is not physical because the HOMO is coupled to HOMO-2 and can result in an unphysical population larger than 2. Instead, we look at the change of the total ionization yield as a function of laser wavelengths as shown in Fig. 4.11. In the corresponding calculation, a 14 fs laser pulse is applied with trapezoidal envelope which has 10 fs constant plateau and 2 fs switch on and off regions. The total ionization decreases smoothly with increasing wavelength. But at the

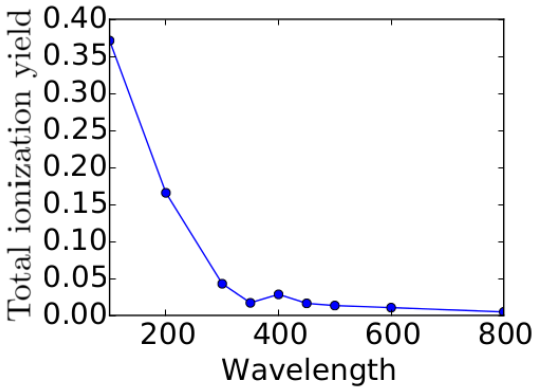

Figure 4.11: Total ionization yield from N_2 as a function of wavelength. The laser electric field is aligned along the molecular axis. Intensity is equal to 5×10^{13} W/cm^2.

resonance wavelength we observe indeed a slightly enhanced ionization.

4.3.2 Ionization of N_2 in filamentation experiments

Enhanced ionization from HOMO-2 of N_2 in interaction with 400 nm laser field has been observed in experiment [183]. In the experiment, a 400 nm laser field with power of 2.3 mJ propagated in air to generate a filament, and the fluorescence from the filament is measured. As a comparison, the fluorescence from filament generated by 800 nm laser field with the same power has been measured. The fluorescence spectra normalized to the same interaction volume are shown in Fig. 4.12. A strong peak from the first negative band, corresponding to the transition from $3\sigma_g$

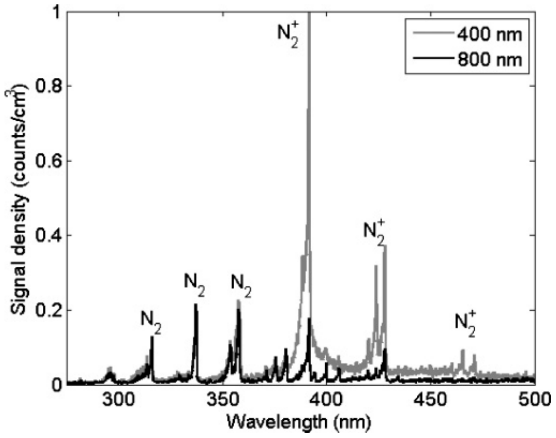

Figure 4.12: Measured fluorescence spectra obtained from laser filaments in air and normalized to the same interaction volume for λ= 800 nm (black) and λ= 400 nm (gray). Fluorescence from the first band obtained for filaments at 400 nm is about 6.4 times larger compared to that at 800 nm. Adapted from [183].

to $2\sigma_u$ in N_2^+, is observed for 400 nm which is about 6.4 times of the signal obtained with the 800 nm laser field. This experiment result suggests an efficient inner-shell ionization for the 400 nm laser field. Such observations agree qualitatively with our simulation results.

The enhanced ionization from an inner valence shell also gives us a deeper insight into the mechanism behind recent observation of abnormal population inversion between ground and excited ionic states in filamentation experiments on N_2 [184, 179, 185, 178]. In the experiment [185], a 800 nm laser field with a power of 3.8 mJ is focused into a chamber full of N_2. A filament is created along the laser propagation direction, in which N_2 is strongly ionized. Then, a weak probe pulse at 400 nm with power of 0.1 μJ is applied and collimated with the 800 nm laser, and the forward

fluorescence spectra is measured as shown in Fig. 4.13. The interesting result is that after applying

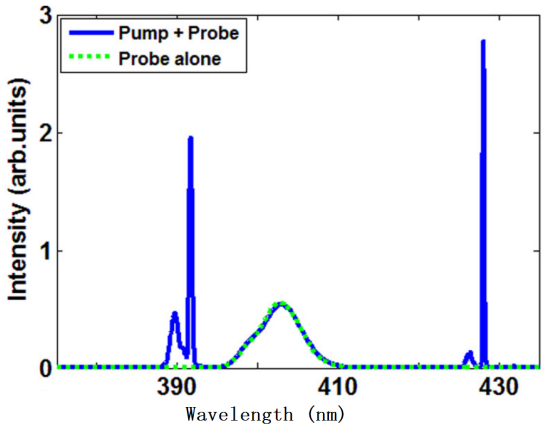

Figure 4.13: The spectra captured with (blue) and without (green) the pump pulse. Laser parameters Adapted from [185].

the 800 nm laser field, the weak 400 nm laser field acting as a seed pulse leads to a strong stimulated emission at 390 nm which correspongds to the transition from HOMO ($3\sigma_g$) and HOMO-2 ($2\sigma_u$). The other peak around 428 nm corresponds to the transition between the same electronic states but different vibrational states. The stimulated emission indicates that there is a strong ionization from HOMO-2 and thus population inversion was created for N_2^+ after applying the 800 nm laser field. Such results are hard to understand because the HOMO-2 is deeply bound. Different models were proposed to explain such abnormal behavior, however, the debates about the mechanism is ongoing [186]. Our simulation results show that for the coupling wavelength at about 400 nm, HOMO-2 can indeed be strongly ionized, which helps us understand better how the deeply bound orbital HOMO-2 can participate in the ionization process.

Since in the experiment the ionization from HOMO-2 is due to the 800 nm laser field which is different to our previous simulations, we have performed another simulation for a two-color laser pulse interacting with N_2 (a weak 400 nm laser field at 1×10^{12} W/cm^2 and a strong 800 nm laser field at intensity of 1×10^{14} W/cm^2) to help us confirm the mechanism. We would like to point out here that the weak 400 nm laser field in our simulation is not to simulate the same effect as in the experiment. The 400 nm laser field in the experiment only acts as a seed to initiate the stimulation

process. The 400 nm laser field in our simulation is considered to arise from the filament which broadens the spectrum of the pulse. Thus, we model the contribution of 400 nm in the filament with a second weak laser field at 400 nm in the simulations. Our simulation results are presented in Fig. 4.14. Although the 400 nm laser field is very weak, there is still a strong ionization from

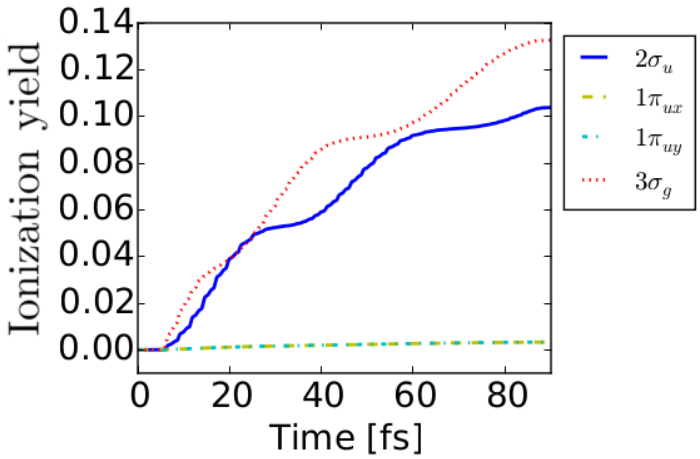

Figure 4.14: Ionization yield of N_2 orbitals with two-color laser field: 400 nm with intensity of 10^{12} W/cm^2 and 800 nm with intensity of 10^{14} W/cm^2. Both laser field are in parallel to the molecular axis.

inner shell orbital. Therefore, our simulations suggest that the spectral broadening of the laser pulse in the filament might play an important role in inducing coupling between the orbitals and an enhanced ionization.

4.4 Ionization from other molecules

Based on our further simulation results, the enhanced ionization from inner shell orbitals is a very general phenomenon that is not only observed for N_2, but also for other molecules such as CO_2, C_2H_4, and C_2H_6. For CO_2, which has an electronic configuration $(1\sigma_g)^2(1\sigma_u)^2(2\sigma_g)^2(3\sigma_g)^2(2\sigma_u)^2$ $(4\sigma_g)^2(1\pi_u)^4(3\sigma_u)^2(1\pi_g)^4$, we have found that a coupling between $1\pi_u$ and $1\pi_g$ can be induced with a 350 nm laser field at parallel orientation. The ionization of the strongly adapted states are shown in Fig. 4.15. For CO_2, the dominant ionization at this wavelength is not the HOMO

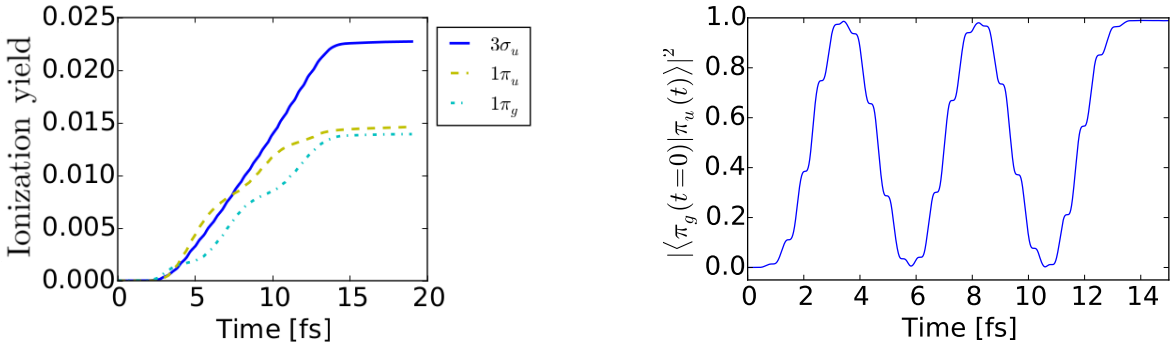

Figure 4.15: Ionization of valence orbitals of CO_2 at 350 nm laser field and intensity of 1×10^{14} W/cm^2 in parallel to the molecular axis. Only the relevant KS orbitals which possess an important response to the laser field are shown with their labels.

($1\pi_g$) but HOMO-1 ($3\sigma_u$). This is because at parallel orientation, HOMO-1 ($3\sigma_u$) is easier to ionize than HOMO ($1\pi_g$) and HOMO-2 ($1\pi_u$). The ionization from HOMO-2 ($1\pi_u$) and HOMO ($1\pi_g$) is suppressed due to the symmetry of the orbitals. We note that for CO_2, there also exist filamentation experiments [179], in which inversion population is observed, corresponding to an enhanced ionization from HOMO-1, in agreement with our results.

We also studied other polyatomic molecules like C_2H_4. A 400 nm laser field is applied parallel to the carbon-carbon bond, which couples HOMO-3 ($1b_{2u}$) and HOMO-1 ($1b_{3g}$), as can be seen from the projection in Fig. 4.16. HOMO ($1b_{3u}$) is still the dominantly ionized orbital. However, we see that the ionization from HOMO-3 is enhanced and becomes comparable to that of HOMO-1. Compared to ionization from HOMO, their ionization yields are relatively small, due to the symmetry of both HOMO-3 and HOMO-1, which suppresses the ionization along the carbon-carbon bond axis. Thus in this case, although a coupling is induced and enhances the ionization, the effect remains relatively small. For C_2H_6, a laser field with wavelength of 200 nm and intensity

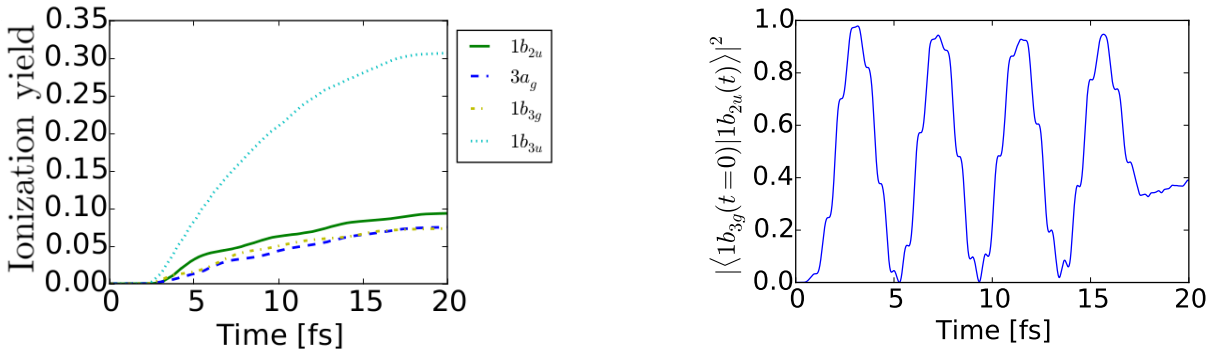

Figure 4.16: Ionization of valence orbitals of C_2H_4 (left) and projection between the coupled states (right). The laser field is at wavelength of 400 nm and intensity of 1×10^{14} W/cm^2 with polarization perpendicular direction to the molecular axis but in parallel to the plane where the molecule lies. Only the relevant KS orbitals which possess an important response to the laser field are shown with their labels.

of 1×10^{14} W/cm^2 is applied to induce coupling between HOMO-1 ($3a_{1g}$) and HOMO-3 ($2a_{2u}$) with polarization parallel to the carbon-carbon bond. As shown from Fig. 4.17(left), the top three strongly ionized orbitals are HOMO ($1e_u$), HOMO-1 ($2a_{2u}$), and HOMO-3 ($2a_{1g}$). The ionization

from HOMO is actually slightly suppressed due to its symmetry. The ionization of HOMO-3 is strongly enhanced and approaches ionization rate of HOMO-1 as a result of the coupling.

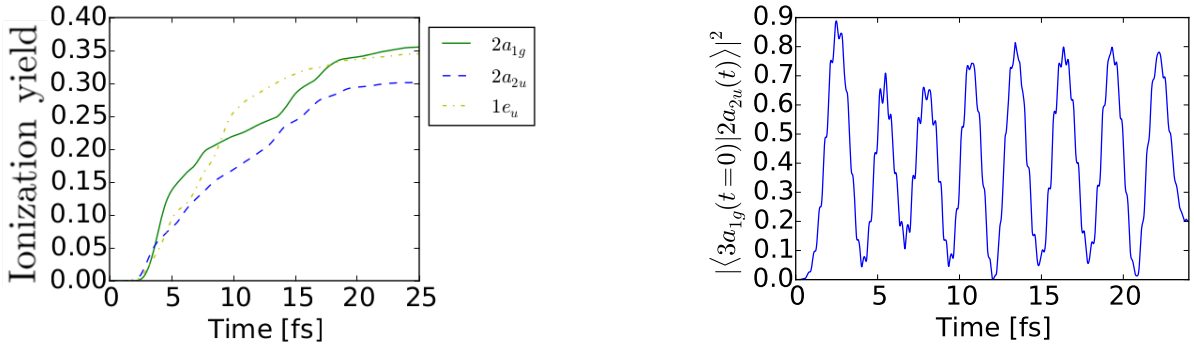

Figure 4.17: Ionization of KS orbitals of C_2H_6 (left) and the projection of coupled states. Laser field parameters: 200 nm and 1×10^{14} W/cm^2 , electric field is parallel to the carbon-carbon molecular axis. Only the relevant KS orbitals which exhibit significant response to the laser field are shown with their labels.

4.5 Summary

In this Chapter, we have shown that the ionization yield strongly depends on orbital symmetry and ionization potential. Ionization from inner valence state is usually orders of magnitude smaller than ionization from HOMO. However, this does not hold true when a laser field induces a strong coupling between inner valence orbitals and HOMO. In that case, strong ionization from inner valence orbitals can be observed. Such phenomenon is rather general and can be observed for di- and polyatomic molecules. Results of our simulations provide better understanding how inner valence orbitals participate in the ionization process. The results are useful to help us analyze observations in filamentation experiments. As ionization is strongly related to dynamical electron localization, we will study electron localization in the coupling regime in the next Chapter.

Chapter 5

Nonadiabatic electron localization [1]

Since the invention of laser in 1960s, research on light-matter interaction in quantum system such as atoms, molecules and solids extends our knowledge about the mechanism of electron response to the light field. As a consequence, new nonlinear nonperturbative phenomena like ATI, HHG were discovered, as discussed in previous Chapters. Usually, it is assumed that electrons follow the change in the oscillating electric field of the laser adiabatically. This means, for example, that the electron density will swap periodically from one side to the other in an atom or a molecule. On the other hand, more recently, dynamic electron localization and nonadiabatic behavior has been seen for such high intense laser fields. Laser induced nonadiabatic dynamics can influence the excitation and ionization behavior of molecular systems. Therefore, nonadiabatic electronic effects must be taken into account when attempting to image or control molecular dynamics through ionization, HHG or fragmentation. The nonadiabatic effects are also prominent in processes such as vision [187], intersystem crossing [188, 189, 190], and many photochemical reactions [191, 192, 193]. In order to achieve the goal of coherent control of such processes, it is important to study and understand nonadiabatic effects.

Adiabatic electron response is usually assumed in atoms, especially in rare gas atoms, due to the large spacing of electronic energy states. Compared to atomic systems, the electronic states in molecules are usually much closer to each other and thus a nonadiabatic behavior is easier to induce and observe in molecules. The nonadiabatic behavior is also easier to observe in large

[1] Part of the results in this Chapter are presented in the review by M. R. Miller, Y. Xia, A. Becker and A. Jaron-Becker, "Laser driven nonadiabatic electron dynamics in molecules", accepted for publication.

molecules because the time for an electron inside a large molecule to traverse is longer, in favor of inducing nonadiabatic response to external laser field [40, 41, 42]. Such nonadiabatic response in larger, conjugated molecules, like linear conjugated systems and aromatic molecules were studied by Lezius et al. [40, 41] and Markevitch et al. [194, 195], respectively. Lezius et al. examined the mass spectra of three linearly fully conjugated all-trans-hydrocarbons of increasing length. They showed that only two peaks are found for the smallest molecules indicating stable production of the first two charge states of ions, resulting in little fragmentation. On the other hand for large molecules the mass spectrum shows extensive fragmentation of molecules, indicating nonadiabatic electron dynamics. However, the spectrum also strongly depends on the wavelength, as shown in Fig. 5.1. Stronger fragmentation at wavelength of 800 nm is observed than longer wavelength of

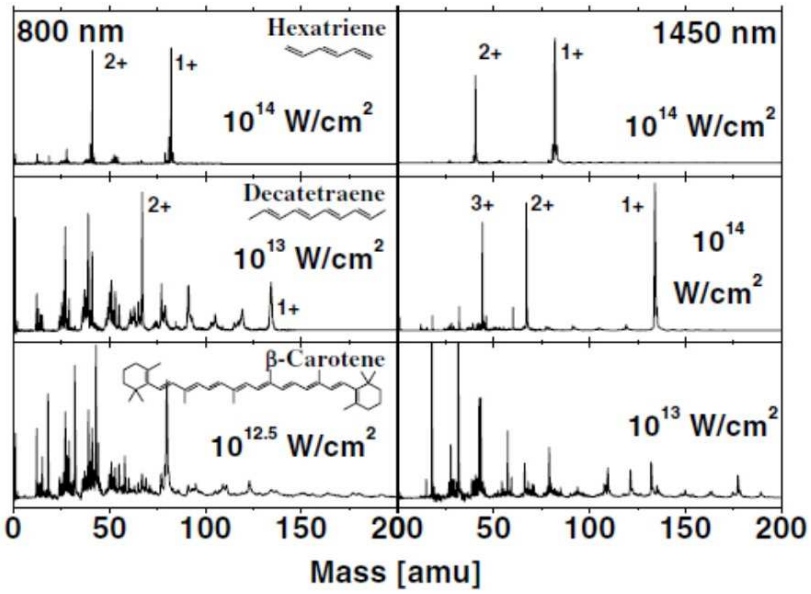

Figure 5.1: Ionization and fragmention patterns represented by the mass spectra of hexatriene, decatetraene and β-carotene for the interaction with laser pulse at 800 nm and 1450 nm. Adapted from [40].

1450 nm. It was pointed out by Lezius et al. that at 800 nm, the duration of the field oscillation was insufficient for the electron to traverse the large molecules adiabatically, while the 1450 nm field can afford the electron wavepacket with sufficient response time. Intramolecular nonadiabatic behavior is also found for small conjugated molecules [196, 54, 197, 198, 199]. For example, the

interaction of the anthracene 1+ cation with a strong electric field of laser leads to nonadiabatic instantaneous dipoles and such nonadiabatic behavior becomes stronger at high intensities [198].

Even for simple one-electron system H_2^+, strong nonadiabatic electron localization can be observed. Zuo and Bandrauk [173, 162] investigated the coupling between charge-resonant states $1\sigma_g$ and $1\sigma_u$ for different internuclear distance. At large internuclear distances, these two states become nearly degenerate and strongly couple to the laser field and can lead to CREI at some critical internuclear distance [200, 173, 162]. What is important is that CREI coincides with the regime where nonadiabatic behavior is present. Previous studies have shown that the degeneracy of the relevant states can lead to the result that population is preferentially trapped in the uphill well [174]. The importance of such nonadiabatic behavior becomes obvious when one examines the temporal dynamics of the electron in the CREI regime. The time resolved studies of ionization of H_2^+ and electron behavior demonstrate that the ionization was not only enhanced but that the timing of peak ionization could be changed as well as shown in Fig. 5.2. Unlike ordinary case, the localized electron does not follow the laser field adiabatically from one nucleus to the other. The electron dynamics instead exhibits two strong localization events on each side for every half laser cycle as shown in Fig. 5.2 (c). This led to the discovery of the so-called multiburst ionization [201].

The study of the response of electron to laser field can ultimately provides a convenient tool for manipulation of the intramolecular electron dynamics and control of the molecular dynamics or potentially provides new tools for control of chemical reactions. In this Chapter, we are going to study the electron dynamics in the coupling regime where enhanced ionization as well as fractional harmonics are observed as discussed in previous Chapters.

5.1 Coupling induced nonadiabatic electron dynamics

As we have discussed, fractional harmonics can be generated for N_2^+ with 400 nm laser field for parallel orientation due to the additional Rabi transition induced electron dynamics. At the coupling regime, the laser-induced instantaneous dipole behaves nonadiabatically, as it has been

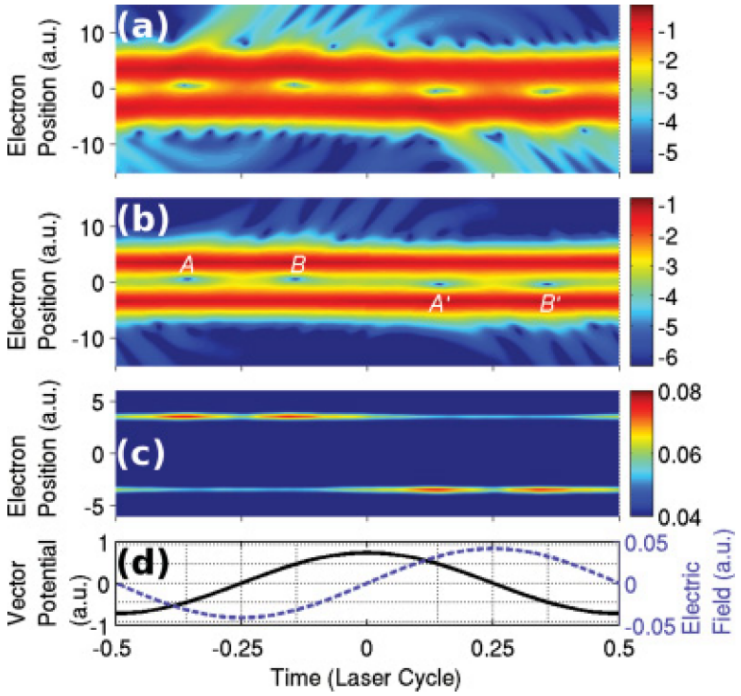

Figure 5.2: Multiburst ionization from H_2^+ at internuclear distance of R=7.0 a.u. along the molecular axis in a strong laser field (shown in d) using (a) 1D model and (b, c) 2D model. Adapted from [201]

shown in Fig. 3.5(b). Since the coupled orbitals are $2\sigma_g$ and $3\sigma_u$, which can lead to electron localization, we would also expect strong nonadiabatic effects in this case. In order to visualize the electron localization directly, we analyzed the density of the HOMO-2 (spin-up) along the molecular axis by integrating over the other two dimensions

$$\rho_{2\sigma_u\uparrow}(z,t) = \int dxdy|\phi_{2\sigma_u\uparrow}(\mathbf{r},t)|^2. \tag{5.1}$$

The density plots of the coupled orbital HOMO-2 of N_2^+ along molecular axis are presented in

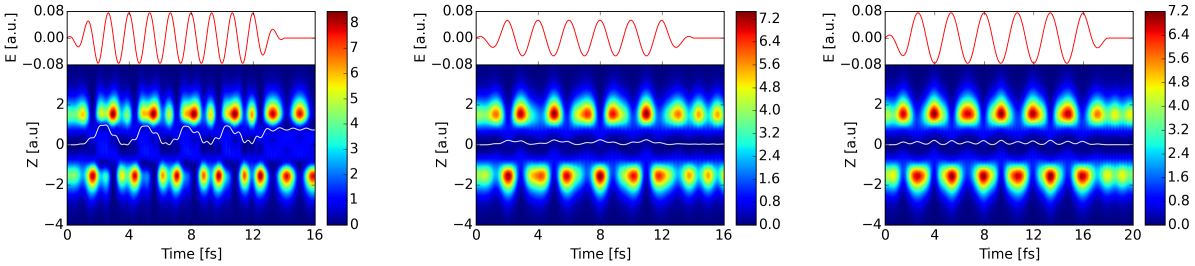

Figure 5.3: The electron density of HOMO-2 of N_2^+ along molecular axis for different laser wavelength: 400 nm (left), 600 nm (middle), and 800 nm (right). The white curve is the electron population transfered from HOMO-2 to HOMO.

Fig. 5.3 for different laser wavelengths: 400 nm (left), 600 nm (middle), and 800 nm (right). The electron localization at resonant case has a strong nonadiabatic behavior but becomes adiabatic, when the laser frequency is off-resonant (800 nm). For the near resonant wavelength of 600 nm, the electron density behaves more adiabatically but still presents some nonadiabatic effect since it does not oscillate symmetrically. This confirms that the nonadiabatic behavior of the time-dependent electron density comes from the coupling between states $2\sigma_u$ and $3\sigma_g$. Such nonadiabatic behavior can be understood by decomposing it into two competing processes. The 400 nm laser field first couples the two states, which leads to nonadiabatic localization as part of the electron dynamics and consequently the localized electron oscillates along the molecular axis at Rabi transition frequency Ω_r. Second, the laser field itself can drive the electron periodically along the molecular axis with the laser frequency. The second process is indeed the adiabatic response of the electron to the electric field of the laser pulse. In Fig. 5.3(left), we also plotted the projection from HOMO-2 to HOMO which has a frequency of Ω_r. In the nonadiabatic case, the electron is basically oscillating

from one side of the molecule to the other side with the Rabi frequency. On the other hand, there is also a modulation in the electron density corresponding to the peaks of the laser electric field. Thus, the electron behavior can be understood as a superposition of such two processes. In the next subsection we discuss the effect of the laser intensity on the nonadiabatic electron dynamics.

5.2 Dependence of nonadiabatic behavior on laser intensity

As we mentioned at the outset of this Chapter, nonadiabatic behavior is mainly found for interaction at high laser intensities. Therefore, it is interesting to analyze how the electron behavior changes with intensity. To this end, we have done simulations for N_2^+ at 400 nm laser field with parallel orientation, which will induce the coupling between HOMO-2 and HOMO. Four different intensities are investigated: 1×10^{13} W/cm^2, 5×10^{13} W/cm^2, 1×10^{14} W/cm^2, and 3×10^{14} W/cm^2. The results are presented in Fig. 5.4. The electron behavior is very different at different laser

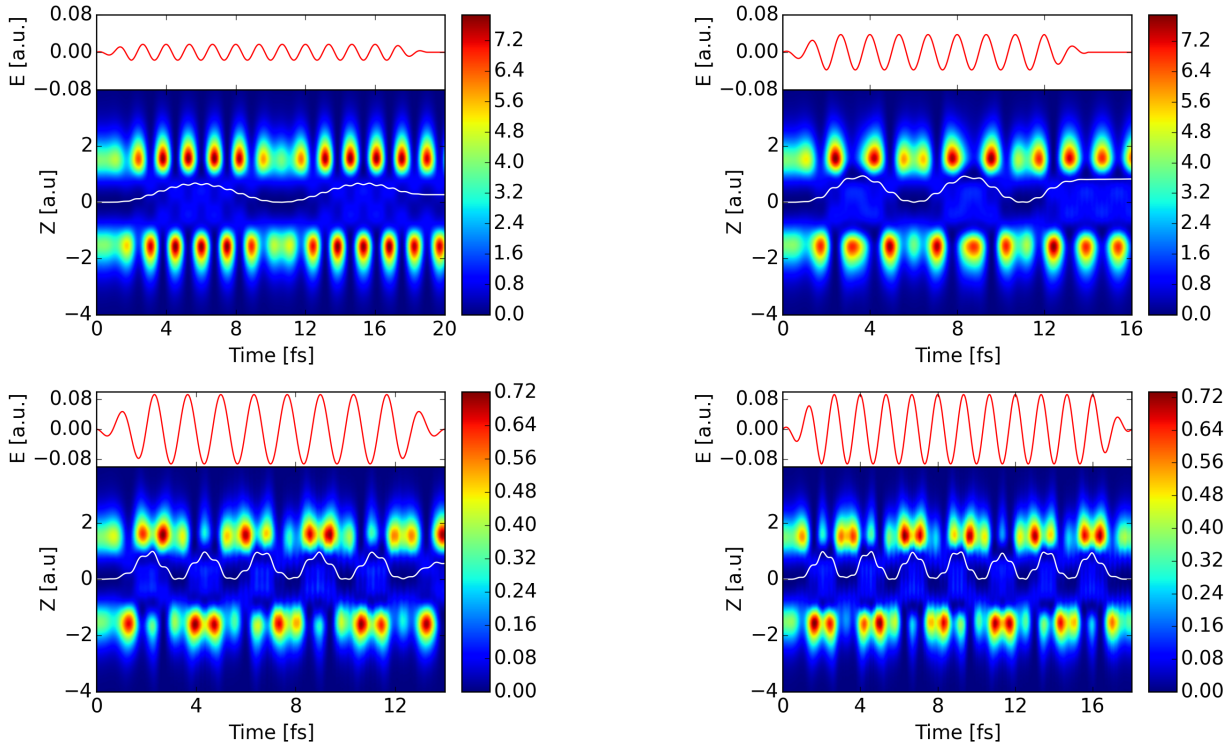

Figure 5.4: Electron density of HOMO-2 from N_2^+ at different laser intensity: 1×10^{13} W/cm^2 (a), 5×10^{13} W/cm^2 (b), 1×10^{14} W/cm^2 (c), and 3×10^{14} W/cm^2 (d). Laser wavelength is fixed at 400 nm.

intensities. At relatively low intensities of 1×10^{13} W/cm^2, the electron is almost following the laser field adiabatically. However, when laser intensity increases, nonadiabatic behavior begins to show up. As we mentioned above, the interaction with the laser field leads to two competing processes: electron oscillates at Rabi frequency due to the coupling effect and electron oscillates following the electric field. Such two processes depend strongly on the electric field amplitude. At relative low intensity 1×10^{13} W/cm^2, the electron's behavior is dominated by the second process and thus behaves more adiabatically. While at stronger laser field, such two processes are comparable to each other which results in a strong nonadiabatic response to the laser field and more complex dynamics.

Our simulation results indicate that the coupling between different states may not necessarily always result in nonadiabatic behavior. At low intensity, the electron can still behave adiabatically, following the laser field. The two competing processes govern the behavior of the electron inside a molecule and the nonadiabatic response is easier to see at strong intense laser field. Through the control of the Rabi frequency via the electric field strength, one can control the nonadiabatic dynamics. All of the results that have been shown so far are obtained for one laser pulse. In the next section we present results for interaction of the molecule with bichromatic laser pulse with one of the frequencies tuned to induce the coupling leading to nonadiabatic dynamics.

5.3 Nonadiabatic localization in two-color laser field

While the two competing processes in previous section are two aspects of the dynamics driven by the same laser pulse, it is interesting to separate such two processes to control them separately. In this section, we therefore show results of simulations with two-color laser field: a 400 nm (resonant) weak laser field at intensity of 1×10^{12} W/cm^2 and a 800 nm (nonresonant) intense laser field at intensity of 1×10^{14} W/cm^2. The simulations were designed to use the 400 nm laser pulse to control the coupling effect, while using the 800 nm laser field to control the second process. Of course, the two effects still cannot be totally separated because the resonant laser field still has influence on both processes. However, we hope such two-color laser field setup can enable us to control it more

or less because of the extra control parameters.

We again study the system N_2^+ and the laser polarization of both fields are parallel to the molecular axis. The results are presented in Fig. 5.5. Since the intensity of the 400 nm laser field

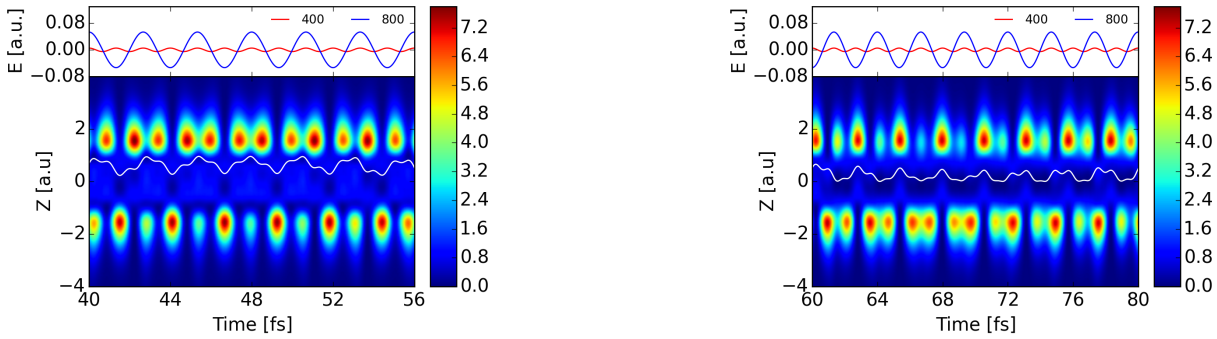

Figure 5.5: The electron density plot from HOMO-2 of N_2^+ in a two color laser field set up: 400 nm laser field at $I = 1 \times 10^{12}$ W/cm^2 and 800 nm laser field at $I = 1 \times 10^{14}$ W/cm^2

is two orders of magnitude smaller than the intensity of the 800 nm field, the second process is mainly influenced by the 800 nm laser field. A strong nonadiabatic response can be still seen in this case, as compared to the previous results for a single laser field at wavelength of 400 nm and lowest intensity of 1×10^{13} W/cm^2, where the electron behaved more adiabatically. Therefore, relative strength of the two competing processes indeed strongly depends on the laser wavelength. What is more interesting is that we have found that during a relative long period (about 20 fs), the electron is on average located more frequently on one side (Fig. 5.5(left)) or on the other side (Fig. 5.5(right)), during the interaction with a 90 fs laser pulse. Such periodic localization preference from one side of the molecule to the other side can be analyzed via the projection of the two coupled orbitals, as for example shown in Fig. 5.6. The projection has two different oscillating frequencies: the high-frequency oscillating component is caused by the 800 nm field and the slow oscillating component is caused by the 400 nm laser field and corresponds to the Rabi frequency. Because of the low intensity, the Rabi frequency is very small in the present case. Therefore, the electron moves very slowly from one side to the other side due to the low intensity of the 400 nm laser pulse, which explains why the electron can locate more frequently on one side for such a long

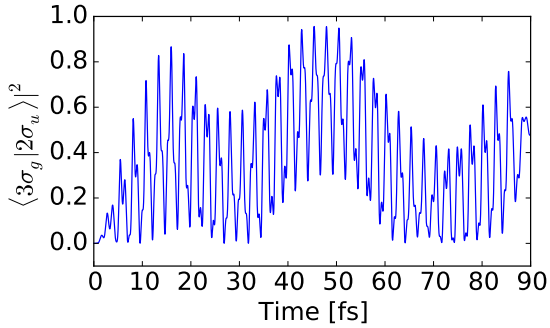

Figure 5.6: The projection from HOMO-2 to HOMO of N_2^+ for two-color laser field: 400 nm laser field at $I = 1 \times 10^{12}$ W/cm^2 and 800 nm laser field at $I = 1 \times 10^{14}$ W/cm^2.

time period.

Control of electron localization in H_2^+ at large internuclear distance has been reported previous in [202, 203]. The coupling of the nearly degenerated $1\sigma_g$ and $1\sigma_u$ states can lead to permanent trapping of the electron on one side. The control of such permanent trapping is very appealing since it can influence strongly related processes such as ionization, dissociation as well as other chemical reactions. Although our simulations with bichromatic field are still far from showing permanent trapping of the electron on one side, it however helps to understand better the mechanism behind it and opens up the possibility to study the conditions of permanent trapping in multielectron molecules.

5.4 Electron localization in other molecules

According to the discussion in previous sections, the electron dynamics can be strongly influenced by the coupling of the orbitals. For N_2^+, the coupling can be induced between for σ_g- and σ_u-type orbitals. In Chapter 3 and Chapter 4, we have shown fractional harmonics and enhanced ionization for other molecules as well. For some of these molecules the efffect are due to the coupling of orbitals with other symmetries.

For $C_2H_2^+$, a 760 nm laser field is used to couple $2\sigma_u$ and $3\sigma_g$, which has the same type of orbital coupling as N_2^+. The density plot of $2\sigma_u$ is shown in Fig. 5.7(a), we see a strong

nonadiabatic dynamics of electron localization but is different compared to N_2^+. For $C_2H_4^+$, one can couple orbitals $1b_{2u}$ and $1b_{3g}$ at 400 nm. The orbital density for $1b_{2u}$ is shown in Fig. 5.7(b) for the laser intensity of 1×10^{14} W/cm^2. The electron response is almost adiabatic with small nonadiabatic signatures. It is surprising when compared with N_2^+ at the same resonant wavelength and intensity, where nonadiabatic behavior is already clearly visible. This indicates that the dynamic localization can also depend on the orbital type. For CO_2^+, where $1\pi_u$ and $1\pi_g$ orbitals are coupled for a laser field of wavelength of 350 nm and intensity of 1×10^{14} W/cm^2, the electron density (in Fig. 5.7(c)) almost follows the laser field adiabatically. We also studied the density plot of the coupled orbital $4b_2$ and $6a_1$ of NO_2, shown in Fig. 5.7(d). The non-adiabatic effect is weak compared to N_2^+ at the same laser intensity. Our simulations are currently limited to smaller molecules due to the computational cost. However, there are no physical arguments which would prohibit the dynamical localization for any open-shell molecule. We have chosen those molecules which due to their electronic properties are more easily accessible for experimental studies. As we pointed out, the effects can strongly depend on the laser intensity and the type of coupled orbital. The choice of systems was also related to visualization of the dynamics, which is not easy for nonsymmetric molecules or σ-π coupling of the orbitals.

5.5 Summary

In this Chapter, we systematically investigated the nonadiabatic electron localization due to the coupling of $2\sigma_u$ and $3\sigma_g$ in N_2^+. The nonadiabatic response of electron is determined by two competing processes: coupling induced oscillations with Rabi frequency and laser induced oscillations with laser frequency. Such competing processes can strongly depend on the laser intensity and thus by changing intensity one can change from adiabatic to nonadiabatic regime for electron dynamics. Moreover, we have explored the possibility of controlling such nonadiabatic behavior with two-color laser pulse and have shown that in such simulations the electron can reside on one nuclei more frequently for relatively long time. The electron localization is also examined for other type of couplings in the regions where we have found strong fractional harmonics and enhanced

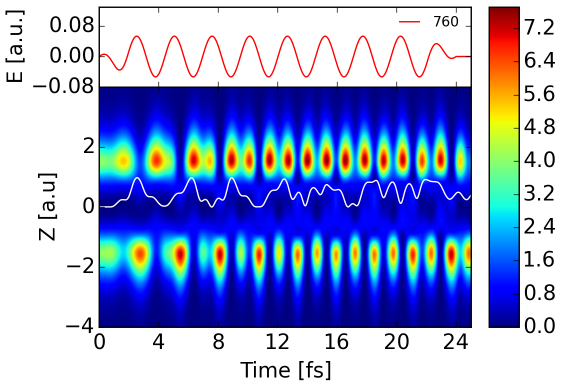

(a) Orbital density of $2\sigma_u$ of $C_2H_2^+$. Laser field: $\lambda = 760$ nm and $I = 1 \times 10^{14}$ W/cm^2

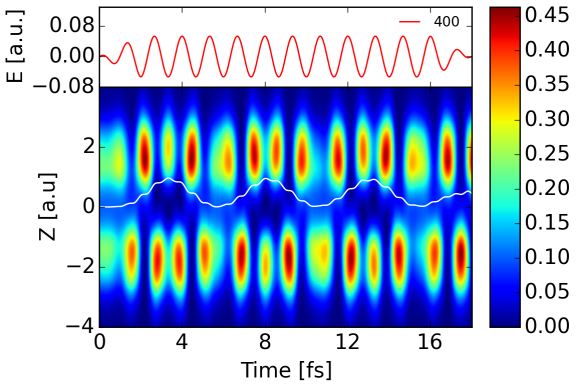

(b) Orbital density of $1b_{2u}$ of $C_2H_4^+$. laser field: $\lambda = 400$ nm and $I = 1 \times 10^{14}$ W/cm^2

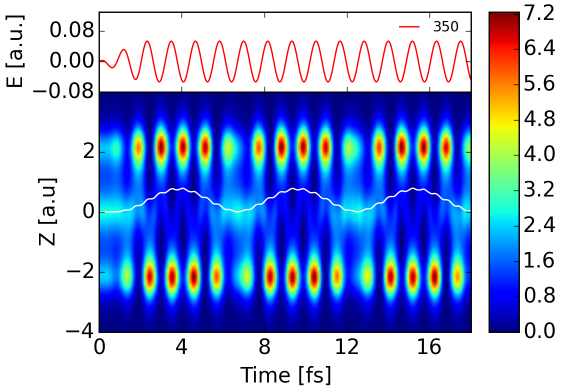

(c) Orbital density of $2\sigma_u$ of CO_2^+. Laser field: $\lambda = 350$ nm and $I = 1 \times 10^{14}$ W/cm^2

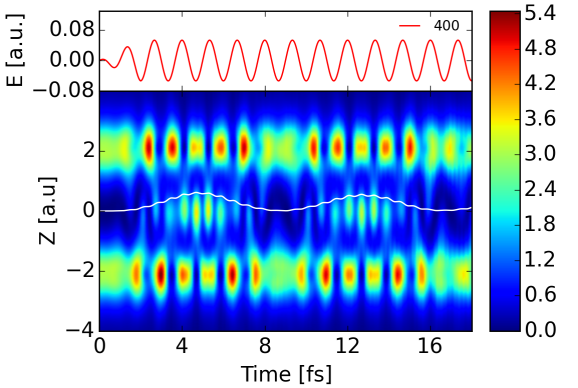

(d) Orbital density of $4b_2$ of NO_2. Laser field: $\lambda = 400$ nm and $I = 1 \times 10^{14}$ W/cm^2

Figure 5.7: Orbital density plot of the coupled orbitals for different molecules.

ionization. For several open-shell molecules nonadiabatic response has been found and illustrated.

Chapter 6

Complex Gaussian basis for non-Hermitian Floquet formalism

A lot of important results in strong field physics of atoms were obtained with theories based on the Floquet theorem. This type of approach was initially developed to obtain exact solutions of the time-dependent Schrödinger equation which describes the interaction between a quantum system and a continuous intense light source which is strictly periodic in time. The wavefuction of the system describing the photo-induced effects is represented in an extended Hilbert space spanned by photon dressed states, which are constructed as a direct product of system and field states. This approach allows to transform the original time-dependent problem into a time-independent formulation yielding quasi-stationary eigenstates which can be expressed in harmonics of the carrier frequency of the field. Instead of dealing with time propagation one has the advantage of application of fast diagonalization algorithms. The Floquet ansatz was successfully applied to non-perturbative studies of the bound-bound transitions in atoms and molecules as well as laser-assisted collisions [204, 182, 205, 206]. Moreover, the non-Hermitian version of the Floquet method provides a description of the decaying states via complex scaling [207]. It can therefore be used in the context of resonance as well as ionization, for example it has been applied to study multiphoton ionization of neutral atoms [208] and molecules (e.g. in [209, 210]), multiphoton detachment of negatively charged ions, ac-Stark shifts, laser-induced chemical bond softening and hardening in a molecule [211], as well as multiphoton dissociation [182, 212], Coulomb explosion, and high harmonic generation [213, 214]. Floquet-based methods not only give results in agreement with experiments, they allow, due to the inherent, intuitive picture of laser-dressed states, for straightforward interpreta-

tion of the results, e.g. determination of the states responsible for transient resonances in high harmonic spectrum [205] as well as identification of key mechanisms. In this way it can help in the development of simplified models.

Formally, Floquet method is limited to time-periodic problems such as interaction of systems with cw-lasers. In recent years, this limitation of the Floquet theory has been overcome and Floquet theory has been adapted to the treatment of laser fields whose amplitudes are varying in time. For example, reasonable results were obtained already for relatively short laser pulses composed of 5 optical cycles. Moreover, it has been shown that with slight modifications one can reformulate the problem to describe the interaction with ultrashort laser pulses [215].

The way to make such approach applicable to larger polyatomic molecules is to combine the time-dependent density-functional theory (TDDFT) with the Floquet method [204, 182, 216] The first applications of this method both in linear response regime [217] and in nonperturbative regime [59, 60, 62, 63, 64] are promising. However, in the nonperturbative regime only grid-based calculations were performed and it is very interesting to explore possibilities of the Floquet-based density-functional theory (DFT) method using the basis-set approach. The Floquet-dressed states might give us better physical picture to understand the multiorbital contributions from inner valence orbitals to the high harmonic generation as well as ionization.

In this thesis, we apply Floquet theorem to solve the time-dependent Schrödinger equation (TDSE) with Gaussian basis sets. Complex basis set is used to enable the description of bound-free and free-free transitions. We designed an optimization process which yield a very accurate calculation of ionization rate. First applications regarding one- and two-photon ionization will be presented.

6.1 Floquet theorem

A system subject to a time-dependent external potential, is described by the time-dependent Schrödinger equation

$$i\hbar\frac{\partial}{\partial t}\Psi(\mathbf{r},t) = \hat{H}(\mathbf{r},t)\Psi(\mathbf{r},t), \tag{6.1}$$

where $\hat{H} = \hat{T} + \hat{U} + \hat{V}$. According to the Floquet theorem [218], if the external potential V is periodic in time $V(t+T) = V(t)$, then the (ground state) solution of Schrödinger equation (6.1) can be written as superposition of so-called quasienergy states given by

$$\Psi_\lambda(\mathbf{r}, t) = e^{-i\varepsilon_\lambda t}\Phi_\lambda(\mathbf{r}, t), \tag{6.2}$$

where

$$\Phi_\lambda(\mathbf{r}, t+T) \quad = \quad \Phi_\lambda(\mathbf{r}, t), \tag{6.3}$$

and ε_λ is called quasienergy. Substituting $\Psi_\lambda(\mathbf{r}, t)$ into Eq. (6.1), we obtain an eigenvalue equation for the quasienergy:

$$\hat{\mathscr{H}}(\mathbf{r}, t)\Phi_\lambda(\mathbf{r}, t) = \epsilon_\lambda\Phi_\lambda(\mathbf{r}, t), \tag{6.4}$$

where

$$\hat{\mathscr{H}}(\mathbf{r}, t) = \hat{H}(\mathbf{r}, t) - i\frac{\partial}{\partial t}. \tag{6.5}$$

Because of the periodicity of Φ_λ (6.3), we have the following transformation,

$$\varepsilon_\lambda^{'} = \varepsilon_\lambda + n\omega \tag{6.6}$$

$$\phi_\lambda^{'}(\mathbf{r}, t) = \exp(in\omega t)\phi_\lambda(\mathbf{r}, t), \tag{6.7}$$

which means that Floquet states are equivalent, if the quasienergies only differ by $n\omega$ where n is an arbitrary integer number. Such property is the same as for Bloch eigenstates in solid state physics.

Since $\Phi_\lambda(\mathbf{r}, t+T) = \Phi_\lambda(\mathbf{r}, t)$ is periodic in time, its temporal part can be expanded into Fourier series

$$\Phi(\mathbf{r}, t) = \sum_{n=-\infty}^{\infty} e^{-in\omega t} f_n(\mathbf{r}). \tag{6.8}$$

The integer n represents the number of photons absorbed (for positive value) or emitted (for negative value). The space part $f_n(\mathbf{r})$ can be either represented by the value on a numerical grid or spanned by basis sets, such as Sturmian functions [219], Slater functions [209], and Gaussian functions [209, 220]. Considering the great success of real Gaussian basis sets for representation of

bound states, especially for large molecular systems, we have chosen Gaussian basis sets to span the spatial part of the wavefunction. If we denote the basis set functions as $\chi_j(\mathbf{r})$, we can write

$$\Phi_\lambda(\mathbf{r},t) = \sum_{nj} C_{nj}^\lambda \exp(-in\omega t)\chi_j(\mathbf{r}). \tag{6.9}$$

Substituting it into Eq. (6.4), we obtain the following matrix equation

$$\sum_{nj}\left[\langle\chi_i|\hat{H}^{(m-n)}|\chi_j\rangle - m\omega\delta_{nm}S_{ij}\right]C_{nj}^\lambda = \varepsilon_\lambda \sum_j S_{ij}C_{mj}^\lambda, \tag{6.10}$$

where

$$\hat{H}^n(\mathbf{r}) = \frac{1}{T}\int_o^T \hat{H}(\mathbf{r},t)\exp(in\omega t)dt, \tag{6.11}$$

and $S_{ij} = \langle\chi_i|\chi_j\rangle$ is the overlap matrix. The integral $\langle\chi_i|\hat{H}^{(m-n)}|\chi_j\rangle$ can be decomposed as

$$\langle\chi_i|\hat{H}^{(m-n)}|\chi_j\rangle = \langle\chi_i| - \frac{\nabla^2}{2m}|\chi_j\rangle\delta_{nm} + \sum_k\langle\chi_i|\frac{-Z_k}{|\mathbf{r}-\mathbf{R}_k|}|\chi_j\rangle\delta_{nm} + \frac{1}{2}\mathbf{E}\cdot\langle\chi_i|\mathbf{r}|\chi_j\rangle(\delta_{n,m+1}+\delta_{n,m-1}) \tag{6.12}$$

for one electron molecular systems where $\mathbf{R}_k$ denotes the nuclei's positions and $\mathbf{E}$ is the external laser electric field. The three terms on the right hand side are called kinetic-energy integral, nuclear-attraction integral and dipole integral, respectively. We will show how to calculate them for Gaussian basis sets with recursive relationship in section 6.3. When applied to the time-dependent Kohn-Sham equation (2.33) to solve for the case of a multielectron system, the matrix elements include two additional parts: electron-electron repulsion integral $\langle\chi_i\chi_n|\nu_H|\chi_j\chi_m\rangle$ and exchange-correlation integral $\langle\chi_i|\nu_{xc}|\chi_j\rangle$. Eq. (6.10) can be efficiently solved using PETSc or SLEPc numerical libraries [221, 222] which are based on methods to solve eigenvalue problems for large matrices.

6.2 Complex basis sets

Physical phenomena can be either studied via Hermitian formalism or non-Hermitian formalism. Although Hermitian formalism of quantum mechanics can handle most of problems in physics, non-Hermitian formalism can provide a straightforward explanation to some phenomena

which might be very hard or impossible to be explained within the framework of Hermitian formalism such as exceptional points, where two or more degenerate resonance states have coalesced, multiphoton ionization of atoms or multiphoton dissociation of molecules, where bound-free or free-free transitions are present.

There are two popular ways to obtain a non-Hermitian Hamiltonian. One is to apply complex coordinate rotation [223, 224], $r \rightarrow r\exp(i\alpha)$ (complex rotation is usually applied to radius r in spherical coordinate), to the Schrödinger equation (6.1)

$$i\frac{\partial\Psi(r\exp(i\alpha),t)}{\partial t} = \hat{H}(r\exp(i\alpha),t)\Psi(r\exp(i\alpha),t), \tag{6.13}$$

where the Hamiltonian operator $\hat{H}(r\exp(i\alpha),t)$ becomes non-Hermitian. We can again, following Floquet theorem, write the wavefunction $\Psi(r\exp(i\alpha),t)$ as

$$\Psi_\lambda(r\exp(i\alpha),t) = \exp(-i\varepsilon_\lambda t)\Phi_\lambda(r\exp(i\alpha),t). \tag{6.14}$$

Substituting it back into the Schrödinger equation, we get

$$\hat{\mathscr{H}}(r\exp(i\alpha),t)\Phi_\lambda(r\exp(i\alpha),t) = \varepsilon_\lambda\Phi_\lambda(r\exp(i\alpha),t). \tag{6.15}$$

ε_λ is now a complex quasienergy and the imaginary part of quasienergy $\mathrm{Im}(\varepsilon)$ is related to the ionization rate Γ of that state via $\Gamma = -2\mathrm{Im}(\varepsilon_\lambda)$.

The influence of the transformation $r \rightarrow r\exp(i\alpha)$ on the spectrum of a many-body Hamiltonian [225] is that both bound state eigenvalues and the complex eigenvalue associated with resonant states are independent of the rotation angle α while the continuum states are rotated by angle of 2α into the lower half complex energy plane, as shown in Fig. 6.1. If α is large enough, then the complex resonance eigenstates will be exposed and thus we can study the resonance states through the complex coordinate rotation.

The other way to construct non-Hermitian Hamiltonian is to use complex basis set which is equivalent to complex coordinate rotation [226] according to the following transformation

$$\begin{aligned}&\iiint f(r,\theta,\phi)H(re^{i\alpha},\theta,\phi)g(r,\theta,\phi)r^2\sin(\theta)drd\theta d\phi \\ =&e^{-3i\alpha}\iiint f(re^{-i\alpha},\theta,\phi)H(r,\theta,\phi)g(re^{-i\alpha},\theta,\phi)r^2\sin(\theta)drd\theta d\phi,\end{aligned} \tag{6.16}$$

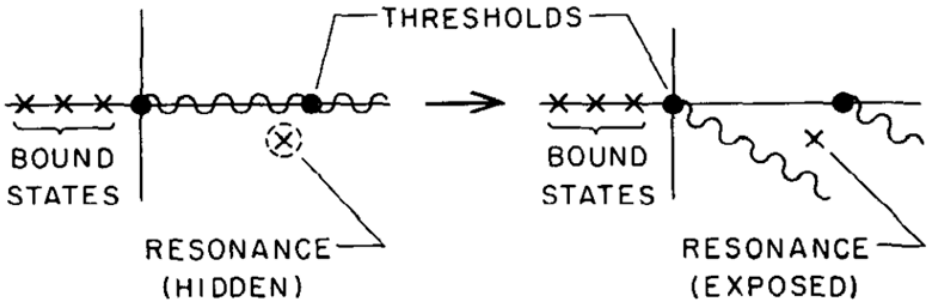

Figure 6.1: Effect of complex coordinate rotation. Bound states and thresholds are invariant. As continuum states rotate, complex resonance eigenvalues may be exposed. Adapted from [225].

where $f(r,\theta,\phi)$ and $g(r,\theta,\phi)$ are real L^2 basis functions. In the above equation, no complex conjugate is applied to left basis set $f(r,\theta,\phi)$ compared to Hermitian case, which is called c-product [227] and denoted as $(f|H|g)$. The complex basis is more appealing compared to the complex-coordinate rotation technique. The rotation of coordinate to complex plane is hard to interpret in the case of molecules while there is no such interpretation problem for the complex basis. Since only continuum is necessary to be rotated into the lower half complex energy plane, only representation of the continuum by the complex basis is necessary and the basis for the bound states can still be kept real. So previous results of Gaussian basis for the description of bound states can be used directly without any modification. On the other hand, different complex basis can have different rotation angle and thus provides even some flexibility.

6.3 Gaussian basis integral

6.3.1 Fundamental integral

As mentioned above, the spatial basis set functions $\chi_j(\mathbf{r})$ can be chosen as Sturmian functions, Slater functions or Gaussian functions. The matrix element evaluation for Sturmian and Slater functions is computationally demanding and thus limits their extension to larger molecular systems. Gaussian basis sets on the other hand have several properties, as illustrated in this section, which make it possible to extend calculations to large systems.

The primitive Gaussian function we consider has the form

$$\phi_{\mathbf{a}}(\mathbf{r}) = N x_a^{l_x} y_a^{l_y} z_a^{l_z} e^{-\alpha_k |\mathbf{r}_a|^2}, \tag{6.17}$$

where $\mathbf{r}_a = \mathbf{r} - \mathbf{A}$, which is centered at position $\mathbf{A}$ with complex exponential α_k and the momentum vector (l_x, l_y, l_z). We use subscript $\mathbf{a}$ here to denote the parameters (position $\mathbf{A}$, momentum vector, and exponential α_k) for a Gaussian basis. In the following, we will just use the subscript $\mathbf{a}$ to represent a Gaussian basis. The normalization coefficient of Gaussian basis is

$$N = \frac{(2\alpha)^{(l_x+l_y+l_z)/2+3/4}}{\sqrt{\Gamma(l_x+\frac{1}{2})\Gamma(l_y+\frac{1}{2})\Gamma(l_z+\frac{1}{2})}}. \tag{6.18}$$

From the fact that the Hamiltonian contains only one- and two-electron operators, it is straightforward to show [228] that most of the matrix elements can be written in terms of integrals of the general form

$$(\mathbf{ab}|\mathbf{cd}) = \iint \phi_{\mathbf{a}}(\mathbf{r}_1)\phi_{\mathbf{b}}(\mathbf{r}_1) f(|\mathbf{r}_1 - \mathbf{r}_2|)\phi_{\mathbf{c}}(\mathbf{r}_2)\phi_{\mathbf{d}}(\mathbf{r}_2) d\mathbf{r}_1 d\mathbf{r}_2. \tag{6.19}$$

For the Gaussian basis, we first consider a more fundamental integral (integral for s-state) [229]

$$I = \iint e^{-\alpha|\mathbf{r}_1-\mathbf{A}|^2} e^{-\beta|\mathbf{r}_1-\mathbf{B}|^2} f(|\mathbf{r}_1 - \mathbf{r}_2|) e^{-\gamma|\mathbf{r}_2-\mathbf{C}|^2} e^{-\delta|\mathbf{r}_2-\mathbf{D}|^2} d\mathbf{r}_1 d\mathbf{r}_2, \tag{6.20}$$

where we ignored the normalization coefficient for convenience. All the matrix integrals in Eq. (6.12) can be written in this general form. For example, the overlap integral,

$$S = I^{overlap} = \int e^{-\alpha|\mathbf{r}-\mathbf{A}|^2} e^{-\gamma|\mathbf{r}-\mathbf{C}|^2} d\mathbf{r}, \tag{6.21}$$

can be obtained by setting

$$\begin{aligned} \beta &= \delta = 0 \\ f(|\mathbf{r}_1 - \mathbf{r}_2|) &= \delta(|\mathbf{r}_1 - \mathbf{r}_2|), \end{aligned} \tag{6.22}$$

in Eq. (6.20). And the nuclear-attraction integral,

$$I^{NE} = \int e^{-\alpha|\mathbf{r}-\mathbf{A}|^2} e^{-\beta|\mathbf{r}-\mathbf{B}|^2} \frac{-Z}{|\mathbf{r}-\mathbf{C}|} d\mathbf{r}, \tag{6.23}$$

can be obtained from Eq. (6.20) using

$$\delta = 0$$

$$\gamma = \infty$$

$$\lim_{\gamma\to\infty} \frac{\gamma^{3/2}}{\pi^{3/2}} e^{-\gamma|\mathbf{r}-\mathbf{C}|^2} = \delta(\mathbf{r}-\mathbf{C})$$

$$f(|\mathbf{r}_1-\mathbf{r}_2|) = -\frac{Z}{|\mathbf{r}-\mathbf{C}|}. \tag{6.24}$$

For the electron-electron repulsion integral, $f(|\mathbf{r}_1-\mathbf{r}_2|)$, we set

$$f(|\mathbf{r}_1-\mathbf{r}_2|) = \frac{1}{|\mathbf{r}_1-\mathbf{r}_2|}. \tag{6.25}$$

The dipole integral can be transformed into the overlap matrix with higher angular momentum Gaussian basis sets, as we will show later.

To evaluate integral Eq. (6.20), we first notice that the product of two Gaussian functions is still a Gaussian function

$$\begin{aligned} e^{-\alpha|\mathbf{r}_1-\mathbf{A}|^2} e^{-\beta|\mathbf{r}_1-\mathbf{B}|^2} &= G_{AB} e^{-\xi|\mathbf{r}_1-\mathbf{P}|^2} \\ e^{-\gamma|\mathbf{r}_2-\mathbf{C}|^2} e^{-\delta|\mathbf{r}_2-\mathbf{D}|^2} &= G_{CD} e^{-\eta|\mathbf{r}_2-\mathbf{Q}|^2}, \end{aligned} \tag{6.26}$$

where

$$\begin{aligned} G_{AB} &= e^{-\frac{\alpha\beta}{\alpha+\beta}|\mathbf{A}-\mathbf{B}|^2}, \\ \xi &= \alpha+\beta, \\ \mathbf{P} &= \frac{\alpha\mathbf{A}+\beta\mathbf{B}}{\alpha+\beta}, \\ G_{CD} &= e^{-\frac{\gamma\delta}{\gamma+\delta}|\mathbf{C}-\mathbf{D}|^2}, \\ \eta &= \gamma+\delta, \\ \mathbf{Q} &= \frac{\gamma\mathbf{C}+\delta\mathbf{D}}{\gamma+\delta}. \end{aligned} \tag{6.27}$$

Because of this property, the four center problem ($\mathbf{A}$, $\mathbf{B}$, $\mathbf{C}$, $\mathbf{D}$) in integral (6.20) can be simplified to a two-center problem ($\mathbf{P}$, $\mathbf{Q}$)

$$I = G_{AB}G_{CD} \iint e^{-\xi|\mathbf{r}_1-\mathbf{P}|^2} f(|\mathbf{r}_1-\mathbf{r}_2|) e^{-\eta|\mathbf{r}_2-\mathbf{Q}|^2} d\mathbf{r}_1 d\mathbf{r}_2. \tag{6.28}$$

Replacing the three factors of the integrand in Eq. (6.28),

$$e^{-\xi|\mathbf{r}_1-\mathbf{P}|^2} = (2\pi)^{-3}\int\left(\frac{\pi}{\xi}\right)^{3/2} e^{-\mathbf{k}_1^2/4\xi}e^{i\mathbf{k}_1\cdot(\mathbf{r}_1-\mathbf{P})}d\mathbf{k}_1, \tag{6.29}$$

$$f(|\mathbf{r}_1-\mathbf{r}_2|) = (2\pi)^{-3}\int\tilde{f}(\mathbf{k}_2)e^{i\mathbf{k}_2}\cdot(\mathbf{r}_1-\mathbf{r}_2)d\mathbf{k}_2, \tag{6.30}$$

$$e^{-\eta|\mathbf{r}_2-\mathbf{Q}|^2} = (2\pi)^{-3}\int\left(\frac{\pi}{\eta}\right)^{3/2} e^{-\mathbf{k}_3^2/4\xi}e^{i\mathbf{k}_3\cdot(\mathbf{r}_1-\mathbf{Q})}d\mathbf{k}_3, \tag{6.31}$$

substituting (6.29)–(6.31) into (6.28) and integrating over $\mathbf{r}_1$, $\mathbf{r}_2$, $\mathbf{k}_1$, and $\mathbf{k}_3$, Eq. (6.20) becomes a simple integral

$$\begin{aligned} I &= \frac{G_{AB}G_{CD}}{8(\xi\eta)^{3/2}}\int e^{-\frac{k_2^2(\xi+\eta)}{4\xi\eta}}e^{-i\mathbf{k_2}\cdot\mathbf{R}}\tilde{f}(k_2)d\mathbf{k}_2 \\ &= \frac{\pi G_{AB}G_{CD}}{2(\xi\eta)^{3/2}R^3}\int_0^\infty u\sin u e^{-u^2/4T}\tilde{f}(u/R)du, \end{aligned} \tag{6.32}$$

where

$$\begin{aligned} T &= \theta^2R^2 \\ \theta^2 &= \xi\eta/(\xi+\eta) \\ \mathbf{R} &= \mathbf{Q}-\mathbf{P}. \end{aligned} \tag{6.33}$$

For the overlap integral, we obtain

$$I^{overlap} = \left(\frac{\pi}{\alpha+\gamma}\right)^{3/2} e^{-\alpha\gamma|\mathbf{A}-\mathbf{C}|^2/(\alpha+\gamma)}. \tag{6.34}$$

The kinetic-energy integral is connected to the overlap integral by

$$\begin{aligned} I^{kinetic} &= \int e^{-\alpha|\mathbf{r}-\mathbf{A}|^2}\left(-\frac{1}{2}\nabla_{\mathbf{r}}^2\right)e^{-\gamma|\mathbf{r}-\mathbf{C}|^2}d\mathbf{r} \\ &= -\frac{1}{2}\nabla_{\mathbf{C}}^2\int e^{-\alpha|\mathbf{r}-\mathbf{A}|^2}e^{-\gamma|\mathbf{r}-\mathbf{C}|^2}d\mathbf{r} \\ &= -\frac{1}{2}\nabla_{\mathbf{C}}^2 I^{overlap} \\ &= \frac{3\alpha\gamma}{\alpha+\gamma}\left(\frac{\pi}{\alpha+\gamma}\right)^{3/2} e^{-\alpha\gamma|\mathbf{A}-\mathbf{C}|^2/(\alpha+\gamma)}. \end{aligned} \tag{6.35}$$

With $f(|\mathbf{r}_1-\mathbf{r}_2|) = \frac{1}{|\mathbf{r}_1-\mathbf{r}_2|}$, the result for the electron-electron repulsion integral is

$$I^{EE} = G_{AB}G_{CD}\frac{2\pi^{5/2}}{\xi\eta(\xi+\eta)^{1/2}}F_0^{EE}(T) \tag{6.36}$$

$$F_0^{EE}(T) = \int_0^1 e^{-Tu^2}du. \tag{6.37}$$

This one dimensional integral (6.37) can be evaluated very efficiently using the GSL integration library [230]. For the nuclear attraction integral in Eq. (6.24), we immediately obtain

$$I^{NE} = G_{AB}\frac{2\pi}{\xi^{3/2}}F_0^{EE}(T). \tag{6.38}$$

6.3.2 Recursion relation for general primitive Gaussian basis integrals

All the integrals presented so far are for primitive Gaussian basis functions with zero angular momentum. For Gaussian basis functions with higher angular momentum, their integrals can be obtained from those for the primitive s-Gaussian basis function using recursion relationship. Before we the introduce the actual recursion relationship, it is useful to look at a simplified notation [229]. In Eq. (6.19), a general two-electron integral over the two electron operator $f(|\mathbf{r}_1 - \mathbf{r}_2|)$ is given. Such an equation defines an inner product between two functions

$$(\mathbf{ab}| = \phi_a(\mathbf{r}_1)\phi_b(\mathbf{r}_1) \tag{6.39}$$

$$|\mathbf{cd}) = \phi_c(\mathbf{r}_2)\phi_d(\mathbf{r}_2). \tag{6.40}$$

using the Dirac notation, where $(\mathbf{ab}|$ and $|\mathbf{cd})$ are referred as "bra" and "ket", respectively [229], and $(\mathbf{ab}|\mathbf{cd})$ is referred as "braket". It is helpful to generalize Eq. (6.39) and Eq. (6.40) to derive the recursion relation. Though the generalized form is more complicated, it should be kept in mind that bras and kets here are simply functions of the positions of electron 1 and 2, respectively. The generalized primitive bra is given by

$$(\mathbf{abp}| = D_A D_B e^{-\alpha(\mathbf{r}-\mathbf{A})^2} e^{-\beta(\mathbf{r}-\mathbf{B})^2} \Pi_{i=x,y,z}(i - A_i)^{a_i}(i - B_i)^{b_i}\xi^{p_i/2}H_{p_i}[\xi^{1/2}(i - P_i)], \tag{6.41}$$

where H_n is the nth Hermite polynomial defined as

$$\begin{aligned} H_0(x) &= 1 \\ H_1(x) &= 2x \\ H_{n+1}(x) &= 2xH_n(x) - 2nH_{n-1}(x). \end{aligned} \tag{6.42}$$

The three symbols **abp** in the bra represent the primitive Gaussian basis $\chi_a(\mathbf{r})$ centered at position $\mathbf{A}$, Gaussian basis $\chi_b(\mathbf{r})$ centered at position $\mathbf{B}$, and the Hermite function centered at position $\mathbf{P}$.

Similar general form can be given for ket. Then, the general primitive integral we are concerned with can be written as

$$\begin{aligned}(\mathbf{ab}|\mathbf{cd}) &= (\mathbf{ab0}|\mathbf{cd0}) \\ &= \iint e^{-\alpha(\mathbf{r}_1-\mathbf{A})^2} e^{-\beta(\mathbf{r}_1-\mathbf{B})^2} \Pi_{i=x_1,y_1,z_1}(i-A_i)^{a_i}(i-B_i)^{b_i}\cdot \\ &\quad f(|\mathbf{r}_1-\mathbf{r}_2|)\cdot e^{-\alpha(\mathbf{r}_2-\mathbf{C})^2} e^{-\beta(\mathbf{r}_2-\mathbf{D})^2} \Pi_{i=x_2,y_2,z_2}(i-C_i)^{c_i}(i-D_i)^{d_i} d\mathbf{r}_1 d\mathbf{r}_2, \end{aligned} \tag{6.43}$$

where we dropped the coefficients D_A, D_B, D_C, and D_D, which can be easily added back later. Applying the properties of Hermite polynomials in Eq. (6.42), there exists a three-term relationship

$$((\mathbf{a}+\mathbf{1}_i)\mathbf{bp}| = p_i\,(\mathbf{ab}(\mathbf{p}-\mathbf{1}_i)| + (P_i-A_i)\,(\mathbf{abp}| + (2\xi)^{-1}\,(\mathbf{ab}(\mathbf{p}+\mathbf{1}_i)|\,, \tag{6.44}$$

where $\mathbf{1}_i$ is a unit index vector with a non-zero element 1 in direction i (i can be x, y, or z). Thus, $((\mathbf{a}+\mathbf{1}_i)\mathbf{bp}|$ means that the angular momentum in Eq. (6.41) at direction i becomes a_i+1, while others remain unchanged. Similar three-term relationships also exist for the ket. Such three-term relationship for **a**, **b**, **c**, and **d** can be applied recursively until all of the angular moments become zero. Then, the integral (6.43) is finally converted into the evaluation of a serials of

$$\begin{aligned}(\mathbf{00p}|\mathbf{00q}) = &\iint e^{-\alpha(\mathbf{r}_1-A)^2} e^{-\alpha(\mathbf{r}_1-B)^2} \Pi_{i=x_1,y_1,z_1} \xi^{p_i/2} H_{p_i}[\xi^{1/2}(i-P_i)]\cdot \\ &f(|\mathbf{r}_1-\mathbf{r}_2|)\cdot e^{-\alpha(\mathbf{r}_1-C)^2} e^{-\alpha(\mathbf{r}_1-D)^2} \Pi_{i=x_2,y_2,z_2} \xi^{q_i/2} H_{q_i}[\xi^{1/2}(i-Q_i)] d\mathbf{r}_1 d\mathbf{r}_2 \\ =&G_{AB}G_{CD} \iint e^{-\xi|\mathbf{r}_1-\mathbf{P}|^2} \Pi_{i=x_1,y_1,z_1} \xi^{p_i/2} H_{p_i}[\xi^{1/2}(i-P_i)] f(|\mathbf{r}_1-\mathbf{r}_2|) \\ &e^{-\eta|\mathbf{r}_2-\mathbf{Q}|^2} \Pi_{i=x_2,y_2,z_2} \xi^{q_i/2} H_{q_i}[\xi^{1/2}(i-Q_i)] d\mathbf{r}_1 d\mathbf{r}_2. \end{aligned} \tag{6.45}$$

Notice that Hermite polynomials satisfy

$$\begin{aligned} e^{-\xi(\mathbf{r}-\mathbf{p})^2} \Pi_{i=x,y,z} \xi^{r_i/2} H_{r_i}(\xi^{1/2}(i-P_i)) &= (-1)^r \Pi_{i=x,y,z} \frac{d^{r_i}}{d_i^{r_i}} e^{-\xi(i-P_i)^2} \\ &= \Pi_{i=x,y,z} \frac{d^{r_i}}{dP_i^{r_i}} e^{-\xi(i-P_i)^2}. \end{aligned} \tag{6.46}$$

so Eq. (6.45) can be simplified as

$$(\mathbf{00p}|\mathbf{00q}) = \Pi_{i=x,y,z} \frac{d^{p_i}}{d^{p_i}P_i} \frac{d^{q_i}}{d^{q_i}Q_i} G_{AB}G_{CD} \iint e^{-\xi|\mathbf{r}_1-\mathbf{P}|^2} f(|\mathbf{r}_1-\mathbf{r}_2|) e^{-\eta|\mathbf{r}_2-\mathbf{Q}|^2} d\mathbf{r}_1 d\mathbf{r}_2, \tag{6.47}$$

where the integral part is exactly the fundamental integral we considered before. So, we can immediately get the final form of the integral as

$$(\mathbf{00p}|\mathbf{00q}) = \Pi_{i=x,y,z} \frac{d^{p_i}}{d^{p_i}P_i} \frac{d^{q_i}}{d^{q_i}Q_i} \frac{G_{AB}G_{CD}}{8(\xi\eta)^{3/2}} \int e^{-\frac{k_2^2(\xi+\eta)}{4\xi\eta}} e^{-i\mathbf{k_2}\cdot\mathbf{R}} f(k_2) d\mathbf{k}_2 \tag{6.48}$$

$$= (-1)^q \Pi_{i=x,y,z} \frac{d^{s_i}}{d^{s_i}R_i} \frac{G_{AB}G_{CD}}{8(\xi\eta)^{3/2}} \int e^{-\frac{k_2^2(\xi+\eta)}{4\xi\eta}} e^{-i\mathbf{k_2}\cdot\mathbf{R}} f(k_2) d\mathbf{k}_2, \tag{6.49}$$

where we combined the two derivatives using the fact that $\mathbf{R} = \mathbf{P} - \mathbf{Q}$ and $s_i = p_i + q_i$. To simplify the notation, we denote the last equation (6.49) as (**S**). For the overlap integral, we have

$$(\mathbf{S})^{overlap} = \left[\frac{\pi}{\xi+\eta}\right]^{3/2} H_{r_x}(\theta R_x) H_{r_y}(\theta R_y) H_{r_z}(\theta R_z) e^{-\theta R^2} \theta^r. \tag{6.50}$$

To avoid the derivative evaluation in Eq. (6.49), we further define

$$(\mathbf{S})_m^{overlap} = \left[\frac{\pi}{\xi+\eta}\right]^{3/2} \theta^r (2\theta^2)^m H_{r_x}(\theta R_x) H_{r_y}(\theta R_y) H_{r_z}(\theta R_z) e^{-\theta R^2}. \tag{6.51}$$

Then we can obtain a two-term recursion relationship for $(\mathbf{S})_m^{overlap}$ as

$$(\mathbf{S})_m^{overlap} = R_i(\mathbf{S} - \mathbf{1}_i)_{m+1}^{overlap} - (s_i - 1)(\mathbf{S} - \mathbf{2}_i)_{m+1}^{overlap}. \tag{6.52}$$

Similar two-term recursion relationships can be found for the other type of integrals as well. So far, we can summarize the algorithm using the calculation of Gaussian basis set as

$$(\mathbf{ab}|\mathbf{cd}) = (\mathbf{ab0}|\mathbf{cd0}) \Rightarrow (\mathbf{00p}|\mathbf{00q}) \Rightarrow (\mathbf{S}) \Rightarrow (\mathbf{0})_m. \tag{6.53}$$

Instead of implementing the recursion function directly to evaluate each recursion relationship, it is implemented with a non-recursive function to avoid extra time caused during calling recursive function and stack overflow. We can further summarize the strategy to calculate the Gaussian basis integrals as follows:

(1) Determine the largest m according to the momentum index of integral (**ab**|**cd**).

(2) Form a table with elements $[0]^i$ for i=0, ..., m.

(3) Calculate (**S**) via recursion relationship (6.52).

(4) Form table $(\mathbf{00p}|\mathbf{00q}) = (-1)^q(\mathbf{S})$ for p=0,1,...p, and q=0,1,...,q.

(5) Calculate $(\mathbf{ab}|\mathbf{cd})$ via recursion relationship (6.44).

The evaluation of Gaussian basis set integral in this form is very efficient and is implemented as a class GaussianBasisEval in our program (see Fig. 6.2).

6.4 Technical details

The main program structure is shown in Fig. 6.2. The IO class is a class that can help

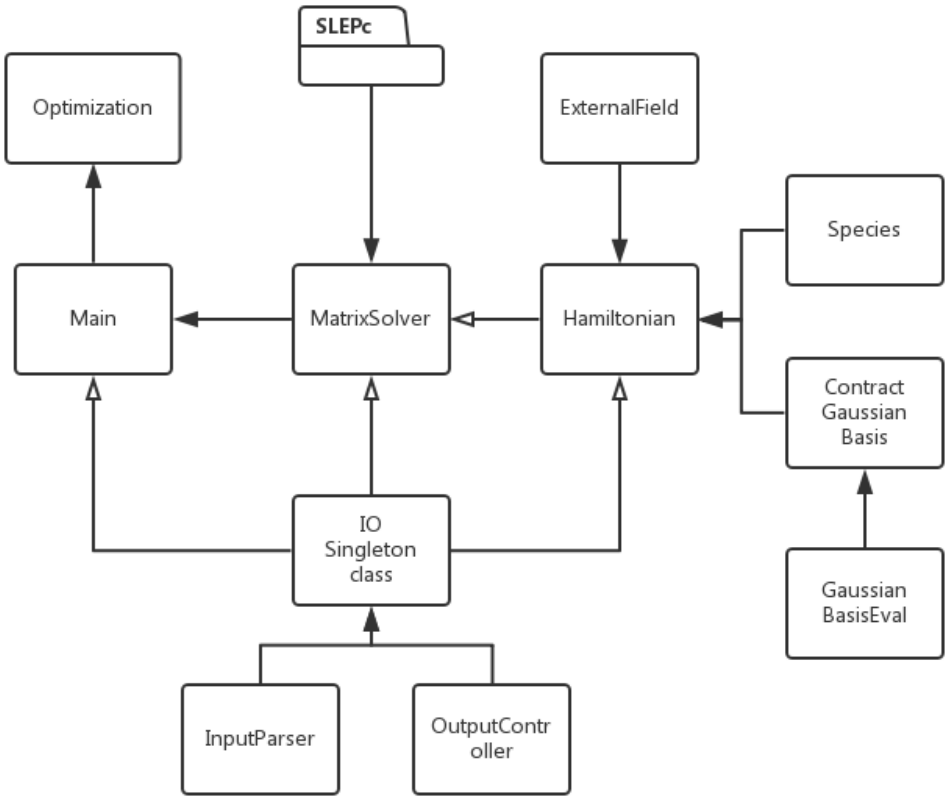

Figure 6.2: Diagram of the Floquet program representing the relationship between classes.

other classes to parse the input and output without worrying about race condition in parallel computation. The GaussianBasisEval class is used to calculate the Gaussian integral in Eq. (6.20) while the ContractGaussianBasis class which is built on the top of GaussianBasisEval is used to

calculate the matrix element with contracted Gaussian basis sets. The main task of Hamiltonian class is to calculate the Floquet matrix elements in Eq. (6.4). Parallelization with MPI is applied to speedup the matrix element calculation process. After the matrix is created, EigenSolver class will check the matrix property and choose an appropriate eigensolver to solve the matrix with parallel package SLEPc [222]. Everything except the optimization class is written in C++. The optimization module is implemented with Python since many optimization packages are available for Python. The optimization process will generate an input file and read the output from the program step by step to find the optimal Gaussian basis sets.

Based on our test calculations, there are several things to be taken into consideration:

(1) Because of the periodic property of Floquet states in Eq. (6.3), we can no longer select Floquet states based on the order of their energies. One way to avoid such problem is to confine the solution $\varepsilon \in (-\omega/2, \omega/2]$ but it still does not clarify from which states each Floquet state is formed, which is an obstacle for the automatic optimization process. One possible solution is to first calculate all bound states of interest without external laser field in which case there is no periodic quasienergy problem and then project Floquet states $\Phi_\lambda(\mathbf{r}, t)$ to the bound state $\psi_b(\mathbf{r})$ of interested via Eq. (6.54) and select the Floquet state with highest projection value

$$\int_o^T dt \int d^3r |\psi_b(\mathbf{r})\Phi_f(t, \mathbf{r})|^2 \tag{6.54}$$

(2) We also find that the imaginary part of quasienergy without external field using rotated complex Gaussian basis sets has a non-zero value. Such phenomena arise from the incompleteness of basis sets and its effect can be reduced by increasing the basis sets as shown in [219, 231]. However, for a Gaussian basis set, it is not easy to improve the accuracy of bound states and the best ground state energy for hydrogen atom we got is -0.4998. Because of this problem, we subtract the imaginary part of eigenvalue ε in laser field by the imaginary part of eigenvalue ε_o with zero-external field. Although the results for the cases

in this thesis are accurate, the procedure should be dealt with carefully for other situations, especially for processes at high intensity.

6.5 Optimization for complex Gaussian basis

The complex coordinate rotation is quite straight forward in numerical calculations. Chu and Telnov have applied it to study multiphoton ionization, dissociation, etc. extensively for one- and two-color laser field [182]. However, so far it is only applied for problems in 1 or 2 dimensions. For the calculation of large molecules with grid method in 3D, it is even impossible with current super computer because the matrix to solve is very huge. For example, for simulation box with 200 grid points in each dimension and a 10 photon block, the matrix to be solved is 8×10^7 by 8×10^7, which is even impossible to store directly in the super computer. Especially, the computational costs will be huge during self-consistent calculation after applying it to DFT. With complex basis set, it is possible to get high precision results with relatively small basis. For example, a basis set with 21 Gaussian functions is applied to calculate the photoionization cross sections from N_2 [220] and it is even possible to obtain accurate results for photoionization cross sections with only one or two complex Gaussian function as shown in [232].

With complex coordinate rotation technique, eigenvalues of resonances can be found since they do not change if the rotation angle reaches a critical value. The complex Gaussian basis is usually obtained by rotating their exponent $\alpha e^{-i\theta}$ directly. Since complex basis sets are obtained by rotating real Gaussian basis sets, according to the equivalence between complex coordinate rotation and complex basis sets in Eq. (6.16), the eigenvalue of resonance states can be stationary after some critical rotation angle. For a simple system, with large enough basis, it is possible by optimizing θ to find the stationary angle, at which the quasienergy does not change with rotation angle anymore. However, for complex systems, usually both α and θ have to be optimized. An efficient optimization process for the exponent α is very important for the application of such technique. For the optimization object function, the natural choice is the quasienergy, which has been used in [233, 234, 235, 236]; while optimization on polarizability is applied in [220, 237, 232].

As for the optimization for the Gaussian exponent α, there is still no common choice yet, which therefore is the most difficult part. A geometrical series for Gaussian exponent α was chosen in [236, 231]. Sometimes, the value of α is chosen such that a complex eigenvalue with real parts in the expected energy range is guaranteed [220]. And recently, Matsuzaki et al. proposed to fit Gaussian functions to Slater function, where the exponent of the Slater function is determined by the energy of ionized electron [238].

During past decades, various real Gaussian basis sets are proposed to describe the bound states and yield relatively high precision for stationary calculations. However, there is still no systematic efficient way to find precise Gaussian basis sets describing continuum states in a laser field. This is because firstly, the basis set parameters strongly depend on the laser parameters, especially the laser frequency. Secondly, unlike in the stationary case, in which basis parameters for bound states can be optimized via minimization of bound state energy, in the laser field, Floquet states only satisfy a stationary condition which means $\frac{\partial \varepsilon}{\partial \alpha_i} = 0$ where ε is quasienergy and α_i are parameters to be optimized. This makes the optimization process more difficult than just minimizing the state energy. Thirdly, the optimization problem is a non-convex problem which makes the process rather difficult.

6.5.1 Optimization algorithm

In our calculations, we take real contracted Gaussian basis sets to describe the bound states and add several additional complex basis sets to describe the continuum wavepackets. Since the Gaussian basis sets are not complete, the stationary property usually only holds for a small range of angles, typically around 30^o. So, one way to optimize the exponents of Gaussian basis set is to calculate the eigenvalue for each angle from 0^o to 80^o degree and study the trajectory to see if a stationary point is found. If no stationary point is present, then one changes the exponents of Gaussian basis set and repeats the above processes until a stationary point is found.

Such optimization is not very efficient, because we have to compute the eigenvalues at each angle from 0^o to 80^o to see if the stationary property is present with the trial exponents of Gaussian

basis set. In such process it is difficult to implement an auto-optimization process since we cannot easily formulate a objective function for such method. Alternatively, we can assume that the stationary points always occurs around 30^o which is a good assumption because the critical angle reported in most papers is lower than 30^o. In this way we only need to perform calculations around 30^o without a full calculation.

To develop an objective function for optimization, we require that the first derivative of the eigenvalue with respect to rotation angle is zero at 30^o, because the eigenvalue at stationary point (assumed to be 30^o) is independent of the rotation angle. According to our calculations, the real part of eigenvalue strongly depends on the real Gaussian basis sets which are already known and barely change for the complex Gaussian basis sets. Therefore, we only require the imaginary eigenvalue $\mathrm{Im}(\varepsilon)$ to be stationary.

The stationary property is not guaranteed by the condition for the first derivative only. As more higher derivatives are zero as well, as better the conclusion that the stationary condition is achieved. To save computation time, we choose to optimize the first and second derivatives of imaginary eigenvalue with respect to the rotation angle only. In our program, the first derivative is calculated with the spline interpolation function. During the interpolation process, we set the boundary condition such that the second derivative at the ends of interpolated points are zero. We have chosen our objective function:

$$\left[\left(\frac{\partial \mathrm{Im}(\varepsilon)}{\partial \theta}\right)^2 + C\left(\frac{\partial^2 \mathrm{Im}(\varepsilon)}{\partial \theta^2}\right)^2\right]_{\theta=30^o}, \tag{6.55}$$

where we added C to adjust the relative weight between the first and second derivatives. Both first and second derivative are squared to convert the stationary problem to a minimization problem. The optimization process will stop when the value of Eq. (6.55) is less than a critical value. However, the ionization rate $\gamma = -2\mathrm{Im}(\varepsilon)$ is strongly influenced by the laser intensity and can vary by several orders of magnitude. Thus, the optimized value of Eq. (6.55) can also vary dramatically and the critical value to stop optimization process need to be changed accordingly for different

systems and laser intensities. Instead of doing this, it is better to optimize the relative value:

$$\frac{1}{(\mathrm{Im}(\varepsilon))^2}\left[\left(\frac{\partial \mathrm{Im}(\varepsilon)}{\partial\theta}\right)^2 + C\left(\frac{\partial^2 \mathrm{Im}(\varepsilon)}{\partial\theta^2}\right)^2\right]_{\theta=30^o}, \tag{6.56}$$

which does not depend strongly on the laser intensity and we do not have to change the criterion for optimization for different intensities.

The optimization algorithm applied is a sequential penalty derivative-free method for non-linear constrained optimization [239], which is provided in Python package pyOpt [240]. The optimization problem is a highly non-convex problem and thus the final optimal result depends on the initial values of exponents of Gaussian basis sets. To overcome such an initial value problem we followed the idea of R. Matsuzaki et al. [238], who used Slater basis sets in their calculation. The radial part of the Slater function has the form as

$$R(r) = Nr^{n-1}e^{-sr}. \tag{6.57}$$

With complex exponent s, the behavior of the Slater function is more similar to a plane wave e^{ikr} than a Gaussian function because the oscillating frequency of Slater function only depends on s while for Gaussian function the oscillating frequency increases with r. Since the ionized wavepacket can be approximated by a plane wave e^{ikr}, we can choose Slater function to represent such a plane wave by setting $s = k = \sqrt{2E}$. We also want to find a similar connection between the energy of the ionized wavepacket and exponents of Gaussian basis set. Actually, there exists a integral transformation between Slater function and Gaussian function

$$e^{-sr} = \frac{s}{2\sqrt{\pi}}\int_0^\infty \alpha^{-3/2}e^{-s^2/4\alpha}e^{-\alpha r^2}d\alpha, \tag{6.58}$$

which can be interpreted such that a Slater function e^{-sr} can be written as a sum of Gaussian functions $e^{-\alpha r^2}$ with coefficient $C = \frac{s}{2\sqrt{(\pi)}}\alpha^{3/2}e^{-s^2/4\alpha}$. The coefficient C constraints the range of exponents α, and thus it tells us for certain value s, where the value of the exponents $\{\alpha_i\}$ of the Gaussian basis sets should be. Therefore, instead of fitting Slater function with Gaussian basis set as in [238], we assign the initial value of $\{\alpha_i\}$ according to C. To prove that this strategy is useful, we have done several calculations and the optimized value of $\{\alpha_i\}$ is shown as vertical line in Fig.

6.3. The solid curve line represents the normalized coefficient C for different ionization energy E_k while the other two dashed curves are those for electron energy of $2E_k$ and $E_k/2$, respectively. Calculations are performed for H atom in laser field of frequency ω=0.6 (left), 1.0 (middle), and 2.0 (right). From the calculation, the exponents $\{\alpha_i\}$ of Gaussian basis sets do fall in the range

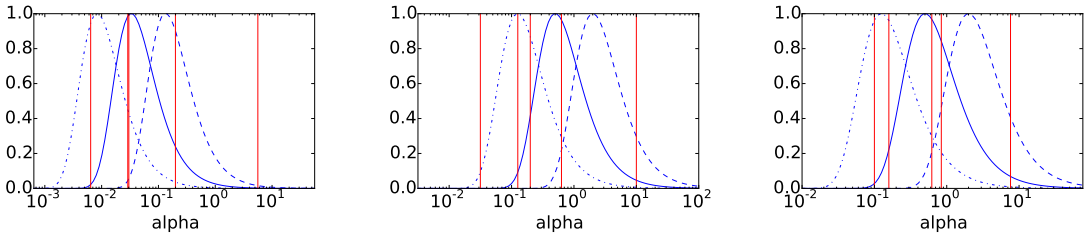

Figure 6.3: Distribution of exponents α of Gaussian basis sets (red vertical line) after optimization for the H atom in a laser field with $\omega = 0.6$ (left), $\omega = 1.0$ (middle), $\omega = 2.0$ (right). The solid blue curve is the normalized coefficient $\alpha^{-3/2}e^{-s^2/4\alpha}$ for $s = \sqrt{2E_k}$ and the other two dashed blue curves are for electron energy of $2E_k$ and E_k.

defined by the coefficient C for several very different laser frequency. We, therefore, choose values uniformly distributed in the range defined by C as the initial optimization value.

6.6 Results and discussion

6.6.1 One photon ionization of H atom

We first calculated the one-photon ionization of the hydrogen atom at intensity 4.387×10^{13} W/cm^2 with laser frequency $\omega = 0.6$ a.u. The real Gaussian basis set used is 6-31++G**, which represents the ground s-state well. For one-photon ionization, no higher bound states are required to get accurate results. Complex Gaussian basis sets including both s and p states are added to represent the continuum states. P states are necessary since the final angular momentum is 1 after one photon transition from s state. The complex s state is also necessary to get good stationary result based on our calculations. s and p Gaussian basis sets share the same exponents α. For the test, we first tried complex Gaussian basis sets with 3 and 5 states. The initial value is assigned according to the coefficient C with $E_k = 0.1$ (energy of ionized electron is $E_k = \omega - I_p$). The number of Floquet block n is also tested for convergence. For this one-photon transition and

laser intensity 4.387×10^{13} W/cm^2, n=0, 1 is sufficient to achieve a converged result. For higher intensity, more Floquet blocks are needed as shown later.

After optimization, we calculated the eigenvalues with the optimized exponents $\{\alpha_i\}$ for the rotation angle from 0^o to 80^o. The results are shown in Fig. 6.4, where the top two panels are

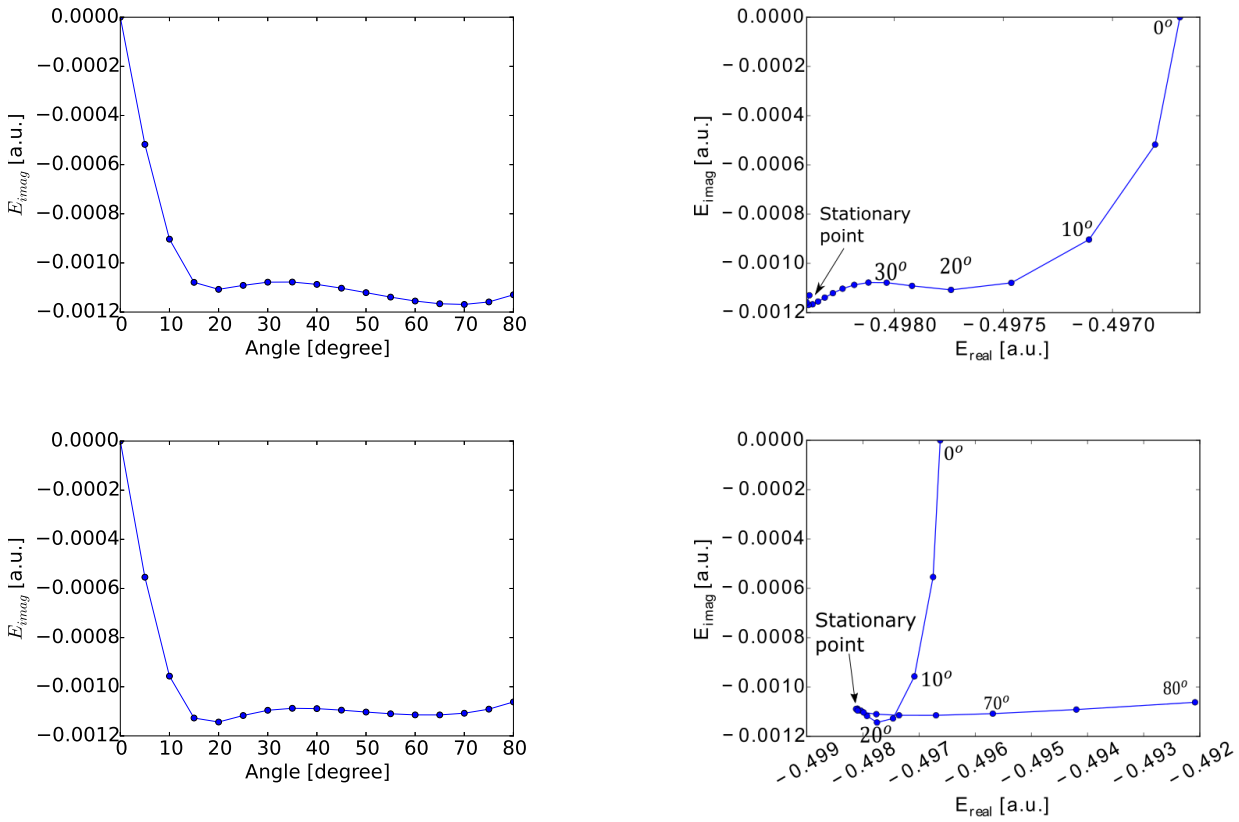

Figure 6.4: Quasienergy trajectory of H atom in a laser field at intensity of 4.387×10^{13} W/cm^2 with frequency $\omega = 0.6$. Results in the top two panels are for 3-complex Gaussian basis sets while those in the bottom row are for 5-Gaussian basis sets. Figures on the left show the imaginary part of quasienergy as a function of the rotation angle θ and panels on the right show the trajectory of the quasienergy. A stationary point is found with $\varepsilon = -0.498 - 0.00109i$ a.u..

results obtained with 3 complex Gaussian basis sets and the bottom two panels are results obtained with 5 complex Gaussian basis sets. The Figures on the left show the imaginary part of quasienergy as function of rotation angle. In both cases, we get a relatively flat curve around 30^o which means both first and second derivatives are close to zero as expected. On the other hand, although we only minimize the objective function at 30^o, the imaginary part of quasienergy is actually unchanged

	our results	reference values
$\omega = 0.6$,$F = 1 \times 10^{-4}$	0.1354	$0.1378^{(a)}$
$\omega = 0.6$, $F = 7.08 \times 10^{-4}$	0.1356	$0.1377^{(b)}$
$\omega = 0.6$, $F = 0.05$	0.1399	$0.1384^{(a)}$
$\omega = 1.0$, $F = 7.08 \times 10^{-4}$	0.0338	$0.0333^{(b)}$
$\omega = 2.0$, $F = 1 \times 10^{-4}$	0.0046	$0.0044^{(a)}$

Table 6.1: Results for one-photon ionization cross sections compared to those from the literature. F is root mean square of laser electric field in atomic units. All the calculations above are performed for $n = 0, 1$ except for $F = 0.05$, in which n is $-1, 0, 1, 2$ due to the strong coupling at high intensity. The superscripts of the reference values: (a) stand for [241] and (b) for [231]

for a much wider range of rotation angle. The two panels on the right show the trajectory of the quasienergy. In both cases, there is an angle, around which the trajectory of the quasienergy does not change too much and is trapped, which is identified as stationary point, as indicated in the Fig. 6.4(right). The stationary point for the 3 complex Gaussian basis sets is around 70^o while for the 5 complex Gaussian basis sets it is around 30^o. From the trajectory plot, the trajectory of 5 complex Gaussian basis sets has a better stationary quality than the other case. Therefore, in the following calculation, we will use 5 Gaussian basis sets.

To compare the results with other papers [241, 231], we calculated the one-photon cross sections via the imaginary part of the quasienergy. For a M photon process, the cross section can be calculated via

$$\sigma_M = \frac{\hbar \Gamma \omega}{I^M}, \tag{6.59}$$

where Γ_ω is the ionization rate and I is the laser intensity. The one-photon cross sections at different intensities and frequencies are calculated and illustrated in the Table 6.1. Our results obtained with only 5 complex Gaussian basis sets (each set includes both s and p components) are in good agreement with those of other papers. The exponents $\{\alpha_i\}$ for different frequencies is given in Table 6.2. We find that the optimized complex Gaussian basis sets do not depend much on the intensity of the laser field but only strongly depend on the frequency. For example, the results for three different intensities but at the frequency $\omega = 0.6$ are obtained with the same complex Gaussian basis sets. for a broad range of intensities from 7×10^8 W/cm^2 to 1.8×10^{14} W/cm^2, keeping the

$\omega = 0.6$	$\omega = 1.0$	$\omega = 2.0$
5.623413	10.00000	7.617912
0.199059	0.630957	0.841466
0.030132	0.199526	0.621906
0.028864	0.125893	0.158489
0.006410	0.031623	0.100000

Table 6.2: The exponents of complex Gaussian basis sets for different laser frequencies. These basis sets are tested for the range of laser intensity from 7×10^8 W/cm to 1.8×10^{14} W/cm^2.

excellent agreement with reference values. This is due to the fact that it is the laser frequency that determines the energy of ionized outgoing wavepackets. The trajectories of eigenvalues for all of this calculations are shown in Fig. 6.5. For all the cases, the stationary property around stationary point is very strong, demonstrating the validity of our calculations.

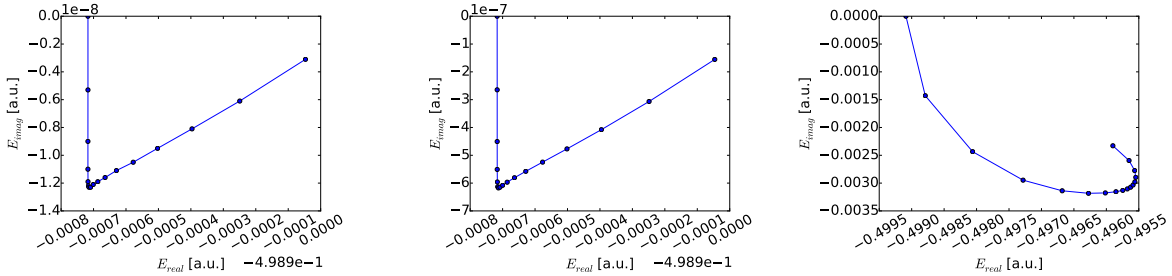

(a) $F = 1 \times 10^{-4} a.u., \omega = 0.6 a.u.$ (b) $F = 7.08 \times 10^{-4} a.u., \omega = 0.6 a.u.$ (c) $F = 0.05 a.u., \omega = 0.6 a.u.$

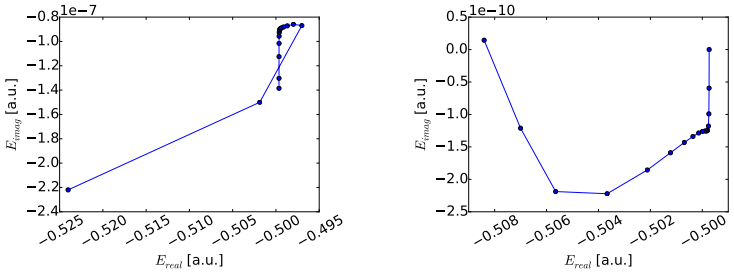

(d) $F = 7.08 \times 10^{-4} a.u., \omega = 1.0 a.u.$ (e) $F = 1 \times 10^{-4} a.u., \omega = 2.0 a.u.$

Figure 6.5: Trajectory of quasienergy of H for different laser parameters. F is the mean square root of laser electric field.

The ionization rates obtained using this method are very accurate and the computation time is short. The ionization rate from numerical simulations is often obtained by applying a long laser

field with constant amplitude and then plot the time dependent population to obtain the slope as a function of time which is equal to the ionization rate. With the Floquet method, the optimization procedure for the one-photon ionization is very fast and typically optimization can be achieved within 10 minutes. Furthermore, since the continuum states depend on the energy of the ionized wavepacket, the optimization has to be done once only for a study as a function of laser intensity. The calculation of the ionization rate itself takes less than 1 second, which is very fast compared to numerical propagation method. On the other hand, Floquet method, also gives direct access to the Stark shift which is usually difficult to obtain with other methods.

6.6.2 Two photon ionization from H atom

While for the one-photon ionization, it is very easy to get the stationary value, the case of two photon ionization is more complicated. The complex Gaussian basis sets can be obtained through optimization process in the same way as for one photon ionization. The maximum angular momentum l should be 2 instead of 1 for this case. The bound states can be still represented with 6-31++G** Gaussian basis set. However, now further bound states are required since the two-photon ionization can go via intermediate states which are needed to be represented. Therefore, for the two-photon ionization case, we have to add more Gaussian basis sets to represent possible excited states and intermediate states.

For H atom, currently there are no real Gaussian basis sets for higher excited states available. Instead of just using five Gaussian basis sets as in the one photon case, we added 15 complex Gaussian basis sets including both s and d states during the optimization. The initial value for each basis is still assigned evenly in the range determined by coefficient C.

We calculated the two-photon ionization of H atom at a laser frequency $\omega = 0.3$ and intensity 4.3×10^{13} W/cm^2. After optimization, we calculated the eigenvalue for different rotation angle and the trajectory is plotted in Fig. 6.6. Compared to one photon ionization, the imaginary part of quasienergy is only flat for the angle between 30^o and 60^o. The stationary point can be found from the trajectory plot in Fig. 6.6(c). The optimized value of α is indicated by the vertical line, as

shown in Fig. 6.6(d).

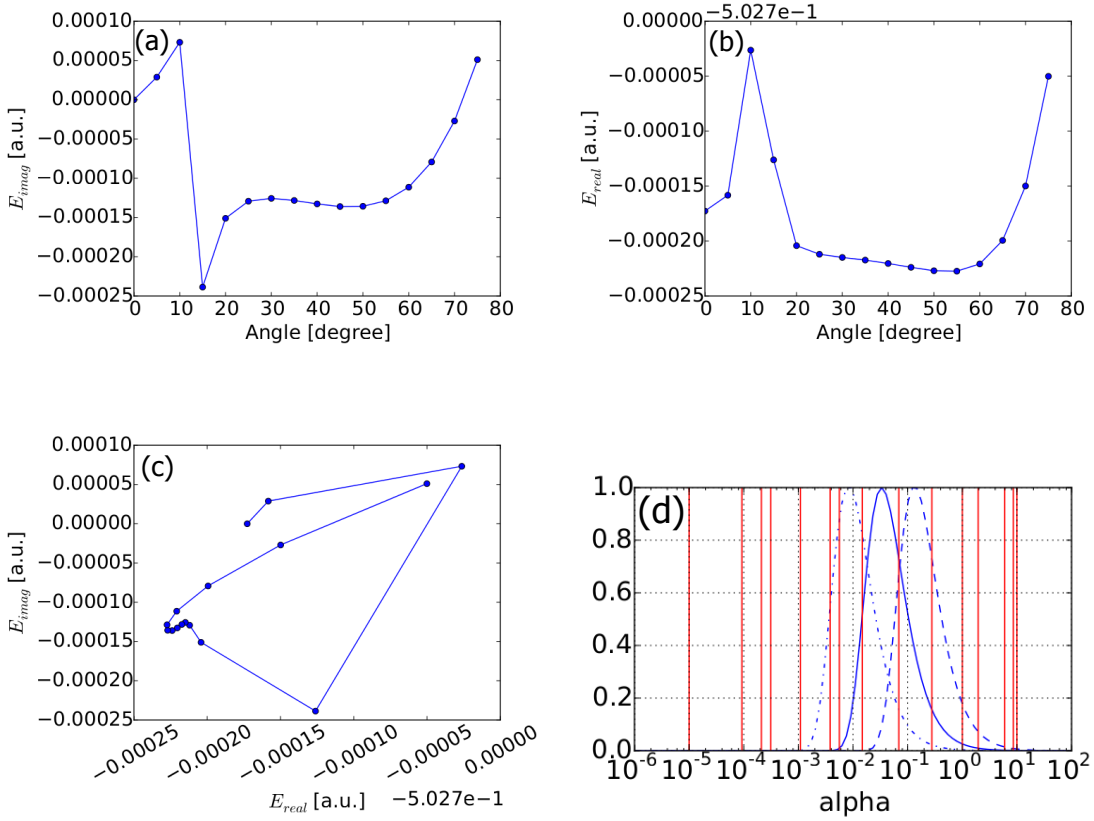

Figure 6.6: Trajectory of quasienergy (a-c) for two photon ionization from H atom in a laser field with $\omega = 0.3$ and $F = 0.025$ and the value of exponents of complex Gaussian basis after optimization are indicated by the vertical lines in (d).

Compared to the case of atom, for molecules, although the number of available Gaussian basis sets for each atom does not change, the total number of Gaussian basis sets increases with the number of atoms and thus these Gaussian basis sets can represent more states than in the atom case. Therefore, we do not need provide many complex Gaussian basis sets in the molecular case as we will illustrate it in the next subsection.

6.6.3 Two photon ionization from H_2^+

We have also applied our method to the simplest molecule H_2^+. We have used the same real Gaussian basis 6-31++G**, which represents the 1s, 2s, 2p, 3s and 3p state. For the continuum, 5

complex Gaussian basis sets including both s and p states centered on each atom are added. The complex Gaussian basis sets on the two H atom are the same.

To compare with other papers, we have performed calculations for laser intensity I=1.76 $\times$ 10^{13} W/cm^2 at different frequencies ω. After optimization, we obtain the stationary quasienergy and calculate the cross section via Eq. (6.59) with $M = 2$. The results are plotted (red dots) and compared to reference values (blue curve) in Fig. 6.7. Our results are in good agreement with the results reported in other papers [231, 242] over a broad range of frequencies even for the $2\sigma_u$ resonance corresponding to the first peak in the figure. Compared to the two-photon calculation

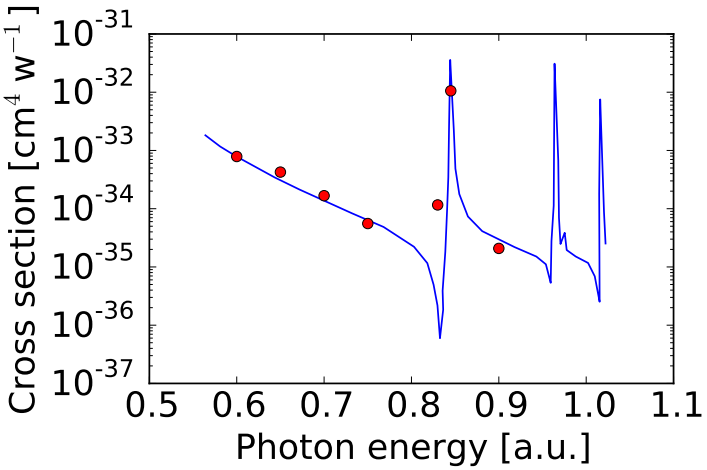

Figure 6.7: Cross section of two-photon ionization from H_2^+ at laser intensity I=1.76$\times 10^{13}$ W/cm^2. The solid curve is adapted from [209, 242] and the red dot is our calculations.

for H atom, we used the same real Gaussian basis set but here we only need 5 complex Gaussian basis sets because of more states can be represented by the Gaussian basis sets. This simple test implies that this Floquet method with Gaussian basis sets may work even for large molecules. The optimal values of exponents $\{\alpha_i\}$ of complex Gaussian basis sets in our calculation for H_2^+ are given in Table 6.3.

Table 6.3: Complex Gaussian exponents for two photon ionization

ω=0.6	ω=0.65	ω=0.7	ω=75	ω=0.83	ω=0.845	ω=0.9
7.02329e-1	6.45221e-1	6.45993e-1	1.53936e1	2.55236e1	2.46937e1	7.33636
4.09294e-2	4.09330e-2	4.09468e-2	6.02369	1.391903	1.07211	2.09922e-1
2.34079e-2	2.23400e-2	2.33864e-2	2.30414e-2	1.000000	9.95687e-1	2.98224e-1
8.35401e-4	1.84340e-3	5.20973e-3	4.54144e-3	7.71358e-2	8.08699e-2	8.73335e-2
7.91926e-4	2.08791e-4	5.67170e-5	1.18183e-4	7.29241e-4	7.29315e-4	9.47368e-4

6.7 Summary

We have shown that the application of a combination of real and complex Gaussian basis sets in the Floquet method can help efficiently compute accurate quasienergies over a broad range of laser intensities and frequencies. A very general optimization procedure to optimize complex Gaussian basis sets has been developed. Although the optimization problem is a non-convex problem and the optimization results depend on the initial value of the exponents of Gaussian basis sets, we find that it is still possible to get accurate results with initial values based on the energy of ionized wavepackets. The cross sections for one-photon and two-photon ionization for both H and H_2^+ are in agreement with those reported in literature. For multiphoton ionization, more basis sets will be needed for the excited and intermediate states. However, with the same available real Gaussian basis sets, more states can be represented for molecules than for atoms by the same Gaussian basis sets. Although we only applied it to one-electron case, it is straightforward to move to multielectron system by applying such technique in the Kohn-Sham equations directly in the future.

Chapter 7

Summary

In this thesis, we have systematically studied multielectron effects in high-order harmonic generation, ionization, and nonadibatic electron localization in the interaction between molecules and an intense laser field by applying time-dependent density-functional theory to solve the multielectron Schrödinger equation. The results of our numerical simulations and theoretical analysis showed that, in particular, the field-induced coupling between different molecular orbitals can have a strong influence on these fundamental processes.

We first analyzed multielectron effects in the high-order harmonic generation spectra in Chapter 3. We found that the laser induced coupling can lead to fractional harmonics in the form of Mollow sidebands over the whole spectra of harmonics and modification of the traditional three-step model for the HHG process. Such phenomenon has been analyzed in detail for the case of N_2^+ but is found to appear in general for other open-shell molecules as well. We further analyzed experimental data for the ellipticity of harmonics from N_2 and CO_2. Our multielectron simulation results are in good agreement with experimental results. By analyzing the response from all valence orbitals to the ellipticity pattern, we have found that contributions from inner valence orbitals play a significant role in the HHG process for molecules, which indicates a breakdown of the single-active-electron model.

In Chapter 4 we studied the coupling effects on ionization which is another important strong-field process. Our results show that the laser-induced coupling between inner valence orbital and HOMO can significantly enhance the ionization from inner shell orbitals. These results do not

only provide another indication of the importance of multielectron effects in strong-field interaction with molecules, but they may also explain the population inversion in ions, recently observed in filamentation experiments.

Since electron localization in molecules can strongly modify the ionization dynamics, we have further studied the effects of the field-induced coupling of states on the electron dynamics in molecules. Analysis of results presented in Chapter 5 show that two competing processes, in which the expected oscillation of the electron density with the change of external field is superimposed by a dynamics due to the Rabi flopping of the coupled states, lead a strong nonadiabatic dynamics. The mechanism and the control of the two competing processes via the parameters of the field are analyzed.

In Chapter 6, we have introduced a new intense-field method using the Floquet theorem and complex Gaussian basis sets. Floquet theorem is applied to transform the time-dependent Schrödinger equation into a set of time-independent equations. Complex Gaussian basis sets are employed to represent the continuum states and an optimization procedure has been developed to obtain the exponents of complex Gaussian basis sets. The application of this method to one- and two-photon ionization yield good agreement with results in literature and the possibility to extend the method to larger molecules has been discussed.

Bibliography

[1] S. V. Popruzhenko. Keldysh theory of strong field ionization: history, applications, difficulties and perspectives. J. Phys. B: At. Mol. Opt. Phys., 47:204001, 2014.

[2] F. H. M. Faisal. Theory of multiphoton processes. Plenum Press, 1987.

[3] C. J. Joachain, N. J. Kylstra, and R. M. Potvliege. Atoms in intense laser fields. Cambridge University Press, 2014.

[4] P. Agostini, F. Fabre, G. Mainfray, G. Petite, and N. K. Rahman. Free-free transitions following six-photon ionization of xenon atoms. Phys. Rev. Lett., 42:1127–1130, 1979.

[5] A. McPherson, G. Gibson, U. Jara, H. Johann, T. S. Luk, I. A. McIntyre, K. Boyer, and C. K. Rhodes. Studies of multiphoton production of vacuum-ultraviolet radiation in rare gase. J. Opt. Soc. Am. B, 4:595, 1987.

[6] X. F. Li, A. L'Huillier, M. Ferray, L. A. Lompré, and G. Mainfray. Multiple-harmonic generation in rare gases at high laser intensity. Phys. Rev. A, 39:5751–5761, 1989.

[7] B. Walker, B. Sheehy, L. F. DiMauro, P. Agostini, K. J. Schafer, and K. C. Kulander. Precision measurement of strong field double ionization of helium. Phys. Rev. Lett., 73:1227–1230, 1994.

[8] A. Talebpour, C.-Y. Chien, Y. Liang, S. Larochelle, and S. L. Chin. Non-sequential ionization of Xe and Kr in an intense femtosecond Ti:sapphire laser pulse. J. Phys. B: At. Mol. Opt. Phys., 30:1721, 1997.

[9] L. Keldysh. Ionization in the field of a strong electromagnetic wave. Sov. Phys. JETP, 20:1307, 1965.

[10] F. H. M. Faisal. Multiple absorption of laser photons by atoms. J. Phys. B, 6:L89, 1973.

[11] H. R. Reiss. Effect of an intense electromagnetic field on weakly bound system. Phys. Rev. A, 22:1786, 1980.

[12] A. M. Perelomov, S. V. Popov, and M. V. Terent'ev. Ionization of atoms in an alternating electric field. Sov. Phys. JETP, 23:924, 1966.

[13] M. V. Ammosov, N. B. Delone, and V. P. Krainov. Tunnel ionization of complex atoms and atomic ions in an alternating electromagnetic field. Sov. Phys. JETP, 64:1191, 1986.

[14] L. D. Landau and E. M. Lifshitz. Quantum Mechanics. Addison Wesley, 1958.

[15] P. A. Franken, A. E. Hill, C. W. Peters, and G. Weinreich. Generation of optical harmonics. Phys. Rev. Lett., 7:118–119, 1961.

[16] T. Popmintchev, M. C. Chen, D. Popmintchev, S. Alisauskas, G. Andriukaitis, T. Balciunas, A. Pugzlys, A. Baltuska, M. Murnane, and H. Kapteyn. Bright coherent attosecond-to-zeptosecond kiloelectronvolt X-ray supercontinua. In Laser Applications to Photonic Applications, page PDPC12, 2011.

[17] T. Popmintchev, M. C. Chen, D. Popmintchev, P. Arpin, S. Brown, S. Alisaukas, G. Andriukaitis, T. Balciunas, O. Mücke, A. Pugzlys, A. Baltuska, B. Shim, S. E. Schrauth, A. Gaeta, C. Hernandez-Garcia, L. Plaja, A. Becker, A. Jaroń-Becker, M. Murnane, and H. Kapteyn. Bright coherent ultrahigh harmonics in the keV X-Ray regime from mid-infrared femtosecond lasers. Science, 336:12878, 2012.

[18] I. P. Christov, M. M. Murnane, and H. C. Kapteyn. High-harmonic generation of attosecond pulses in the "single-cycle" regime. Phys. Rev. Lett., 78:1251, 1997.

[19] M. Hentschel, R. Kienberger, Ch. Spielmann, G. A. Reider, N. Milosevic, T. Brabec, P. Corkum, U. Heinzmann, M. Drescher, and F. Krausz. Attosecond metrology. Nature, 414:509, 2001.

[20] P. M. Paul, E. S. Toma, P. Breger, G. Mullot, F. Augé, Ph. Balcou, H. G. Muller, and P. Agostini. Observation of a train of attosecond pulses from high harmonic generation. Science, 292, 2001.

[21] K. Midorikawa. High-order harmonic generation and attosecond science. Jpn. J. Appl. Phys., 50:090001, 2011.

[22] T. Brabec and F. Krausz. Intense few-cycle laser fields: Frontiers of nonlinear optics. Mod. Phys., 72:545, 2000.

[23] P. Corkum and F. Krausz. Attosecond science. Nat. Phys., 3:381, 2007.

[24] N. B. Delone and V. P. Krainov. Multiphoton processes in atoms. Springer, 2000.

[25] Z. Vager, R. Naaman, and E. P. Kanter. Coulomb explosion imaging of small molecules. Science, 244:426–431, 1989.

[26] P. H. Bucksbaum, A. Zavriyev, H. Muller, and D. W. Schumacher. Softening of the H_2^+ molecular bond in intense laser fields. Phys. Rev. Lett., 64:1883, 1990.

[27] A. Giusti-Suzor, X. He, O. Atabek, and F. H. Frederic. Above-threshold dissociation of H_2^+ in intense laser fields. Phys. Rev. Lett., 64:515, 1990.

[28] A. Etches, M. B. Gaarde, and L. B. Madsen. Two-center minima in harmonic spectra from aligned polar molecules. Phys. Rev. A, 84:023418, 2011.

[29] M. Lein, N. Hay, R. Velotta, J. P. Marangos, and P. L. Knight. Interference effects in high-order harmonic generation with molecules. Phys. Rev. A, 66:023805, 2002.

[30] J. Muth-Böhm, A. Becker, and F. H. M. Faisal. Suppressed molecular ionization for a class of diatomics in intense femtosecond laser fields. Phys. Rev. Lett., 85:2280, 2000.

[31] A. Jaroń-Becker, A. Becker, and F. H. M. Faisal. Saturated ionization of fullerenes in intense laser fields. Phys. Rev. Lett., 96:143006, 2006.

[32] S. Patchkovskii, Z. Zhao, T. Brabec, and D. M. Villeneuve. High harmonic generation and molecular orbital tomography in multielectron systems: Beyond the single active electron approximation. Phys. Rev. Lett., 97:123003, 2006.

[33] B. K. McFarland, J. P. Farrel, P. H. Bucksbaum, and M. Guhr. High harmonic generation from multiple orbitals in N_2. Science, 21:1232, 2008.

[34] O. Smirnova, Y. Mairesse, S. Patchkovskii, N. Dudovich, D. Villeneuve, P. Corkum, and M. Yu. Ivanov. High harmonic interferometry of multi-electron dynamics in molecules. Nature, 460:972, 2009.

[35] B. B. Augstein and C. Figueira DE Morisson Faria. High-order harmonic generation in diatomic molecules: Quantum interference, nodal structures and multiple orbitals. Mod. Phys. Lett. B, 26:1130002, 2012.

[36] D. Dundas. Multielectron effects in high harmonic generation in N_2 and benzene: Simulation using a non-adiabatic quantum molecular dynamics approach for laser-molecule interactions. J. Chem. Phys, 136, 2012.

[37] D. Dundas and J. M. Rost. Molecular effects in the ionization of N_2, O_2, and F_2 by intense laser fields. Phys. Rev. A, 71:013421, 2005.

[38] M. Leibscher, I. Sh. Averbukh, and H. Rabitz. Molecular alignment by train of short laser pulses. Phys. Rev. Lett., 90:213001, 2003.

[39] J. Itatani, J. Levesque, D. Zeidler, H. Niikura, H. Ppin, J. C. Kieffer, P. B. Corkum, and D. M. Villeneuve. Tomographic imaging of molecular orbitals. Nature, 432:867–871, 2004.

[40] M. Lezius, V. Blanchet, D. M. Rayner, D. M. Villeneuve, A. Stolow, and M. Yu. Ivanov. Nonadiabatic multielectron dynamics in strong field molecular ionization. Phys. Rev. Lett., 86:51, 2001.

[41] M. Lezius, V. Blanchet, M. Yu. Ivanov, and A. Stolow. Polyatomic molecules in strong laser field: Nonadiabatic multielectron dynamics. J. Chem. Phys., 117:1575, 2002.

[42] A. Stolow. The three pillars of photo-initiated quantum molecular dynamics. Farad. Discuss., 117:1575, 2013.

[43] J. Parker, K. T. Taylor, C. W. Clark, and S. Blodgett-Fort. Intense-field multiphoton ionization of a two-electron atom. J. Phys. B: At. Mol. Opt. Phys., 29, 1996.

[44] H. G. Muller. Low-frequency above-threshold ionization of a model two-electron atom. Opt. Exp., 8, 2001.

[45] J. S. Parker, B. J. S. Doherty, K J. Meharg, and K. T. Taylor. Time delay between singly and doubly ionization wavepackets in laser-driven helium. J. Phys. B: At. Mol. Opt. Phys., 36, 2003.

[46] A. Jaroń-Becker, A. Becker, and F. H. M. Faisal. Ionization of N_2, O_2, and linear carbon clusters in a strong laser pulse. Phys. Rev. A, 69, 2004.

[47] A. Becker and F. H. M. Faisal. S-matrix theory of two-electron momentum distribution produced by double ionization in intense laser fields. Opt. Exp., 8, 2001.

[48] J. Muth-Böhm, A. Becker, S. L. Chin, and F. H. M. Faisal. S-matrix theory of ionization of polyatomic molecules in an intense laser pulse. Chem. Phys. Lett., 337:313, 2001.

[49] A. Jaroń-Becker, A. Becker, and F. H. M. Faisal. Signature of molecular orientation and orbital symmetry in strong-field photoelectron angular and energy distribution of diatomic molecules and small carbon clusters. Laser Phys., 14:179, 2004.

[50] A. Jaroń-Becker, A. Becker, and F. H. M. Faisal. Dependence of strong-field photoelectron angular distribution on molecular orientation. J. Phys. B: At. Mol. Opt. Phys., 36:L375, 2003.

[51] T. Klamroth. Laser-driven electron transfer through metal-insulator-metal contacts: Time-dependent configuration interaction singles calculations for a jelium model. Phys. Rev. B, 68:245421, 2003.

[52] L. Greenman, P. J. Ho, S. Pabst, E. Kamarchik, D. A. Mazziotti, and R. Santra. Implementation of time-dependent configuration-interaction singles method for atomic strong-field processes. Phys. Rev. A, 74:043420, 2006.

[53] N. Rohringer, A. Gordon, and R. Santra. Configuration-interaction-based time-dependent orbital approach for ab initio treatment of electronic dynamics in a strong optical laser field. Phys. Rev. A, 74:043420, 2006.

[54] S. M. Smith, X. Li, A. N. Markevitch, D. A. Romanov, R. J. Levis, and H. B. Schlegel. A numerical simulation of nonadiabatic electron excitation in the strong field regime: Linear polyenes. J. Phys. Chem. A, 109:5176, 2005.

[55] J. Zanghellini, M. Kitzler, C. Fabian, T. Brabec, and A. Scrinzi. An MCTDHF approach to multilectron dynamics in laser fields. Laser Phys., 13:1064, 2003.

[56] M. Nest, T. Klamroth, and P. Saalfrank. The multiconfiguration time-dependent Hartree-Fock method for quantum chemical calculation. J. Chem. Phys., 122:124102, 2005.

[57] G. Jordan, J. Caillat, C. Ede, and A. Scriniz. Strong field ionization of linear molecules: A correlated three-dimensional calculation. J. Phys. B: At. Mol. Opt. Phys., 39:S341, 2006.

[58] T. Kato and H. Kono. Time-dependent multiconfiguration theory for electronic dynamics of molecules in an intense laser field. Chem. Phys. Lett., 392:533, 2004.

[59] T. Otobe and K. Yabana. Density-functional calculation for the tunnel ionization rate of hydrocarbon molecules. Phys. Rev. A, 75:062507, 2007.

[60] A. Castro, M. A. L. Marques, J. A. Aloso, G. F. Bertsch, and A. Rubio. Excited states dynamics in time-dependent density-functional theory: High-field molecular dissociation and harmonic generation. Eur. Phys. J. D, 28:211, 2004.

[61] E. Runge and E. K. U. Gross. Density-functional theory for time-dependent systems. Phys. Rev. Lett., 52:997, 1984.

[62] D. A. Telnov and Shih-I Chu. Effect of electron structure and multiphoton dynamical response on strong-field multiphoton ionization of diatomic molecules with arbitrary orientation: An all-electron time-dependent density-functional-theory approach. Phys. Rev. A, 79:041401, 2009.

[63] E. P. Fowe and A. D. Bandrauk. Nonlinear time-dependent density-functional-theory study of ionization and harmonic generation in CO_2 by ultrashort intense laser pulses: Orientation effects. Phys. Rev. A, 81:023411, 2010.

[64] J. Liu, Z. Guo, J. Sun, and W. Liang. Theoretical studies on electronic spectroscopy and dynamics with the real-time time-dependent density-functional theory. Front. Chem. China, 5:11, 2010.

[65] M. A. L. Marques, X. López, D. Varsano, A. Castro, and A. Rubio. Time-dependent density-functional approach for biological chromophores: The case of the green fluorescent protein. Phys. Rev. Lett., 90:258101, 2003.

[66] A. Castro, M. Isla, J. Martínez, and J. A. Alonso. Scattering of a proton with the Li_4 cluster: Non-adiabatic molecular dynamics description based on time-dependent density-functional theory. Chem. Phys., 399:130–134, 2012.

[67] M. A. L. Marques, A. Castro, G. F. Bertsch, and A. Rubio. Octopus: a first-principles tool for excited electron–ion dynamics. Comput. Phys. Commun., 151:60–78, 2003.

[68] S. Botti, A. Castro, N. Lathiotakis, X. Andrade, and M. A. L. Marques. Optical and magnetic properties of boron fullerenes. Phys. Chem. Chem. Phys., 11:4523–4527, 2009.

[69] S. I. Chu. Recent development of self-interaction-free time-dependent density functional theory for nonperturbative treatment of atomic and molecular multiphoton processes in intense laser fields. J. Chem. Phys., 123:062207, 2005.

[70] X. Chu and S. I. Chu. Role of the electronic structure and multielectron responses in ionization mechanisms of diatomic molecules in intense short-pulse lasers: An all-electron ab initio study. Phys. Rev. A, 70:061402(R), 2004.

[71] X. Chu and S. I. Chu. Time-dependent density-functional theory for molecular processes in strong fields: Study of multiphoton processes and dynamical response of individual valence electrons of N_2 in intense laser fields. Phys. Rev. A, 64:063404, 2001.

[72] X. Chu and S. I. Chu. Self-interaction-free time-dependent density functional theory for molecular processes in intense laser fields. In 8th International Conference on Multiphoton Processes, volume 525 of AIP Conference Proceedings, pages 415–426, Melville, N.Y., 2000. American Institute of Physics.

[73] M. Oliveira and F. Nogueira. Generating relativistic pseudo-potentials with explicit incorporation of semi-core states using ape, the atomic pseudo-potentials engine. Comput. Phys. Comm., 178, 2008.

[74] G. B. Bachelet, D. R. Hamann, and M. Schluter. Relativistic norm-conserving pseudopotentials. Phys. Rev. B, 25:2103, 1982.

[75] R. M. Dreizler and E. K. Gross. Density Functional Theory. Springer, 1990.

[76] C. Fiolhais, F. Nogueira, and M. Margues. A Primer in Density Functional Theory. Springer, 2003.

[77] W. Koch and M. C. Holthausen. A Chemist's Guide to Density Functional Theory. Wiley-VCH Verlag GmbH, 2001.

[78] R. G. Parr and W. Yang. Density-Functional Theory of Atoms and Molecules. Oxford University Press, 1989.

[79] J.M. Combes, P. Duclos, and R. Seiler. The Born-Oppenheimer approximation. In Rigorous Atomic and Molecular Physics, volume 74 of NATO Advanced Study Institutes Series, pages 185–213. Springer US, 1981.

[80] P. Hohenberg and W. Kohn. Inhomogeneous electron gas. Phys. Rev., 136:B864, 1964.

[81] M. Levy. Electron densities in search of hamiltonians. Phys. Rev. A, 26:1200, 1982.

[82] E. H. Lieb. Density Functional Methods in Physics. Plenum, New York, 1985.

[83] A. K. Theophilou. The energy density functional formalism for excited states. J. Phys. C, 12:5419, 1979.

[84] O. Gritsenko and E. J. Baerends. The spin-unrestricted molecular Kohn-Sham solution and the analogue of Koopmanss theorem for open-shell molecules. J. Chem. Phys., 120:8364, 2004.

[85] P. Strange. Relativistic Quantum Mechanics with Application in Condensed Matter and Atomic Physics. Cambridge University Press, 1998.

[86] K. Capelle. A bird's-eye view of density-functional theory. Braz. J. Phys., 36:1318–1343, 2006.

[87] J. T. Chayes, L. Chayes, and M. B. Ruskai. Density functional approach to quantum lattice systems. J. Stat. Phys., 38:497, 1985.

[88] P. E. Lammert. Coarse-grained v representability. J. Chem. Phys., 125:074114, 2006.

[89] C. A. Ullrich and W. Kohn. Degeneracy in density functional theory: Topology in the ν and n spaces. Phys. Rev. Lett., 89:156401, 2002.

[90] M. A.L. Miguel, O. J.T. Micael, and B. Tobias. Libxc: A library of exchange and correlation functionals for density functional theory. Comput. Phys. Commun., 183:2272 – 2281, 2012.

[91] E. S. Gustavo and N. S. Viktor. Chapter 24 - Progress in the development of exchange-correlation functionals. In Theory and Applications of Computational Chemistry, pages 669 – 724. Elsevier, 2005.

[92] F. Bloch. Bemerkung zur Elektronentheorie des Ferromagnetismus und der elektrischen Leitfähigkeit. Z. Phys., 57:545, 1929.

[93] P. A. M. Dirac. Note on exchange phenomena in the thomas atom. Proc. Camb. Phil. Soc., 26:376, 1930.

[94] P. Gombás. Die Statistische Theorie des Atoms und Ihre Anwendungen. Springer-Verlag Wien, 1949.

[95] J. C. Slater. Quantum Theory of Atomic Structure, volume 2. McGraw-Hill, New York, 1960.

[96] P. R. Antoniewicz and L. Kelinman. Kohn-Sham exchange potential exact to first order in $\rho(K)/\rho_0$. Phys. Rev. B, 31:6779, 1985.

[97] L. Kleinman and S. H. Vosko. Gradient expansion of the exchange-energy density functional: Effect of taking limits in the wrong order. Phys. Rev. B, 37:4634, 1988.

[98] J. A. Chevary and S. H. Vosko. Importance of Pauli-principle restrictions for accurate numerical evaluation of the exchange-only screening function. Phys. Rev. B, 42:5320, 1990.

[99] L. J. Sham. Computational Methods in Band Theory, page 458. Plenum Press, 1971.

[100] D. C. Langreth and J. P. Perdew. Theory of nonuniform electronic systems. I. Analysis of the gradient approximation and a generalization that works. Phys. Rev. B, 21:5469, 1980.

[101] D. C. Langreth and M. J. Mehl. Beyond the local-density approximation in calculations of ground-state electronic properties. Phys. Rev. B, 28:1809, 1983.

[102] J. P. Perdew. Accurate density functional for the energy: Real-space cutoff of the gradient expansion for the exchange hole. Phys. Rev. Lett., 55:1665, 1985.

[103] A. D. Becke. Density functional calculations of molecular bond energies. J. Chem. Phys., 84:4524, 1986.

[104] A. D. Becke. Density-functional exchange-energy approximation with correct asymptotic behavior. Phys. Rev. A, 38:3098, 1988.

[105] A. E. DePristo and J. D. Kress. Rational function representation for accurate exchange energy functionals. J. Chem. Phys., 86:1425, 1987.

[106] J. P. Perdew and Y. Wang. Accurate and simple analytic representation of the electron-gas correlation energy. Phys. Rev. B, 45:13244, 1992.

[107] A. D. Becke and M. R. Roussel. Exchange holes in inhomogeneous systems: A coordinate-space model. Phys. Rev. A, 39:3761, 1989.

[108] A. D. Becke. Density-functional thermochemistry. V. Systematic optimization of exchange-correlation functionals. J. Chem. Phys., 107:8554, 1997.

[109] A. D. Becke. Exploring the limits of gradient corrections in density functional theory. J. Comput. Chem., 20:63, 1999.

[110] A. D. Becke. A new mixing of Hartree-Fock and local density-functional theories. J. Chem. Phys., 98:1372, 1993.

[111] M. Levy, N. H. March, and N. C. Handy. On the adiabatic connection method, and scaling of electronelectron interactions in the Thomas-Fermi limit. J. Chem. Phys., 104:1989, 1996.

[112] R. van Leeuwen and E. J. Baerends. Exchange-correlation potential with correct asymptotic behavior. Phys. Rev. A, 49:2421–2431, 1994.

[113] P. R. T. Schipper, O. V. Gritsenko, S. J. A. van Gisbergen, and E. J. Baerends. Molecular calculations of excitation energies and (hyper)polarizabilities with a statistical average of orbital model exchange-correlation potentials. J. Chem. Phys., 112:1344–1352, 2000.

[114] M. Gell-Mann and K. A. Brueckner. Correlation energy of an electron gas at high density. Phys. Rev., 106:364, 1957.

[115] Jr. W. J. Carr and A. A. Maradudin. Ground-state energy of a high-density electron gas. Phys. Rev., 133:A371, 1964.

[116] P. Nozières and D. Pines. Correlation energy of a free electron gas. Phys. Rev., 111:442, 1958.

[117] Jr. W. J. Carr. Energy, specific heat, and magnetic properties of the low-density electron gas. Phys. Rev., 122:1437, 1961.

[118] D. M. Ceperley and B. J. Alder. Ground state of the electron gas by a stochastic method. Phys. Rev. Lett., 45:566, 1980.

[119] J. P. Perdew and A. Zunger. Self-interaction correction to density-functional approximations for many-electron systems. Phys. Rev. B, 23:5048, 1981.

[120] S. H. Vosko, L. Milk, and M. Nusair. Accurate spin-dependent electron liquid correlation energies for local spin density calculations: a critical analysis. Can. J. Phys., 58:1200, 1980.

[121] N. Troullier and J. L. Martines. Efficient pseudopotentials for plane-wave calculations. Phys. Rev. B, 43, 1991.

[122] L. Kleinman and D. M. Bylander. Efficacious form for model pseudopotentials. Phys. Rev. Lett., 48, 1982.

[123] D. Vanderbilt. Soft self-consistent pseudopotentials in a generalized eigenvalue formalism. Phys. Rev. B, 41:7892, 1990.

[124] G Seifert, D Porezag, and Th Frauenheim. Calculations of molecules, clusters, and solids with a simplified LCAO-DFT-LDA scheme. Int. J. Quant. Chem., 58:185–192, 1996.

[125] L. Pan, K. T. Taylor, and C. W. Clark. Perturbation theory study of high-harmonic generation. J. Opt. Soc. Am. B, 7:509, 1990.

[126] M. C. Kohler, T. Pfeifer, K. Z. Hatsagortsyan, and C. H. Keitel. Frontiers of atomic high-harmonic generation. arXiv, 1201:5094v1, 2012.

[127] R. A. Ganeev. Harmonic generation in laser-produced plasmas containing atoms, ions and clusters: a review. J. Mod. Opt., 59:409, 2012.

[128] M. C. Chen, C. Mancuso, C. Hernandez-Garcia, F. Dollar, B. Galloway, D. Popmintchev, P. C. Huang, B. Walker, L. Plaja, A. A. Jaroń-Becker, A. Becker, M. M. Murnane, H. C. Kapteyn, and T. Popmintchev. Generation of bright isolated attosecond soft X-ray pulses driven by multicycle midinfrared lasers. Proc. Nat. Acad. Sciences, 111:E2361–E2367, 2014.

[129] D.M. Villeneuve, J.B. Bertrand, P.B. Corkum, N. Dudovich, J. Itatani, J.C. Kieffer, F. Lgar, J. Levesque, Y. Mairesse, H. Niikura, B.E. Schmidt, A.D. Shiner, and H.J. Wrner. Studying the electronic structure of molecules with high harmonic spectroscopy. In Attosecond Physics, volume 177 of Springer Series in Optical Sciences, pages 159–190. 2013.

[130] E. Frumker, N. Kajumba, J. B. Bertrand, H. J. Wörner, C. T. Hebeisen, P. Hockett, M. Spanner, S. Patchkovskii, G. G. Paulus, D. M. Villeneuve, A. Naumov, and P. B. Corkum. Probing polar molecules with high harmonic spectroscopy. Phys. Rev. Lett., 109:233904, 2012.

[131] J. B. Bertrand, H. J. Wörner, P. Hockett, D. M. Villeneuve, and P. B. Corkum. Revealing the cooper minimum of $\mathbf{N}_2$ by molecular frame high-harmonic spectroscopy. Phys. Rev. Lett., 109:143001, 2012.

[132] S. Haessler, J. Caillat, W. Boutu, C. Giovanetti-Teixeira, T. Ruchon, T. Auguste, Z. Diveki, P. Breger, A. Maquet, B. Carré, R. Taieb, and P. Salieres. Attosecond imaging of molecular electronic wavepackets. Nat. Phys., 6:200–206, 2010.

[133] W. Boutu, S. Haessler, H. Merdji, P. Breger, G. Waters, M. Stankiewicz, L. J. Frasinski, R. Taieb, J. Caillat, A. Maquet, P. Monchicourt, B. Carre, and P. Salieres. Coherent control of attosecond emission from aligned molecules. Nat. Phys, 4:545, 2008.

[134] W. Li, X. Zhou, R. Lock, S. Patchkovskii, A. Stolow, H. C. Kapteyn, and M. M. Murnane. Time-resolved dynamics in N_2O_4 probed using high harmonic generation. Science, 322:1207–1211, 2008.

[135] O. Smirnova, S. Patchkovskii, Y. Mairesse, N. Dudovich, D. Villeneuve, P. Corkum, and M. Y. Ivanov. Attosecond circular dichroism spectroscopy of polyatomic molecules. Phys. Rev. Lett., 102:063601, 2009.

[136] C. Vozzi, M. Nero, F. Calegari, G. Sansone, M. Nisoli, S. D. Silverstri, and S. Stagira. Generalized molecular orbital tomography. Nat. phys., 7:822–826, 2011.

[137] H. J. Wörner, J. B. Bertrand, D. V. Kartashov, P. B. Corkum, and D. M. Villeneuve. Following a chemical reaction using high-harmonic interferometry. Nature, 466:604, 2010.

[138] C. Altucci, R. Velotta, E. Heesel, E. Springate, J. P. Marangos, C. Vozzi, E. Benedettti, F. Calegari, G. Sansone, S. Stagira, M. Nisoli, and V. Tosa. High-order harmonics generation in alkanes. Phys. Rev. A, 73:043411, 2006.

[139] R. Torres, T. Siegel, L. Brugnera, I. Procino, Jonathan G. Underwood, C. Altucci, R. Velotta, E. Springate, C. Froud, I. C. E. Turcu, S. Patchkovskii, M. Yu. Ivanov, O. Smirnova, and J. P. Marangos. Revealing molecular structure and dynamics through high-order harmonic generation driven by mid-IR fields. Phys. Rev. A, 81:051802, 2010.

[140] P. B. Corkum. Plasma perspective on strong field multiphoton ionization. Phys. Rev. Lett., 71:1994, 1993.

[141] M. Lewenstein, P. Balcou, M. Yu. Ivanov, A. L'Hullier, and P. B. Corkum. Theory of high-harmonic generation by low frequency laser fields. Phys. Rev. A, 49:2117, 1994.

[142] H. Sakai, J. L. Larsen, L. Wendt-Larsen, J. Olesen, P. B. Corkum, and H. Stapelfeldt. Nonsequential double ionization of D_2 molecules with intense 20-fs pulses. Phys. Rev. A, 67:063404, 2003.

[143] M. Lein, J. P. Marangos, and P. L. Knight. Electron diffraction in above-threshold ionization of molecules. Phys. Rev. A, 66:051404, 2002.

[144] T. Popmintchev, M. C. Chen, P. Arpin, M. M. Murnane, and H. C. Kapteyn. The attosecond nonlinear optics of bright coherent X-ray generation. Nat. Photonics, 4:822–832, 2010.

[145] D. M. Volkov. über eine Klasse von Lsungen der Diracschen Gleichung. Z. Physik, 94:250, 1935.

[146] I. V. Litvinyuk, Kevin F. Lee, P. W. Dooley, D. M. Bylander, D. M. Villeneuve, and P. B. Corkum. Alignment-dependent strong field ionization of molecules. Phys. Rev. Lett., 90:233003, 2003.

[147] T. Kanai, S. Minemoto, and H. Sakai. Quantum interference during high-order harmonic generation from aligned molecules. Nature, 435:470–474, 2005.

[148] M. Lein, N. Hay, R. Velotta, J. P. Marangos, and P. L. Knight. Role of the intramolecular phase in high-harmonic generation. Phys. Rev. Lett., 88:183903, 2002.

[149] M. Lein, P. P. Corso, J. P. Marangos, and P. L. Knight. Orientation dependence of high-order harmonic generation in molecules. Phys. Rev. A, 67:023819, 2003.

[150] S. K. Son, D. A. Telnov, and S. I. Chu. Probing the origin of elliptical high-order harmonic generation from aligned molecules in linearly polarized laser fields. Phys. Rev. A, 82:043829, 2010.

[151] H. Sakai and K. Miyazaki. High-order harmonic-generation in nitrogen molecules with subpicosecond visible dye-laser pulse. Appl. Phys. B, 61:493–498, 1995.

[152] Y. Liang, S. Augst, S. L. Chin, Y. Beaudoin, and M. Chaker. High harmonic generation in atomic and diatomic molecular gases using intense picosecond laser pulse-a comparison. J. Phys. B, 27:5119–5130, 1994.

[153] C. Lyngå, A. L'Hullier, and C.-G Wahlström. High-order harmonic genration in molecular gases. J. Phys. B, 29:3293–3302, 1996.

[154] Y. Mairesse, J. Higuet, N. Dudovich, D. Shafir, B. Fabre, E. Mevel, E. Constant, S. Patchkovskii, Z. Walters, M. Y. Ivanov, and O. Smirnova. High harmonic spectroscopy of multichannel dynamics in strong-field ionization. Phys. Rev. Lett., 104:213601, 2010.

[155] Y. Xia and A. Jaroń-Becker. Multielectron contributions in elliptically polarized high-order harmonic emission from nitrogen molecules. Opt. Lett., 39:1461–1464, 2014.

[156] D. M. Gaudiosi, B. Reagan, T. Popmintchev, M. Grisham, M. Berrill, O. Cohen, B. C. Walker, M. M. Murnane, H. C. Kapteyn, and J. J. Rocca. High harmonic generation from ions in a capillary discharge plasma waveguide. Opt. Photonics News, 17:44–44, 2006.

[157] D. Popmintchev, C. Hernández-García, F. Dollar, C. Mancuso, J. Pérez-Hernández, M.C. Chen, A. Hankla, X. Gao, B. Shim, A. Gaeta, M. Tarazkar, D. Romanov, R. Levis, J. Gaffney, M. Foord, S. Libby, A. Jaroń-Becker, A. Becker, L. Plaja, M. Murnane, H. Kapteyn, and T. Popmintchev. Efficient soft X-ray high harmonic generation in multiply-ionized plasmas: the ultraviolet surprise. Science, 350:1225, 2015.

[158] P. Wei, X. Yuan, Z. Zeng, Y. Zheng, J. Jiang, X. Ge, and R. Li. Enhanced high-order harmonic generation from spatially prepared filamentation in argon. Opt. Exp., 29:17229–17236, 2015.

[159] R. A. Ganeev and H. Kuroda. Extremely broadened high-order harmonics generated by the femtosecond pulses propagating through the filaments in air. Appl. Phys. Lett., 95:201117, 2009.

[160] B. R. Mollow. Power spectrum of light scattered by two-level systems. Phys. Rev., 188, 1969.

[161] D. E. Browne and C. H. Keitel. Resonance fluorescence in intense laser fields. J. Mod. Opt., 47:1307, 2000.

[162] T. Zuo, S. Chelkowski, and A. D. Bandrauk. Photon-emission spectra of the H_2^+ molecular ion in an intense laser field. Phys. Rev. A, 49:3943, 1994.

[163] C. R. Jacob and M. Reiher. Spin in density-functional theory. Int. J. Quant. Chem., 112:3661, 2012.

[164] X. Zhou, R. Lock, N. Wagner, W. Li, H. C. Kapteyn, and M. M. Murnane. Elliptically polarized high-order harmonic emission from molecules in linearly polarized laser fields. Phys. Rev. Lett., 102:073902, 2009.

[165] X. B. Zhou, R. Lock, W. Li, N. Wagner, M. M. Murnane, and H. C. Kapteyn. Molecular recollision interferometry in high harmonic generation. Phys. Rev. Lett., 100:073902, 2008.

[166] A. T. Le, R. R. Lucchese, and C. D. Lin. Polarization and ellipticity of high-order harmonics from aligned molecules generated by linearly polarized intense laser pulses. Phys. Rev. A, 82, 2010.

[167] J. Levesque, Y. Mairesse, N. Dudovich, H. Pépin, J. C. Kieffer, P. B. Corkum, and D. M. Villeneuve. Polarization state of high-order harmonic emission from aligned molecules. Phys. Rev. Lett., 99:243001, 2007.

[168] L. Holmegaard, J. L. Hansen, L. Kalhøj, S. L. Kargh, H. Stapelfeldt, F. Filsinger, J. Küpper, G. Meijer, D. Dimitrovski, M. Abu-samba, C. P. J. Martiny, and L. B. Madsen. Photoelectron angular distributions from strong-field ionization of oriented molecules. Nat. Phys., 6:428, 2010.

[169] C. Z. Bisgaard, O. J. Clarkin, G. Wu, A. M. D. Lee, O. Gebner, C. C. Hayden, and A. Stolow. Time-resolved molecular frame dynamics of fixed-in-space CS_2 molecules. Science, 323:1464–1468, 2009.

[170] G. N. Gibson, R. R. Freeman, and T. J. Mcllrath. Dynamics of the high-intensity multiphoton ionization of N_2. Phys. Rev. Lett., 67:1230, 1991.

[171] S. L. Chin, Y. Liang, J. E. Decker, F. A. Ilkov, and M. V. Ammosov. Tunnel ionization of diatomic molecules by an intense CO_2 laser. J. Phys. B, 25:L249, 1992.

[172] T. D. G. Walsh, J. E. Decker, and S. L. Chin. Tunnel ionization of simple molecules by an intense CO_2 laser. J. Phys. B, 26:L85, 1993.

[173] T. Zuo and A. D. Bandrauk. Charge-resonance-enhanced ionization of diatomic molecular ions by intense lasers. Phys. Rev. A, 52:R2511, 1995.

[174] T. Seideman, M. Y. Ivanov, and P. B. Corkum. Role of electron localization in intense-field molecular ionization. Phys. Rev. Lett., 75:2819, 1995.

[175] W. Li, A. Jaroń-Becker, C. W. Hogle, V. Sharma, X. Zhou, A. Becker, H. C. Kapteyn, and M. M. Murnane. Visualizing electron rearrangement in shape and time during the transition from a molecule to atoms. Proc. Natl. Acad. Sci., 107:20219, 2010.

[176] E. Lötstedt, T. Kato, and K. Yamanouchi. Intramolecular electron dynamics in the ionization of acetylene by an intense laser pulse. J. Chem. Phys., 138:104304, 2013.

[177] E. P. Fowe and A. D. Bandrauk. Nonperturbative time-dependent density-functional theory of ionization and harmonic generation in OCS and CS_2 molecules with ultrashort intense laser pulses: Intensity and orientational effects. Phys. Rev. A, 84:035402, 2011.

[178] W. Chu, H. Li, J. Ni, B. Zeng, J. Yao, H. Zhang, G. Li, C. Jing, H. Xie, H. Xu, K. Yamanouchi, and Y. Cheng. Lasing action induced by femtosecond laser filamentation in ethanol flame for combustion diagnosis. App. Phys. Lett., 104(9), 2014.

[179] W. Chu, B. Zeng, J. Yao, H. Xu, J. Ni, G. Li, H. Zhang, F. He, C. Jing, Y. Cheng, and Z. Xu. Multiwavelength amplified harmonic emissions from carbon dioxide pumped by mid-infrared femtosecond laser pulses. Europhys. Lett, 97(6):64004, 2012.

[180] T. Streibel and R. Zimmermann. Resonance-enhanced ionization mass spectrometry (REMPI-MS): Application for process analysis. Annu. Rev. Anal. Chem., 7:361, 2014.

[181] X. Li, J. C. Tully, H. B. Schlegel, and M. J. Frisch. Ab initio Ehrenfest dynamics. J. Chem. Phys., 123:084106, 2005.

[182] S. I. Chu and D. A. Telnov. Beyond the Floquet theorem: Generalized Floquet formalisms and quasienergy methods for atomic and molecular multiphoton processes in intense laser fields. Phys. Rep., 390:1, 2004.

[183] J.-F. Daigle, A. Jaroń-Becker, S. Hosseini, T.-J. Wang, Y.. Kamali, G. Roy, A. Becker, and S. L. Chin. Intensity clamping measurement of laser filamentation in air at 400 and 800 nm. Phys. Rev. A, 82:023405, 2010.

[184] J. Yao, B. Zeng, H. Xu., G. Li, W. Chu, J. Ni, H. Zhang, S. L. Chin, Y. Cheng, and Z. Xu. High-brightness switchable multiwavelength remote laser in air. Phys. Rev. A, 84:051802, 2011.

[185] H. Zhang, C. Jing, G. Liand H. Xie, J. Yao, B. Zeng, W. Chu, J. Ni, H. Xu, and Y. Cheng. Abnormal dependence of strong-field-ionization-induced nitrogen lasing on polarization ellipticity of the driving field. Phys. Rev. A, 88:063417, 2013.

[186] J. Ni, W. Chu, C. Jing, H. Zhang, B. Zhang, J. Yao, G. Li, H. Xie, C. Zhang, H. Xu, S. L. Chin, Y. Cheng, and Z. Xu. Identification of the physical mechanism of generation of coherent N_2^+ emissions in air by femtosecond laser excitation. Opt. Exp., 21:8746, 2013.

[187] H. Y. Tan, Y. Sun, W. Lo, S. J. Lin, C. H. Hsiao, Y. F. Chen, C.-M. Huang, W. C. Lin, S. H. Jee, H. S. Yu, and C. Y. Dong. Multiphoton fluorescence and second harmonic generation imaging of the structural alterations in keratoconus ex vivo. Invest. Ophthalmol. Vis. Sci., 47:5251, 2006.

[188] D. Ding, J. Huang, R. N. Compton, C. E. Klots, and R. E. Haufler. CW laser ionization of C_{60} and C_{70}. Phys. Rev. Lett., 73:1084, 1994.

[189] A. Baev, O. Rubio-Pons, F. Gel'mukhanov, and H. Agren. Optical limiting properties of zinc- and platinum-based organometallic compounds. J. Phys. Chem. A, 108:7406–7416, 2004.

[190] M. Tsubouchi, B. J. Whitaker, and T. Suzuki. Femtosecond photoelectron imaging on pyrazine: S1 $\rightarrow$ T1 intersystem crossing and rotational coherence transfer. J. Phys. Chem. A, 108:6823–6835, 2004.

[191] H. S. Yoo, M. J. DeWitt, and B. H. Pate. Vibrational dynamics of terminal Acetylenes: II. Pathway for vibrational relaxation in gas and solution. J. Phys. Chem. A, 108:1365–1379, 2004.

[192] J. R. Barker, L. M. Yoder, and K. D. King. Vibrational energy transfer modeling of nonequilibrium polyatomic reaction systems. J. Phys. Chem. A, 105(5):796–809, 2001.

[193] J. Che, J. L. Krause, M. Messina, K. R. Wilson, and Y. Yan. Detection and control of molecular quantum dynamics. J. Phys. Chem., 99:14949–14958, 1995.

[194] A. N. Markevitch, S. M. Smith, D. A. Romanov, H. B. Schlegel, M. Yu. Ivanov, and R. J. Levis. Nonadiabatic dynamics of polyatomic molecules and ions in strong laser fields. Phys. Rev. A, 63:011402(R), 2003.

[195] A. N. Markevitch, D. A. Romanov, S. M. Smith, H. B. Schlegel, M. Yu. Ivanov, and R. J. Levis. Sequential nonadiabatic excitation of large molecules and ions driven by strong laser field. Phys. Rev. A, 69:013401, 2004.

[196] X. Li, S. M. Smith, A. N. Markevitch, D. A. Romanov, R. J. Levis, and H. B. Schlegel. A time-dependent Hartree-Fock approach for studying the electronic optical response of molecules in intense fields. Phys. Chem. Chem. Phys., 7:233, 2005.

[197] S. M. Smith, X. Li, A. N. Markevitch, D. A. Romanov, R. J. Levis, and H. B. Schlegel. Numerical simulation of nonadiabatic electron excitation in the strong field regime. 2. linear polyene cations. J. Phys. Chem. A, 109:10527, 2005.

[198] S. M. Smith, X. Li, A. N. Markevitch, D. Romanov, R. J. Levis, and H. B. Schlegel. Numerical simulation of nonadiabatic electron excitation in the strong field regime. 3. polyacene neutrals and cations. J. Phys. Chem. A, 111:6920, 2007.

[199] H. B. Smith, D. A. Romanov, X. Li, J. A. Sonk, H. B. Schlegel, and R. J. Levis. Numerical bound state electron dynamics of carbon dioxide in the strong-field regime. J. Phys. Chem. A, 114:2576, 2010.

[200] S. Chelkowski, A. Conjusteau, T. Zuo, and A. Bandrauk. Dissociative ionization of H_2^+ in an intense laser field: Charge-resonance-enhanced ionization, Coulomb explosion, and harmonic generation at 600 nm. Phys. Rev. A, 54:3235, 1996.

[201] N. Takemoto and A. Becker. Time-resolved view on charge-resonance-enhanced ionization. Phys. Rev. A, 84:023401, 2011.

[202] R. Bavli and H. Metiu. Laser-induced localization of an electron in double-well quantum structure. Phys. Rev. Lett., 69:1986, 1992.

[203] G. L. Kamta and A. D. Bandrauk. Effects of molecular symmetry on enhanced ionization by intense laser pulses. Phys. Rev. A, 75:041401, 2007.

[204] S. I. Chu. Generalized Floquet theoretical apapproach to intense field multiphoton and nonlinear optical processes. Adv. Chem. Phys., 73:739, 1989.

[205] A. Jaroń-Becker. Multiphoton processes in intense laser fields. PhD thesis, Warsaw University, 2001.

[206] L. W. Garland, A. Jaroń, J. Z. Kamiński, and R. M. Potvliege. Off-shell effects in laser-assisted electron scattering at low frequency. J. Phys. B: At. Mol. Opt. Phys., 35:2861, 2002.

[207] R. M. Potvliege and R. Shakeshaft. In Atoms in intense laser fields, page 373. Academic Press, New York, 1992.

[208] A. Jaroń, R. M. Potvliege, and E. Mese. Floquet analysis of laser-induced continuum structures. J. Phys. B: At. Mol. Opt. Phys., 33:1487, 2000.

[209] L. B. Madsen, M. Plummer, and J. F. McCann. Multiphoton ionization of H_2^+ by intense light: A comparison of Floquet and wave-packet results. Phys. Rev. A, 58:456, 1998.

[210] P. V. Likhatov and D. A. Telnov. Multiphoton ionization of H_2^+ at critical internuclear separation: Non-Hermitian Floquet analysis. J. Phys. B: At. Mol. Opt. Phys., 42:105603, 2009.

[211] T. T. Nguyen-Dang, F. Chateauneuf, O. Atabek, and X. He. Time-resolved dynamics of two-channel molecular systems in CW laser fields: Wave-packet construction in the Floquet formalism. Phys. Rev. A, 51:1387, 1995.

[212] T. T. Nguyen-Dang, C. Lefebvre, H. Abou-Rachid, and O. Atabek. Floquet representation of absolute phase and pulse-shape effects on laser-driven molecular photon dissociation. Phys. Rev. A, 71:023403, 2005.

[213] R. M. Potvliege and R. Shakeshaft. Multiphoton processes in an intense laser field: Harmonic generation and total ionization rates for atomic hydrogen. Phys. Rev. A, 40:3061, 1989.

[214] D. A. Telnov, J. Wang, and S. I. Chu. Two-color phase control of high-order harmonic generation in intense laser fields. Phys. Rev. A, 52:3988, 1995.

[215] K. Drese and M. Hlthaus. Floquet theory for short laser pulses. Eur. Phys. J. D, 5:119, 1999.

[216] D. Telnov and S. I. Chu. Floquet formalism of time-dependent density functional theory. Chem. Phys. Lett., 264:466, 1997.

[217] P. Salek, T. Helgaker, and T. Saue. Linear response at the 4-component relativistic density functional level: application to the frequency-dependent dipole polarizability of H_g, AuH and PtH_2. Chem. Phys., 311:187, 2005.

[218] G. Floquet. Sur les équations différentielles linéaires à coefficients périodiques. Ann. I'Ecol. Norm. Sup., 12:47, 1883.

[219] R. M. Potvliege. STRFLO: a program for time-independent calculation of multiphoton processes in one-electron atomic systems I. Quasienergy spectra and angular distributions. Comput. Phys. Commun., 114:42–93, 1998.

[220] C. C. Yu, R. M. Pitzer, and C. W. McCurdy. Molecular photoionization cross sections by the complex-basis-function method. Phys. Rev. A, 32:2134, 1985.

[221] S. Balay, S. Abhyankar, M. F. Adams, J. Brown, P. Brune, K. Buschelman, L. Dalcin, V. Eijkhout, W. D. Gropp, D. Kaushik, M. G. Knepley, L. C. McInnes, K. Rupp, B. F. Smith, S. Zampini, and H. Zhang. PETSc Web page, 2015.

[222] V. Hernandez, J. E. Roman, and V. Vidal. SLEPc: A scalable and flexible toolkit for the solution of eigenvalue problems. ACM Trans. Math. Software, 31:351–362, 2005.

[223] J. Aguilar and J. M. Combes. A class of analytic perturbations for one-body Schrödinger Hamiltonians. Commun. Math. Phys., 22:269–279, 1971.

[224] E. Balslev and J. M. Combes. Spectral properties of many-body Schrödinger operators with dilatation-analytic interactions. Commun. Math. Phys., 22:280–294, 1971.

[225] W. P. Reinhart. Complex coordinates in the theory of atomic and molecular structure and dynamics. Ann. Rev. Phys. Chem., 33:223–255, 1982.

[226] T. N. Rescigno, C. W. McCurdy, and A. E. Orel. Extensions of the complex-coordinate method to the study of resonances in many-electron systems. Phys. Rev. A, 17:1931–1938, 1978.

[227] N. Moiseyev. Non-Hermitian quantum mechanics. Cambridge University Press, 2011.

[228] A. Szaba and N. S. Ostlund. Modern Quantum Chemistry: Introduction to advanced Quantum Chemistry. Dover Publications, 1989.

[229] Peter M.W. Gill. Molecular Integrals over Gaussian basis functions. Adv. Quantum Chem., 25:141 – 205, 1994.

[230] M. Galassi, J. Davies, J. Theiler, G. Gough, G. Jungman, P. Alken, M. Booth, and F. Rossi. GNU Scientific Library Reference Manual, volume 83. 2009.

[231] M. Plummer and J. F. McCann. Complex-basis-function Floquet calculation of multiphoton ionization rates in hydrogen systems. J. Phys. B, 28:4073–4089, 1995.

[232] M. Morita and S. Yabushita. Photoionization cross sections of H_2^+ and H_2 with complex Gaussian-type basis functions optimized for the frequency-dependent polarizabilities. J. Comput. Chem., 29:2471, 2008.

[233] G. D. Doolen. A procedure for calculating resonance eigenvalue. J. Phys. B: At.. Mol. Phys., 8:525, 1975.

[234] Y. K. Ho. A resonant state and the ground state of positronium hydride. Phys. Rev. A, 17:1675, 1978.

[235] C. W. McCurdy and F. Martín. Implementation of exterior complex scaling in B-splines to solve atomic and molecular collision problems. J. Phys. B: At. Mol. Opt. Phys., 37:917, 2004.

[236] M. Honigmann, H.-P. Liebermann, and R. J. Buenker. Use of complex configuration interaction calculations and the stationary principle for the description of metastable electronic states of HCl^{-}. J. Chem. Phys., 133:044305, 2010.

[237] T. N. Rescigno. Atomic photoionization by the complex-basis-function expansion method: Application to ground-state and metastable M_g. Phys. Rev. A, 31:607, 1985.

[238] R. Matsuzaki, S. Asai, C. W. McCurdy, and S. Yabushita. Construction of complex STO-NG basis sets by the method of least squares and their applications. Theor. Chem. Acc., 133:1521, 2014.

[239] G. Liuzzi, S. Lucidi, and M. Sciandrone. Sequential penalty derivative-free methods for nonlinear constrained optimization. Siam. J. Optimiz., 20(5):2614–2635, 2010.

[240] R. E. Perez, P. W. Jansen, and J. R. R. A. Martins. PyOpt: A Python-based object-oriented framework for nonlinear constrained optimization. Struct. Multidiscip. O., 45:101–118, 2012.

[241] S. I. Chu. Intense field multiphoton ionization via complex dressed states: application to the H atom. Phys. Rev. Lett., 39:1195–1198, 1977.

[242] L. Tao, C. W. McCurdy, and T. N. Rescigno. Grid-based methods for diatomic quantum scattering problems. III. Double photoionization of molecular hydrogen in prolate spheroidal coordinates. Phys. Rev. A, 82:023423, 2010.

[243] N. Moiseyev, M Chrysos, and R Lefebvre. The solution of the time-dependent Schrödinger equation by the (t,t') method: application to intense field molecular photodissociation. J. Phys. B: At. Mol. Opt. Phys., 28:2599, 1995.

[244] E. J. Baerends, O. V. Gritsenko, and R. Van Meer. The KohnSham gap, the fundamental gap and the optical gap: the physical meaning of occupied and virtual KohnSham orbital energies. Phys. CHem. Chem. Phys., 15:16408–16425, 2013.

[245] S. Baker, J. S. Robinson, C. A. Haworth, H. Teng, R. A. Smith, C. C. Chirilă, M. Lein, J. W. G. Tisch, and J. P. Marangos. Probing proton dynamics in molecules on an attosecond time scale. Science, 312:424–427, 2006.

[246] P. Balanarayan and N. Moiseyev. Linear Stark effect for sulfur atom in strong high-frequency laser fields. Phys. Rev. Lettt., 110:253001, 2013.

[247] A. Baltuška, Th. Udem, M. Uiberacker, M. Hentschel, E. Goulielmakis, Ch. Gohle, R. Holzwarth, V. S. Yakovlev, A. Scrinzi, T. W. Hänsch, and F. Krausz. Attosecond control of electronic processes by intense light fields. Nature, 421:611–615, 2003.

[248] A. D. Bandrauk and F. Légaré. Progress in Ultrafast Intense Laser Science VIII, chapter Chap. 2. Springer, NY, 2012.

[249] A. D. Bandrauk. Molecules in Laser Fields, chapter Chap. 4. Marcel Dekker Inc., NY, 1994.

[250] D. Bauer, D. B. Milosevic, and W. Becker. Strong-field approximation for intense-laseratom processes: The choice of gauge. Phys. Rev. A, 72:023415, 2005.

[251] A. D. Becke. On the large-gradient behavior of the density functional exchange energy. J. Chem. Phys., 85:7184, 1986.

[252] R. V. Leeuwen and E. J. Baerends. Exchange-correlation potential with correct asymptotic behavior. Phys. Rev. A, 49:2421, 1994.

[253] N. H. Burnett, H. A. Baldis, M. C. Richardson, and G. D. Enright. Harmonic generation in CO_2 laser target interaction. Appl. Phys. Lett., 31:172, 1977.

[254] R. L. Carman, D. W. Forlund, and J. M. Kindel. Visible harmonic emission as a way of measuring profile steepening. Phys. Rev. Lett., 46:29, 1981.

[255] R. L. Carman, C. K. Rhodes, and R. F. Benjamin. Observation of harmonics in the visible and ultraviolet created in CO_2-laser-produced plasmas. Phys. Rev. A, 24:2649, 1981.

[256] Chan L., M. Siemens, M. M. Murnane, H. C. Kapteyn, S. Mathias, M. Aeschlimann, P. Grychtol, R. Adam, C. M. Schneider, J. M. Shaw, H. Nembach, and T. J. Silva. Ultrafast demagnetization dynamics at the M edges of magnetic elements observed using a tabletop high-harmonic soft X-ray source. Phys. Rev. Lett., 103:257402, 2009.

[257] P. B. Corkum, N. H. Burnett, and F. Brunel. Above-threshold ionization in the long-wavelength limit. Phys. Rev. Lett., 62:1259, 1989.

[258] M. Drescher, M. Hentschel, R. Kienberger, M. Uiberacker, V. Yakovlev, A. Scrini, Th. Westerwalbeslon, U. Kleineberg, U. Heinzmann, and F. Krausz. Time-resolved atomic inner-shell spectroscopy. Nature, 419:803–807, 2002.

[259] D. J. Fraser, MHR Hutchinson, JP Marangos, YL Shao, JWG Tisch, and M. Castillejo. High harmonic generation in butane and butadiene. J. Phys. B: At. Mol. Opt. Phys., 28:L739–L745, 1995.

[260] E. Gagnon, P. Ranitovic, X. M. Tong, C. L. Cocke, M. M. Murnane, H. C. Kapteyn, and A. S. Sandhu. Soft X-ray-driven femtosecond molecular dynamics. Science, 317:1374–1378, 2007.

[261] P. Jemmer and P. J. Knowles. Exchange energy in Kohn-Sham density-functional theory. Phys. Rev. A, 51:3571, 1995.

[262] F. Krausz and M. Ivanov. Attosecond physics. Rev. Mod. Phys., 81:163, 2009.

[263] W. Li, V. Sharma, C. Hogle, A. Jaroń-Becker, A. Becker, H. Kapteyn, and M. Murnane. Ultrafast molecular dynamics probed using strong field ionization. In Second International Conference on Attosecond Physics, 2009.

[264] Z. H. Loh, M. Khalil, R. E. Correa, R. Santra, C. Buth, and S. R. Leone. Quantum state-resolved probing of strong-field-ionized xenon atoms using femtosecond high-order harmonic transient absorption spectroscopy. Phys. Rev. Lett., 98:143601, 2007.

[265] E. A. McLean, J. A. Stamper, B. H. Ripin, H. R. Griem, J. M. McMahon, and S. E. Bodner. Harmonic generation in Nd:laser-produced plasmas. Appl. Phys. Lett., 31:825, 1977.

[266] L. Miaja-Avila, C. Lei, M. Aeschlimann, J. L. Gland, M. M. Murnane, H. C. Kapteyn., and G. Saathoff. Laser-assisted photoelectric effect from surfaces. Phys. Rev. Lett., 97:113604, 2006.

[267] R. S. Mulliken. Intensities of electronic transitions in molecular spectra II. Charge-transfer spectra. J. Chem. Phys., 7:20, 1939.

[268] G. Saathoff, L. Miaja-Avila, M. Aeschlimann, M. M. Murnane, and H. C. Kapteyn. Laser-assisted photoemission from surfaces. Phys. Rev. A, 77:022903, 2008.

[269] A. Savin, C. J. Umrigar, and X. Gonze. Relationship of Kohn-Sham eigenvalues to excitation energies. Chem. Phys. Lett., 288:391, 1998.

[270] J. M. Schins, P. Breger, P. Agostini, R. C. Constantinescu, H. G. Muller, G. Grillon, A. Antonetti, and A. Mysyrowicz. Observation of laser-assisted auger decay in Argon. Phys. Rev. Lett., 73:2180–2183, 1994.

[271] A. Srinzi, M. Y. Ivanov, R. Kienberger, and D. M. Villeneuve. Attosecond physics. J. Phys. B, 39:R1, 2006.

[272] M. E. Siemens, Q. Li, R. Yang, K. A. Nelson, E. H. Anderson, M. M. Murnane, and H. C. Kapteyn. Quasi-ballistic thermal transport from nanoscale interfaces observed using ultrafast coherent soft X-ray beams. Nature, 9:26–30, 2010.

[273] R. Stowasser and R. Hoffmann. What do the Kohn-Sham orbitals and eigenvalues mean? J. Am. Chem. Soc., 121:3414, 1999.

[274] A. V. Titov, A. O. Mitrushenkov, and I. I. Tupitsyn. Effective core potential for pseudo-orbitals with nodes. Chem. Phys. Lett., 185:330, 1991.

[275] X. M. Tong, Z. X. Zhao, and C. D. Lin. Theory of molecular tunnel ionization. Phys. Rev. A, 66:033402, 2002.

[276] R. Torres, N. Kajumba, J. G. Underwood, J. S. Robinson, S. Baker, J. W. Gtisch, R. de Nalda, W. A. Bryan, R. Velotta, C. Altucci, I. C. E. Turcu, and J. P. Marangos. Probing orbital structure of polyatomic molecules by high-order harmonic generation. Phys. Rev. Lett., 98:203007, 2007.

[277] D. J. Tozer and N. C. Handy. Improving virtual Kohn-Sham orbitals and eigenvalues: Application to excitation energies and static polarizabilities. J. Chem. Phys., 109:10180, 1998.

[278] A. J. Verhaef. Optical detection of tunneling ionization. Phys. Rev. Lett., 104:163904, 2010.

[279] J. Yao, G. Li, C. Jing, B. Zeng, W. Chu, J. Ni, H. Zhang, H. Xie, C. Zhang, H. Li, H. Xu, S. L. Chin, Y. Cheng, and Z. Xu. Remote creation of coherent emissions in air with two-color ultrafast laser pulses. New J. Phys., 15(2):023046, 2013.

[280] B. Zhang, W. Chu, G. Liand J. Yao, H. Zhang, J. Ni, C. Jing, H. Xie, and Y. Cheng. Real-time observation of dynamics in rotational molecular wave packets by use of air-laser spectroscopy. Phys. Rev. A, 89:042508, 2014.

[281] T. Zuo, S. Chelkowski, and A. D. Bandrauk. Harmonic generation by the H_2^+ molecular ion in intense laser fields. Phys. Rev., 48:3837, 1993.